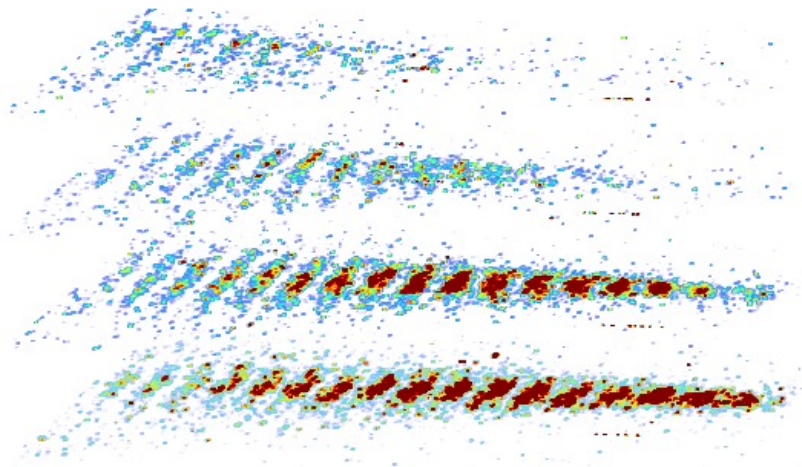**Doctoral Thesis**

Electron Bunch Seeding of the Self-Modulation Instability in Plasma
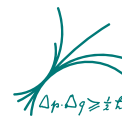

Livio Verra

March 2022

Department of Physics

Technical University of Munich

Max-Planck Institute for Physics
(Werner-Heisenberg Institute)

CERN

TECHNISCHE UNIVERSITÄT MÜNCHEN
Fakultät für Physik

Electron bunch seeding of the self-modulation instability in plasma

Livio Verra

Vollständiger Abdruck der von der Fakultät für Physik der Technischen Universität München zur Erlangung des akademischen Grades eines

Doktors der Naturwissenschaften (Dr. rer. nat.)

genehmigten Dissertation.

Vorsitzende:

    Prof. Dr. Laura Fabbietti

Prüfer der Dissertation:

1. Hon.-Prof. Dr. Allen C. Caldwell

2. Prof. Dr. Peter Fierlinger

Die Dissertation wurde am 04.04.2022 bei der Technischen Universität München eingereicht und durch die Fakultät für Physik am 20.05.2022 angenommen.

A Sofia,
che ha riportato la gioia
nella nostra famiglia

"Baby, you ain't seen nothing yet"

Abstract

Plasma wakefield acceleration uses relativistic charged particle bunches to accelerate electron bunches to high energies. For the last three decades, this method has been considered a solution for high-gradient acceleration and a valuable scheme for future accelerators.

The Advanced WAKefield Experiment (AWAKE) makes use of the large amount of energy stored in relativistic proton bunches to accelerate electron bunches to high energy in a single stage. The length of the available proton bunches is $\sim 7\,\mathrm{cm}$, that is too long to effectively drive wakefields with GV/m amplitude in plasmas with density $> 10^{14}\,\mathrm{cm}^{-3}$. Thus, the AWAKE scheme relies on the self-modulation instability of the proton bunch to drive wakefields with large amplitude.

In this work, I demonstrate experimentally that the wakefields driven by a short electron bunch can seed the self-modulation instability of a long proton bunch in plasma. I show that the timing of the self-modulation is reproducible from event to event and that it is controlled by the timing of the seed bunch at the picosecond time scale.

When seeding with the electron bunch, the growth of the self-modulation can be independently controlled by the amplitude of the seed wakefields and by the growth rate of the instability. I show that increasing the charge of the seed electron bunch increases the amplitude of the seed wakefields, leading to a larger growth of the self-modulation, while the growth rate remains constant. Analogously, when increasing the proton bunch charge, the growth rate of the self-modulation increases.

Moreover, I show that the hosing instability of the proton bunch is seeded by purposely misaligning the trajectory of the seed electron bunch with respect to that of the proton bunch. I also discuss a method to obtain three-dimensional images of the self-modulated p^+ bunch.

These results are important milestones on the path towards high-energy physics applications of proton driven plasma wakefield acceleration.

Contents

Chapter 1

Introduction

1.1 Particle accelerators

Particle accelerators are machines that use electromagnetic fields to increase the energy of charged particles, containing them in well-defined beams, and they are the tools used to study high-energy particle physics. To investigate the interaction between elementary particles, charged beams are accelerated and sent to collide against fixed solid targets or against each other, and the results of the collisions are measured using particle detectors.

The energy of the beams at the interaction point of a collider defines the energy of the center-of-mass of the collisions. Higher center-of-mass energy allows to create particles with larger mass and to resolve smaller structures of matter. Therefore, accelerator physicist has always been seeking ways to achieve higher beam energies.

Conventional accelerators increase the energy of the particles using longitudinal electric fields produced in radio-frequency (RF) cavities. High-gradient accelerators use the electrostatic fields that can be sustained in media such as plasmas.

1.2   State of the art of particle accelerators

The most powerful collider currently operating is the Large Hadron Collider (LHC) at CERN. The LHC is a storage ring with circumference of 26.7 km, in which two identical, counter-rotating, bunched proton (p^+) beams are accelerated to 6.5 TeV. The beams collide at four interaction points with center-of-mass energy of 13 TeV.

The quality of a collider is quantified with a parameter called luminosity, that is defined, for identical beams colliding head-on, as:

$$L = \frac{N^2 f}{4\pi \sigma_x \sigma_y},$$ (1.1)

where N is the number of particles per bunch, f the collision repetition rate, σ_x and σ_y the transverse size of the bunches at the interaction point. The value of L therefore indicates the number of interactions per units of time and area. In 2018, LHC reached instantaneous luminosity $L = 1.9 \cdot 10^{34}\,\mathrm{cm^{-2}s^{-1}}$ [1]. The high energy and quality of the collisions at LHC allowed for the detection of extremely rare events and for the discovery of the Higgs boson in 2012 [2], for which the Nobel Prize was awarded in 2013.

Protons are composite particles consisting of quarks and gluons with mass $m_p = 1.6 \cdot 10^{-27}\,\mathrm{kg} = 936\,\mathrm{MeV/c^2}$. Therefore, in $p^+ p^+$ collisions, quarks and gluons collide with high energies, although individually undefined, providing a noisy collision environment. In lepton colliders, point-like particles collide with well-defined energies. As a consequence, lepton colliders are better suited for precision measurements at the center-of-mass energy.

The most powerful lepton collider was the Large Electron-Positron (LEP) collider at CERN. In the same tunnel where LHC is located nowadays, LEP reached a maximum center-of-mass energy of 209 GeV in 2000. LEP's experiments provided detailed studies of the electroweak interaction.

Circular particle accelerators, such as LEP and LHC, bend charged particle beams on circular trajectories using the magnetic field of electromagnetic dipoles. Particles gain energy every turn as they pass through an accelerating section, but they loose energy due to synchrotron radiation. The amount of energy U_0 that a

relativistic particle loses as synchrotron radiation over one turn is [3]:

$$U_0 = \frac{4\pi r_e}{3(m_0 c^2)^3} \frac{E^4}{\rho} = \frac{e^2 \gamma^4}{3\varepsilon_0 \rho}, \tag{1.2}$$

where r_e is the classical electron radius, m_0 the particle mass at rest, e the elementary charge, c the speed of light, E the particle energy, γ the Lorentz factor, $\rho = \gamma m_0 c / qB$ the bending radius of the particle in the magnetic field B, ε_0 the vacuum permittivity. Equation 1.2 shows that the energy loss per turn depends on the particle energy and on the mass at rest to the power four. This makes circular accelerators unfavourable for the acceleration of light particles such as electrons (e^-) and positrons (e^+), but favorable for heavier particles like protons, ions and muons. Due to the limited energy gain per turn and the synchrotron radiation loss, the maximum energy that e^+ and e^- can reach in circular colliders is significantly lower than the energy that p^+ can reach. This is why p^+ are currently accelerated in LHC up to 6.5 TeV, while e^+ and e^- in LEP were accelerated up to 104.5 GeV, because of the limitations due to the synchrotron radiation loss (at this maximum energy, $U_0 \sim 2.8$ GeV). The energy of the p^+ beam is limited by the strength of the magnetic field that keeps the particles on the circular trajectory. The ratio between the magnetic field B_0 and the bending radius ρ_b is equal to the beam rigidity $\gamma m_0 c / e$.

Linear particle accelerators consist of many accelerating sections, where the energy loss due the synchrotron radiation is negligible. The most powerful linear collider was the 3.2-km-long Stanford Linear Collider (SLC) at SLAC National Accelerator Laboratory, in which e^+ and e^- were colliding with center-of-mass energy up to 91 GeV and $L = 6 \cdot 10^{30}$ cm^{-2}s^{-1} [4]. SLC operated between 1987 and 1998 to study in detail the properties of the Z boson.

A fraction of SLC was then converted into a free electron laser (FEL): the Linac Coherent Light Source (LCLS). In an FEL, the e^- beam is made to oscillate transversely, after acceleration, using magnetic wigglers and undulators [5]. The e^- beam emits synchrotron radiation with high temporal coherence and characteristics similar to a laser pulse. The most powerful FEL in operation is the 3.4-km-long European XFEL at the Deutsches Elektronen-Synchrotron (DESY) [6]. In this machine, e^- bunches are accelerated to 17.5 GeV with a root

mean square (rms) energy spread of $2\,\mathrm{MeV}$ and normalized transverse emittance $\epsilon_N = 0.97\,\mathrm{mm}$ mrad.

1.3 Proposals for future colliders based on RF technology

The design of an accelerator is strongly influenced by the application for which it is conceived. The high-energy particle physics community defined the main goal of the next machine, after the completion of the LHC program, that is to reach the energy frontier well beyond the production energy of the Higgs boson, to study physics beyond the Standard Model.

The most recent proposal of a hadron collider is the Future Circular Collider (FCC) at CERN [7]. This would be a p^+p^+ collider with circumference of $91\,\mathrm{km}$, reaching center-of-mass energy $> 100\,\mathrm{TeV}$. Over an envisioned 25 years of operation, FCC would provide an integrated luminosity ten times larger than LHC and allow for the direct discovery of high-mass particles.

As an intermediate step towards the future hadron collider, the same tunnel would first host an e^+e^- collider (FCC-ee) [8]. This machine would provide center-of-mass energy increasing over the 15 years of operation from the Z boson production ($91\,\mathrm{GeV}$) to the $t\bar{t}$ production ($365\,\mathrm{GeV}$). With an extremely high precision on the collision energy ($\sim 100\,\mathrm{keV}$) and high luminosity (e.g., $L \sim 10^{36}\,\mathrm{cm}^{-2}\mathrm{s}^{-1}$ for Z production), FCC-ee would be an electroweak and Higgs factory, allowing for the detection of rare decays that are postulated in theory. In this machine, synchrotron radiation would cause a power loss of $50\,\mathrm{MW}$/beam at all energies and require top-up injection [9]. Thus, a booster synchrotron would be installed in the same tunnel to continuously feed the collider.

The main linear e^+e^- collider projects under investigation are the Compact Linear Collider (CLIC) at CERN [10] and the International Linear Collider (ILC) in Japan [11]. CLIC would provide center-of-mass energy from $380\,\mathrm{GeV}$ to $3\,\mathrm{TeV}$, for an increasing length of the machine from 11 to $50\,\mathrm{km}$ over 30 years of operation. In its current design, CLIC would exploit normal-conducting RF cavities with ac-

celerating field $\sim 70\,\mathrm{MV/m}$, powered by $2\,\mathrm{GeV}$ drive e^- beams. ILC would exploit superconducting RF cavities to achieve a first center-of-mass energy of $250\,\mathrm{GeV}$, extendable up to $1\,\mathrm{TeV}$ (the length of the machine would be 20.5-40 km). These machines would provide $L \sim 10^{34}\,\mathrm{cm^{-2}s^{-1}}$ and serve as electroweak factories and as colliders working at the high-energy frontier.

1.4   Limitation of conventional accelerators

The center-of-mass energy of hadron and e^+e^- colliders has increased over the years with exponential rate until the 1990s, as shown in Figure 1.1. Since then, the rate of increase has slowed down due to the limitations of the RF and magnet technologies. Increasing further the energy of the beams has become extremely expensive and requires building remarkably long machines.
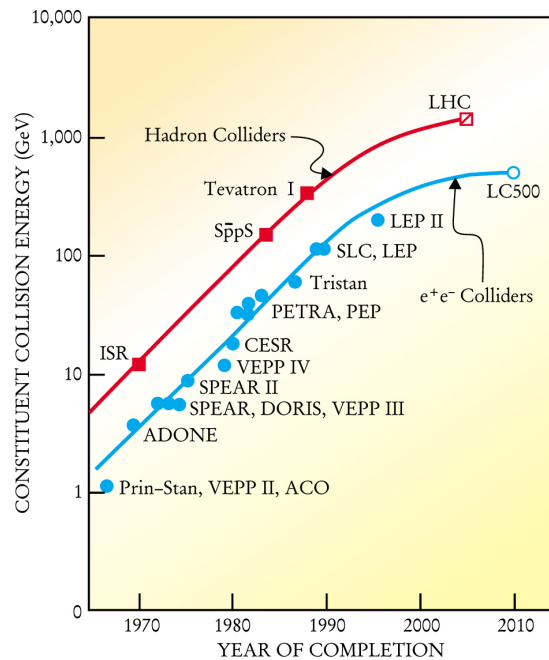

Figure 1.1: Effective constituent collision energy (i.e., center-of-mass energy) of hadron colliders (red curve) and e^+e^- colliders (blue curve), plotted in semi-logaritmic scale against completion date. Figure from [12]

RF technology is very advanced and can be reliably employed in accelerators and colliders. The main limitation is the accelerating gradient. In fact, state of the art RF cavities can produce accelerating electric fields up to $\sim 100\,\mathrm{MV/m}$. This limit is due to the electric breakdown of the structure of the cavity [13], that can be caused by fatigue and pulsed heating. Further factors limit the performance of superconductive RF cavities, such as quench magnetic field, field emission and thermal breakdown.

In a linear machine, the energy gained by a particle is the product between the accelerating gradient and the length of the accelerator. Thus, to reduce the foot-print and cost of a linear lepton accelerator, it is necessary to obtain larger accelerating gradients. The best candidate for high-gradient acceleration is the plasma wakefield technology.

1.5   Plasma wakefield acceleration

Plasmas can sustain electric fields with amplitude larger than in RF cavities, as they consist of free electrons and ions [14] (i.e., they are already "broken down"). When an intense laser pulse or a relativistic charged particle bunch (the *driver*) travels in plasma, its transverse electric field displaces the plasma electrons [15, 16]. The plasma ions, that are much more massive than the electrons, remain immobile (at the timescale of this process) and provide a charge-neutrality restoring force that induces an oscillation of the plasma electrons, after the driver has passed. The drive bunch therefore transfers energy to the plasma generating an inhomogeneity in the plasma electron distribution. The local charge non-neutrality sustains electrostatic waves: the wakefields [15, 16]. The wakefields experienced by a following particle or bunch (the *witness*) have longitudinal (E_z) and transverse ($W_\perp = E_r + v_w \times B_\theta$) components ($E_r$ is the radial electric field, B_θ the azimuthal magnetic field and v_w the velocity of the witness). In linear theory [17], E_z and $W_\perp$ are sinusoidal and $\pi/2$ out of phase with respect to each other. Thus, a witness particle or bunch can be accelerated to high energies, if it travels in the focusing and accelerating phase of the wakefields. Figure 1.2 shows schematically the plasma wakefields driving process, with a short e^- drive bunch.
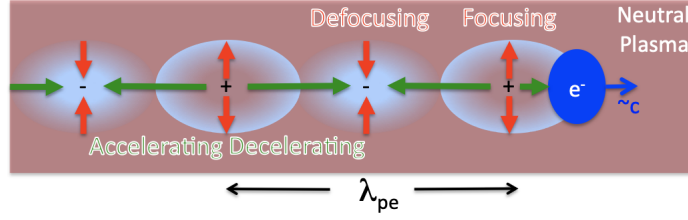
Figure 1.2: Schematic of a short e^- drive bunch (blue in the Figure), going from left to right in neutral plasma (brown background) with speed c, driving wakefields. The residual charge inhomogeneity (white faint ellipses) sustains the longitudinal and transverse wakefields (green and red arrows). Figure from [18].

The maximum electric field that can be generated at a given plasma electron density n_{pe} is estimated by the linear, cold, wave-breaking field E_{WB} as [14]:

$$E_{WB} = \frac{m_e c \omega_{pe}}{e} \sim 100\,\text{V/m} \sqrt{n_{pe}\,[\text{cm}^{-3}]}, \tag{1.3}$$

where m_e is the mass of the electron and ω_{pe} is the plasma electron angular frequency, defined as:

$$\omega_{pe} = \sqrt{\frac{n_{pe} e^2}{m_e \varepsilon_0}}. \tag{1.4}$$

Plasma wakefield experiments use plasma electron densities in the $(10^{14} - 10^{18})\,\text{cm}^{-3}$ range, allowing for maximum accelerating fields on the order of $(1 - 100)\,\text{GV/m}$. Plasma wakefield acceleration is therefore appealing to reduce the length, the cost and the foot-print of future accelerators.

The distance over which the plasma wakefields are driven depends on the energy content of the driver. The drive bunch (or pulse) excites the wakefields by depositing energy into the plasma and a fraction of this energy may be recaptured by the witness bunch. The distance L over which a charged drive bunch with energy E_b can sustain wakefields with amplitude E_z (without considering other diminishing effects such as dephasing and diffraction) can be roughly estimated as:

$$L = e \frac{E_b[J]}{E_z[V/m]}. \tag{1.5}$$

The energy in single laser pulses and electron bunches is typically on the order of ~ 10 and $100\,\mathrm{J}$, respectively. This limits the length of the plasma wakefield accelerator and requires a staging system to reach high energies. This means that, before the driver is totally depleted of its energy, the witness bunch is extracted from the plasma and injected into a new section, where a new driver creates the wakefields. The process of catching and injecting the witness bunch at each stage makes staging a complex process that may jeopardize the quality of the witness bunch. Acceleration in a single, long stage is therefore desirable.

1.5.1 Laser driven plasma wakefield acceleration

In 1979, T. Tajima and J.M. Dawson proposed that laser driven plasma wakefields could trap and accelerate electrons [15]. The experimental realization followed in 1992 by a group at the University of California, Los Angeles, using a laser plasma beatwave accelerator [19]. Laser plasma wakefield acceleration (LWFA) experiments using a single laser pulse became possible with the invention of chirped pulse amplification (CPA) [20]. In 2006, three groups have been able to produce electron beams with a finite energy spread (few %), using short, intense laser pulses [21, 22, 23]. In 2014 a research group at the Lawrence Berkeley National Laboratoy (LBNL) used a $300\,\mathrm{TW}$ laser system to accelerate $6\,\mathrm{pC}$ of electrons to $4.2\,\mathrm{GeV}$ in $9\,\mathrm{cm}$ of plasma (average accelerating gradient $\sim 47\,\mathrm{GeV/m}$) with a rms energy spread of 6% [24]. Even higher energies ($\sim 8\,\mathrm{GeV}$) were reached guiding the drive laser pulse through a 20-cm-long laser-heated capillary discharge waveguide [25].

After the high accelerating gradient has been demonstrated, the research shifted on staging, that is necessary to reach higher energies. Further experiments at LBNL have demonstrated acceleration in two independent laser-driven stages [26], using active plasma lenses [27] to catch the witness e^- bunch from the first stage and inject it into the second one.

The e^- bunches produced in LWFA can also be used to drive light sources, if the quality and stability of the acceleration process is high enough. Major progress on energy spread minimization and stability has been made at DESY [28, 29] and the first lasing of an e^- bunch obtained from a LWFA has been proven at the

Shanghai Institute of Optics and Fine Mechanics [30].

1.5.2   Beam driven plasma wakefields acceleration

In 1985, P. Chen, J. M. Dawson, W. Huff, and T. Katsouleas suggested that the plasma wakefields could also be driven by a relativistic electron bunch [16]. The demonstration of beam driven plasma wakefield acceleration (PWFA) followed in an experiment at the Argonne National Laboratory in 1988 [31]. Experiments at SLAC demonstrated in 2007 that some electrons were accelerated from 42 to 84 GeV in 85 cm of plasma (average accelerating gradient ~ 49 GeV/m) [32]. High gradient, two-bunch acceleration was demonstrated in 2008 [33].

After the demonstration of the principle, the research focused on the efficiency of the acceleration process [34], on the energy spread minimization [35, 36, 37, 38] and on the emittance preservation [39]. The first demonstration of lasing of an e^- bunch accelerated in a PWFA was performed at INFN-Laboratori Nazionali di Frascati [40]. This is a fundamental step towards PWFA facility for user-oriented applications. One of the current proposals is EuPRAXIA@SPARC_LAB [41], aiming to operate a short wavelength FEL by the end of 2029.

The possibility of accelerating electrons up to 600 GeV in 600 m of plasma with wakefields driven by a relativistic p^+ bunch was suggested in 2009 [42]. For charged particles, the energy E_b stored in a single particle with rest mass m_0 is:

$$E_b = \gamma m_0 c^2. \tag{1.6}$$

The energy stored in available, single, relativistic p^+ bunches can be extremely high. For example, the 400 GeV/c p^+ bunch with bunch charge $Q_p = 48$ nC from the CERN Super Proton Synchrotron (SPS) carries ~ 20 kJ. Relativistic p^+ bunches can therefore drive plasma wakefields without energy depletion nor dephasing over very long distances ($\mathcal{O}(100\,\text{m})$) [43]. The acceleration of electrons in p^+ driven plasma wakefields up to 2 GeV was demonstrated in 2018 at AWAKE at CERN [44]. In the following Section, I will discuss the AWAKE experiment and the potential applications of this scheme.

1.6   The AWAKE experiment at CERN

AWAKE [45], the Advanced WAKefield Experiment is a proof-of-principle R&D project at CERN to study p^+ driven plasma wakefield acceleration. In AWAKE, a $400\,\text{GeV/c}$ p^+ bunch is delivered by CERN SPS and injected in plasma. Since the length of the p^+ bunch is much longer than the plasma electron wavelength, it is subject to the transverse occurrence of the two-stream instability [46, 47], the self-modulation instability (SMI) [48]. During the self-modulation (SM), the long bunch is converted into a train of microbunches that resonantly drive large amplitude wakefields. Seeding the instability makes this process reproducible from event to event and allows for the controlled injection and acceleration of e^- bunches.

The first goal of AWAKE Run 1 (2016-2018)[49] was to demonstrate that the long p^+ bunch self-modulates in plasma [50, 51] and that SM can be seeded using a relativistic ionization front [52]. The second goal was to use the wakefields driven by the self-modulated p^+ bunch to accelerate externally injected electrons [44].

AWAKE Run 2 (started in 2021) aims to accelerate e^- witness bunches to GeV energies while preserving the initial quality. The roadmap of the experiment over the decade has been organized in phases, towards the first high-energy physics applications.

In this thesis I show experimentally for the first time that the self-modulation in plasma can also be seeded using the wakefields driven by a short, preceding e^- bunch.

1.6.1   AWAKE Run 1

Figure 1.3 shows the experimental setup. The core of the experiment is a 10-m-long rubidium (Rb) vapor source. A $\sim 120\,\text{fs}$, $\sim 100\,\text{mJ}$ laser pulse ($\lambda = 780\,\text{nm}$) produces a relativistic ionization front (RIF) that creates the plasma by ionizing the Rb atoms. (RbI→RbII) [53].

Upstream of the vapor source three beamlines merge, bringing together:

- the proton bunch from SPS (red in Figure 1.3)

- the ionizing laser pulse (green)
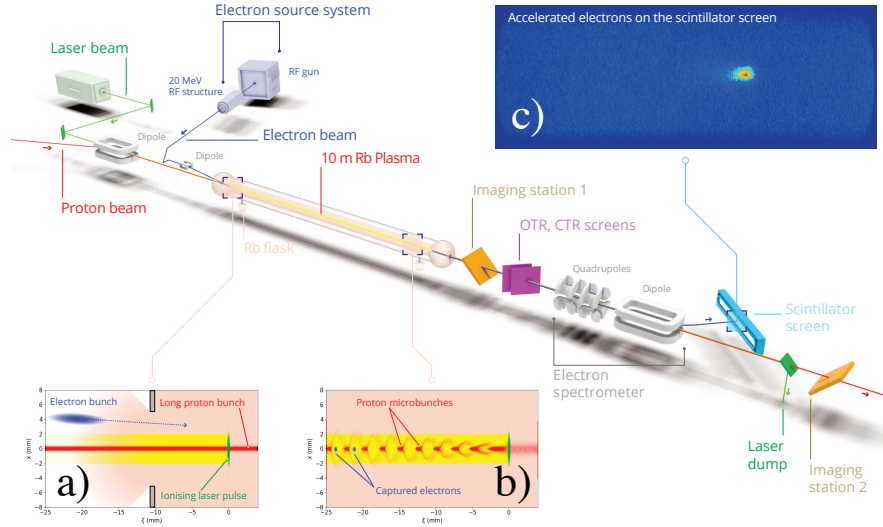
- the witness electron bunch (blue).

Figure 1.3: Schematic layout of the AWAKE experiment. Proton (red), laser (green) and electron (blue) beams are merged upstream of the Rb vapor source (yellow cylinder). The proton beam diagnostics and the electron spectrometer are positioned downstream of the vapor source. Inset (a) is a schematic of the beam injection geometry at the entrance of the vapor source for the acceleration experiment. Inset (b) shows the modulated proton bunch and captured electrons at the exit of the plasma. Inset (c) is an image of the accelerated e^- beam at the spectrometer screen. Figure from [44].

The RIF propagates within the p^+ bunch. It ionizes the Rb vapor and seeds SM (so-called ionization-front seeding): the fast onset of the beam-plasma inter-action at the RIF location provides the seed wakefields from which SM grows. The temporal overlap of the three bunches is shown in Figure 1.4: the laser pulse (green) travels within the p^+ bunch (red) at the peak of the bunch charge density to seed SM. Ahead of the laser pulse, the p^+ bunch travels in Rb vapor and there-fore remains un-modulated. Behind the laser pulse, the plasma sustains the seed wakefields (green line). The witness e^- bunch (blue) is located at $\sim 1\,\sigma_t$ behind the laser pulse (σ_t is the rms duration of the p^+ bunch).
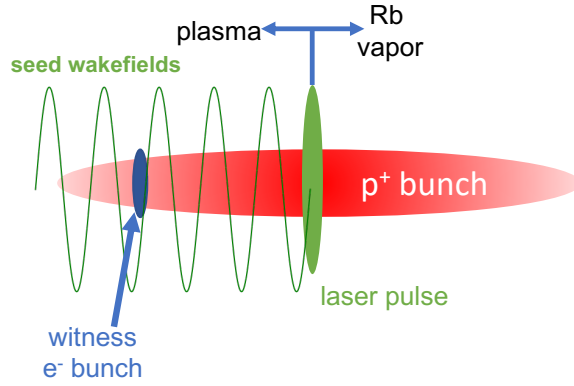
Figure 1.4: Schematic drawing of the temporal overlap of the p^+ (red), e^- (blue) and laser (green) beams in Run 1 (ionization-front seeding). The beams travel from left to right.

The experimental setup is presented in detail in Section 3.1 and the main results of AWAKE Run 1 are summarized in Chapter 4.

1.6.2   AWAKE Run 2

The goal of Run 2 is to accelerate witness e^- bunches to high energies while preserving the initial bunch quality. A first plasma section will be dedicated to SM of the p^+ bunch (modulator) and a second section to the electron acceleration (accelerator). The injection of the witness e^- bunch will take place in a gap region between the two sections [54]. With this scheme, the e^- bunch is injected on-axis, in vacuum, after SM saturation, avoiding the disruptive effect of the growth of the wakefields on the injection process. To reach witness bunch energies $> 10\,\mathrm{GeV}$, the length of the accelerator will be $> 10\,\mathrm{m}$, and therefore the plasma will be pre-ionized.

As mentioned before, when the un-modulated p^+ bunch enters a pre-ionized plasma, it undergoes the self-modulation instability, unless seeding occurs. If SM was seeded with a relativistic ionization front, the front of the bunch would undergo SMI in the second plasma section. The wakefields driven by the front of the bunch might then interfere with, and disrupt, the structure of the wakefields

driven by the seeded SM in the back of the bunch. Therefore, the entire p^+ bunch must be self-modulated with reproducible timing and amplitude, when entering the accelerator section. This can be obtained only if the seed wakefields act on the entire p^+ bunch.
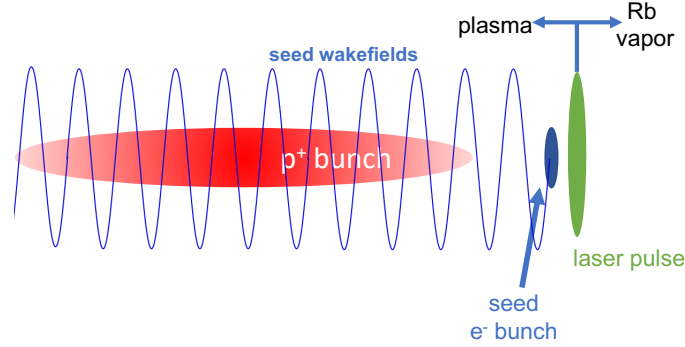

Figure 1.5: Schematic drawing of the temporal overlap of the p^+ (red) and seed e^- (blue) bunches and laser pulse (green) at the entrance of the modulator for Run 2. The seed wakefields (blue line) are driven by the e^- bunch.

Seeding using the wakefields driven by a preceding e^- bunch is the goal of AWAKE Run 2a (2021-2022, making use of the existing facility and setup) and the topic of this thesis. Figure 1.5 shows the timing setup for Run 2 at the entrance of the modulator. The ionizing laser pulse travels far ahead of the p^+ bunch, so that the RIF does not seed SM [52]. The e^- bunch travels close behind the RIF, driving the seed wakefields. Therefore, the entire p^+ bunch self-modulates.

Theoretical studies and simulations [48, 55, 56] have shown that the maximum accelerating field driven by the self-modulated bunch decreases along the plasma, after saturation, due to dephasing between the wakefields and the microbunches. Figure 1.6 shows that the maximum amplitude of the wakefields driven by a self-modulated LHC bunch decreases after saturation, in case of constant plasma density (thin red line). It was demonstrated in previous experiments (see Section 4.4) that a gradient in the plasma electron density can mitigate this effect [57]. To maximize the amplitude of the wakefields driven by the self-modulated bunch, a plasma density step will be applied in the modulator [58]. Numerical simulations showed that, when a density step is introduced, the amplitude of the wakefields

remains at the saturation level for long distance along the plasma (see the thick red line in Figure 1.6) [59]. The effect of the density step will be studied experimentally during Run 2b (2023-2024).
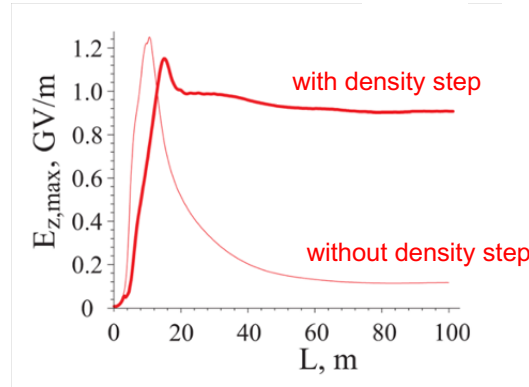

Figure 1.6: Maximum amplitude of the longitudinal wakefields driven by a self-modulated LHC p^+ bunch along the plasma in case of uniform plasma electron density (thin red line) and in case of a density step (thick red line). Figure from [59].

Run 2c (starting in 2028) will implement the previous results. In the first plasma section, with plasma density step, the p^+ bunch will undergo SM, seeded by the e^- bunch. A witness $150\,\text{MeV}$ e^- bunch will be injected on-axis in the gap region and it will enter the wakefields in the second plasma section. Blowout [60], matching and beam loading [61] will be exploited to preserve the quality of the witness bunch during the acceleration process [54, 62]. The final setup of AWAKE Run 2c is shown in Figure 1.7. In this scheme, the Rb vapor in the accelerator will be ionized by a counter-propagating laser pulse. Thus, the p^+ bunch will effectively enter a pre-ionized plasma, in the accelerator. This makes the e^- bunch seeding extremely important, because the entire p^+ bunch must self-modulate with reproducible timing before entering the accelerator section.

After the completion of Run 2c, the use of novel scalable plasma sources will be studied, in the context of Run 2d. The goal is to extend the length the accelerator over tens of meter, so as to prove the scaling of the e^- bunch energy gain. The plasma technologies currently under study are helicon and discharge plasma sources. Afterwards, AWAKE will be ready to provide e^- bunches for the

first high-energy physics applications.
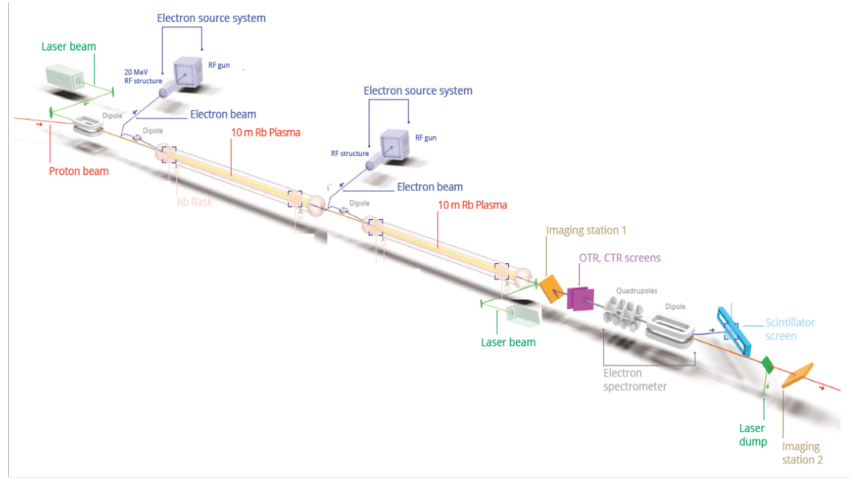
Figure 1.7: Schematics of AWAKE Run 2c.

1.6.3   Particle physics applications of AWAKE

By the conclusion of Run 2, AWAKE should have demonstrated the acceleration of e^- bunches with stable GeV/m accelerating gradient and preservation of the bunch quality to the 10 mm mrad level.

The first application of the AWAKE scheme would be to use the high-energy e^- bunch colliding on a fixed solid target. For this application, there are no strong requirements on the emittance and on the transverse size of the accelerated bunch. The interaction of electrons with the target may produce dark photons, that would then decay into e^+e^- pairs [63]. Assuming a 50 GeV bunch containing $5 \cdot 10^9$ electrons [64], the AWAKE scheme could enable a fixed target experiment with number of electrons on target per year several orders of magnitude higher than in current experiments, such as NA64 at CERN [65].

Another potential application is using the e^- bunches accelerated with the AWAKE scheme in collisions with high-power laser pulses to investigate strong-fields quantum electrodynamics [64].

The most ambitious application of the AWAKE scheme is an electron-proton

collider. In this case, $\mathcal{O}(50\,\text{GeV})$ e^- bunches would collide with p^+ bunches produced by LHC. Even though limited in luminosity ($L \sim 10^{27}\,\text{cm}^{-2}\text{s}^{-1}$), this would be the first compact collider based on PWFA. The focus of the physics program would be on quantum chromodynamics and on the study of the inner structure of the proton. The natural upgrade of this scheme would be to drive the plasma wakefields using p^+ bunches from LHC. In this case, the accelerator could be scaled to km-length, and could lead to the production of e^- bunches at the TeV level, allowing for center-of-mass energies $\mathcal{O}(10\,\text{TeV})$ [66].

1.7 Topic of this thesis

In this thesis I discuss the seeding of the self-modulation instability in plasma using a preceding e^- bunch, that is the main goal of AWAKE Run 2a. I show with experimental results that the e^- bunch seeds effectively the self-modulation by proving that the p^+ bunch self-modulates with reproducible timing from event to event (Section 6.3). Moreover, I demonstrate that the growth of the SM can be controlled by varying independently the seed wakefields amplitude (Section 6.4) and the growth rate of the SM (Section 6.5).

Chapter 2

Theoretical background

2.1 Definition of plasma

Plasma is a state of matter with peculiar properties, defined in [67] as:

"A quasineutral gas of charged and neutral particles which exhibits collective behaviour".

As it is normally generated by ionizing a gas, the number of ions and electrons are equal, and so are the densities. The densities are high enough that plasma ions and plasma electrons can be treated collectively as fluids. The opposite charged fluids are coupled to each other and tend to electrically neutralize one another. In fact, the motion of ions and electrons is dominated by the electromagnetic fields generated by the local charge inhomogeneity and particle motion, rather than by collisions.

As the plasma particles are relatively free to move, they shield out the potentials that are applied to the plasma. When a local positive or negative non-neutrality is present, a sheath of plasma electrons develops around it so that the electric field is non-negligible only within a shielding distance, called the Debye-length, that is defined as:

$$\lambda_D = \sqrt{\frac{\varepsilon_0 k_B T_e}{n_{pe} e^2}}, \tag{2.1}$$

where k_B is the Boltzmann's constant and T_e is the plasma electron temperature, that is related to the particles velocity. It is the electrons temperature T_e and density n_{pe} which is used for the definition of λ_D because the electrons are much more mobile than the ions due to their smaller mass. In fact they generally move, in case of a local non-neutrality, so as to create a surplus or deficit of negative charge. When n_{pe} increases, λ_D decreases because each layer of plasma contains more electrons. Moreover, λ_D increases when increasing T_e: without thermal agitation the charge cloud would collapse to an infinitely thin layer.

When the dimensions L of the system are much larger than λ_D, the local or externally applied potentials are shielded within a distance short compared with L. This is why plasma is defined as *quasineutral*. Therefore, one criterion for an ionized gas to be a plasma is to be dense enough so that λ_D is much shorter than L. Also, the number of particles N_D in a sphere with radius equal to λ_D (a Debye sphere) must be high enough to make the Debye shielding a statistically valid concept. In addition to $\lambda_D << L$, collective behaviour requires $N_D >> 1$.

The ion or electron plasma frequency

$$\omega_{pi,e} = \sqrt{\frac{n(i,e)^2}{\varepsilon_0 m_{i,e}}}, \tag{2.2}$$

where (i,e) and $m_{i,e}$ are the charge and mass of the ions or of the electrons, respectively. Since $m_e << m_i$, $\omega_{pe} >> \omega_{pi}$. Thus, the *electron* frequency ω_{pe} is the most important for the processes discussed here, because they happen at the time scale relevant for the oscillations of the plasma electrons. In fact, ω_{pe} corresponds to the typical electrostatic oscillation frequency of an electron in response to a small charge separation.

Plasma oscillations are observed only if the plasma system is studied over time periods longer than the plasma period $T_{pe} = 2\pi/\omega_{pe}$ and if external actions change the system at a rate slower than ω_{pe}. To study the system as a plasma, the electrostatic interactions must dominate over collisions between particles. Therefore, the mean time between collisions T_c must be longer than the plasma period.

In conclusion, the conditions a plasma must satisfy are:

1. $\lambda_D >> L$

2. $N_D >> 1$

3. $T_c > T_{pe}$

2.1.1   The AWAKE plasma

The plasma in AWAKE is created by ionizing Rb vapor [68] with an $\sim 120\,\mathrm{fs}$ and $< 450\,\mathrm{mJ}$ laser pulse focused with transverse size at the entrance of the vapor source $\sigma_r \sim 1\,\mathrm{mm}$. With these parameters, the intensity and energy of the laser pulse are high enough to ionize the outermost electron of each rubidium atom (the first ionization potential is $4.12\,\mathrm{eV}$) on its path [69]. The vapor density is adjustable in the range $n_{vap} = (0.5 - 10) \cdot 10^{14}\,\mathrm{cm}^{-3}$. Since the laser pulse ionizes $\sim 100\%$ of the atoms on its path [50], in the following $n_{vap} = n_{pe}$. The electron temperature is a few eV. For a temperature of $4\,\mathrm{eV}$ and $n_{pe} = 7 \cdot 10^{14}\,\mathrm{cm}^{-3}$, $\lambda_D \sim 0.6\,\mathrm{\mu m}$ and $N_D \sim 500$.

2.2   Plasma wakefields

As discussed in Section 1.5, when a charged particle bunch travels in plasma, it drives longitudinal and transverse wakefields. The longitudinal component of the wakefields E_z (in the direction of the wave-vector) can be used to accelerate charged particles.

AWAKE uses the space-charge fields of a relativistic ($\gamma{=}427$) p^+ bunch to drive plasma wakefields. Since a relativistic, charged bunch carries almost purely transverse electric field, it radially displaces the plasma electrons, inducing their oscillation. Part of the energy stored in the bunch is converted into a longitudinal electric field that can be used for charged particle acceleration.

2.2.1   Linear plasma wakefield theory

Linear theory allows to calculate the wakefields driven by a charge distribution, as long as the density perturbation δn is small compared to n_{pe}. In the 2D cylindrical case (z, r), one can define the longitudinal and radial density profiles

as n_b:

$$n_b(\xi = ct - z, r) = n_{b0} \cdot n_{b||}(\xi) \cdot n_{b\perp}(r), \tag{2.3}$$

where ξ is the position along the relativistic p^+ bunch moving at $v_b \sim c$, n_{b0} is the peak charge density, $n_{b||}$ is the longitudinal distribution and $n_{b\perp}$ is the radial distribution, both normalized to one. The longitudinal plasma wakefields E_z driven by a bunch distribution defined as in Equation 2.3 can be calculated with [17]:

$$E_z(\xi, r) = \frac{n_{b0}q}{\varepsilon_0} \int_{-\infty}^{\xi} n_{b||}(\xi')cos(k_{pe}(\xi - \xi'))d\xi' \cdot R(r) \tag{2.4}$$

and the transverse wakefields $W_\perp = E_r - cB_\theta$

$$W_\perp(\xi, r) = \frac{-n_{b0}q}{\varepsilon_0 k_{pe}} \int_{-\infty}^{\xi} n_{b||}(\xi')sin(k_{pe}(\xi - \xi'))d\xi' \cdot \frac{dR(r)}{dr}, \tag{2.5}$$

where $R(r)$ is defined by:

$$
\begin{aligned}
R(r) = k_{pe}^2 K_0(k_{pe}r) \int_0^r r' n_{b\perp}(r') I_0(k_{pe}r') dr' \\
+ k_{pe}^2 I_0(k_{pe}r) \int_r^\infty r' n_{b\perp}(r') K_0(k_{pe}r') dr'
\end{aligned}
\tag{2.6}
$$

The term $R(r)$ defines the radial dependency of the longitudinal wakefields. Its value is maximum on axis ($r = 0$), and so is the amplitude of the longitudinal wakefield. The derivative of $R(r)$ describes the radial dependency of the transverse wakefields as a function of r. The transverse wakefields amplitude is zero on axis and maximum at $r \sim \sigma_r$, that is the transverse size of the drive bunch. The maximum amplitude of E_z and of $W_\perp$ at a given ξ are related according to:

$$|W_\perp|_{max} = |E_z|_{max} \frac{|dR/dr|_{max}}{k_{pe}|R|_{max}} \tag{2.7}$$

For the experiment described in this thesis, the p^+ bunch to plasma density ratio n_p/n_{pe} is small, as $n_{pe} \sim 1 \cdot 10^{14}\,\text{cm}^{-3}$ and $n_p \leq 8.8 \cdot 10^{12}\,\text{cm}^{-3}$ (peak density of the p^+ bunch with charge $Q_p = 46.9\,\text{nC}$ and 2D-Gaussian (r, t) density distribution with rms transverse size at the plasma entrance $\sigma_{(x,y)} = (0.175, 0.167)\,\text{mm}$ and rms duration $\sigma_t = 239\,\text{ps}$). Thus, linear theory applies before SM occurs.

Linear plasma wakefields theory shows that to effectively drive large amplitude wakefields, the rms bunch duration σ_t must satisfy:

$$\omega_{pe}\sigma_t = \sqrt{2}. \tag{2.8}$$

Moreover, to avoid transverse current filamentation instability [70], the rms transverse size σ_r must satisfy

$$k_{pe}\sigma_r \leq 1, \tag{2.9}$$

where $k_{pe} = \omega_{pe}/c$ (k_{pe}^{-1} is the plasma skin depth). As experiments normally use high plasma electron densities ($n_{pe} > 10^{14}\,\mathrm{cm}^{-3}$), the drive bunches must be short and focused tightly to drive wakefields effectively.

The SPS p^+ bunch can be focused at the plasma entrance to $\sigma_r \sim 0.2\,\mathrm{mm}$, but cannot be longitudinally compressed to less than $\sigma_t \sim 255\,\mathrm{ps}$. If the plasma electron density is chosen to satisfy the condition on the bunch duration (Equation 2.8), $n_{pe} \sim 6\cdot 10^9\,\mathrm{cm}^{-3}$. Hence, according to Equation 1.3, $E_{WB} \sim 6\,\mathrm{MV/m}$, which is not interesting for high-gradient acceleration. When satisfying the condition on the bunch radius (Equation 2.9), the density can be high enough to drive wakefields amplitude on the GV/m scale (for $n_{pe} \sim 7\cdot 10^{14}\,\mathrm{cm}^{-3}$, $E_{WB} \sim 2.6\,\mathrm{GV/m}$). Therefore, to reach significant accelerating gradients when using a high energy p^+ drive bunch, one has to choose the plasma electron density based on $k_{pe}\sigma_r \leq 1$, that makes the bunch duration too long for effective wakefields excitation ($\omega_{pe}\sigma_t \sim 600$). However, since the p^+ bunch duration is much longer than the plasma period, it is subject to a transverse beam-plasma instability, called the self-modulation instability (SMI) [48, 71].

2.3   Self-modulation instability

When the long p^+ bunch enters a plasma, the initial noise [72] or imperfections [52] in the charge density distribution of the bunch drive initial transverse wakefields that modulate the radius of the bunch itself, along its longitudinal axis. The modulated bunch density resonantly increases the amplitude of the wakefields, self-reinforcing the self-modulation (SM) until the bunch is fully modulated into a train of microbunches, that develop in the focusing phase of the

wakefields, with modulation period $\sim T_{pe}$. The protons that are in the defocusing phase are defocused out of the wakefields and of the plasma. Since the protons are relativistic, the longitudinal shift of particles along the bunch is negligible in this experiment.

Considering a train of microbunches with microbunch duration T_{bunch} and density $n_b = n_{b0} \cdot \Theta(T_{bunch}c - \xi) \cdot exp(-r\frac{r^2}{2\sigma_r^2})$ with the Heaviside function $\Theta = 1$ when $0 \leq \xi \leq T_{bunch}c$ and 0 otherwise, one can use Equation 2.5 to obtain the transverse wakefields amplitude along the train of microbunches. In [73], the length of the microbunches is set as $k_{pe}L_{bunch} = \pi$, the relative charge of the mth microbunch is increasing along the bunch as $(2m - 1) \cdot Q_{m0}$, with Q_{m0} the charge of the first one, and the microbunches are placed with distance $1.5\,\lambda_{pe}$ to each other ($\lambda_{pe} = \frac{2\pi c}{\omega_{pe}}$ is the plasma electron wavelength). The amplitude of the transverse wakefields at the center of the mth microbunch ξ_{CM} is determined as:

$$W_\perp(\xi, r) = -\frac{qn_{b0}}{\varepsilon_0 k_{pe}}((m-1)^2) + sin(k_{pe}(\xi - \xi_{CM}))(1 - cos(k_{pe}\xi))\frac{dR(r)}{dr}. \quad (2.10)$$

It is therefore shown that the amplitude of the transverse wakefields increases along the bunch ($W_\perp \propto (m-1)^2$) when the microbunches are placed in the right phase and with the right length, here with increasing charge density.

The train of microbunches as considered in [73] is a simplified picture of the self-modulated p^+ bunch. In AWAKE, the charge density of the microbunch follows the initial Gaussian bunch distribution and the microbunches are spaced by $\sim \lambda_{pe}$ due to the self-modulation process. The increase of the amplitude of the transverse wakefields along the bunch was demonstrated in previous experiments [74] and will be discussed again in Section 6.5 and 6.4.

2.3.1 Seeding of the self-modulation

When SM develops from the uncontrolled wakefields initially driven by the p^+ bunch, it occurs as an instability and the timing of the wakefields is not reproducible from event to event. When a seed wakefield is applied, its transverse component determines the first modulation of the radius along the p^+ bunch, from which SM grows. Therefore, the timing of the p^+ driven wakefields is defined by the seed bunch and it is reproducible from event to event.
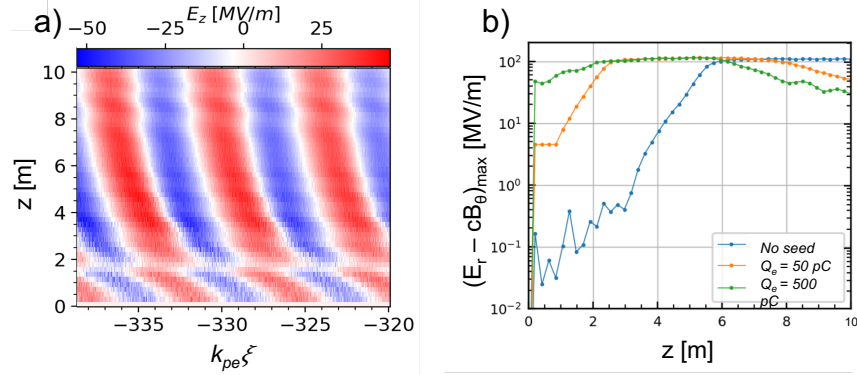
Figure 2.1: a) Waterfall plot of the longitudinal wakefields along the plasma and along a slice of the p^+ bunch $\sim 2\,\sigma_t$ ahead of the center of the bunch. The seed e^- bunch travels $\sim 4\,\sigma_t$ ahead of the center of the p^+ bunch. b) Maximum transverse wakefields driven by the p^+ bunch along the plasma with no seed bunch (blue line), $Q_e = 50\,\mathrm{pC}$ (orange line) and $Q_e = 500\,\mathrm{pC}$ (green line) seed e^- bunch. $n_{pe} = 2 \cdot 10^{14}\,\mathrm{cm^{-3}}$.

The seed wakefields can be driven by a preceding e^- bunch. Figure 2.1a shows simulation results of the longitudinal wakefields along the plasma (vertical axis) and along the bunch (horizontal axis) in a longitudinal slice around $\sim 2\,\sigma_t$ ahead of the center of the p^+ bunch. The seed wakefields are driven by an e^- bunch traveling $\sim 4\,\sigma_t$ ahead of the center of the p^+ bunch. For the first $\sim 2\,\mathrm{m}$ of propagation, the wakefields are mainly driven by the seed bunch. In fact, the slope of the wakefields for $z < 2\,\mathrm{m}$ towards the back of the bunch indicates that the phase velocity of the wakefields is smaller than c, since it is close to that of the drive bunch (for $\gamma = 36$, $\beta = 0.9996$). For $z > 2\,\mathrm{m}$, the phase velocity of the wakefields becomes close to c (the slope becomes larger) and the amplitude increases because the p^+ driven wakefields take over (for $\gamma = 426$, $\beta = 0.999997$), with timing inherited from the seed wakefields. In Section 6.3, I will discuss experimental results showing that a preceding e^- bunch can seed SM in plasma of a long p^+ bunch.

Figure 2.1b shows that, when increasing the charge of the seed e^- bunch, the amplitude of the initial transverse wakefields increases from $\sim 0.1\,\mathrm{MV/m}$ ($Q_e = 0\,\mathrm{pC}$, blue line) to $\sim 4\,\mathrm{MV/m}$ ($Q_e = 50\,\mathrm{pC}$, orange line) and to $\sim 40\,\mathrm{MV/m}$

($Q_e = 500\,\text{pC}$, green line). Moreover, SM reaches saturation earlier along the plasma and with larger wakefields amplitude for larger Q_e. This happens because the initial modulation of the bunch occurs faster when the amplitude of the seed wakefields is larger, and therefore SM develops earlier along the plasma.

2.3.2 Growth of the self-modulation

The transverse wakefields along the propagation distance $z = ct$ of a bunch with constant bunch density n_b that undergoes SM can be written in the linear regime as:

$$W_\perp(n_b, z) = W_{\perp 0} \cdot e^{\Gamma(n_b, z) z}, \tag{2.11}$$

where $W_{\perp 0}$ is the initial ($z = 0$) transverse seed wakefields and $\Gamma(n_b, z)$ is the SM growth rate. An expression for the growth rate using linear wakefields theory is derived with slightly different expressions in [48, 55, 56] as:

$$\Gamma(n_b, z) = \frac{3\sqrt{3}}{4} \omega_{pe} \left(\frac{n_b m_e}{2 n_{pe} m_p \gamma} \frac{\xi}{z} \right)^{1/3}. \tag{2.12}$$

Equations 2.11 and 2.12 show that the growth rate Γ decreases with the propagation distance z as $\propto z^{-1/3}$, while the exponentiation Γz increases as $\propto z^{2/3}$.

The growth rate increases along the bunch as a function of the initial bunch density as $\Gamma \propto (n_b \cdot \xi)^{1/3}$. Therefore, $W_\perp$ also grows along the bunch. When seeding does not take place, $W_{\perp 0}$ depends on n_b (see Equation 2.5). In the case of a p^+ bunch whose SM is seeded by the wakefields driven by a preceding e^- bunch, $W_{\perp 0}$ is the seed wakefields amplitude and it depends solely on the e^- bunch parameters, while Γ depends solely on those of the p^+ bunch. The effect of an increase in $W_{\perp 0}$ or Γ is to increase the amplitude of the wakefields at any time along the bunch, i.e., the SM growth.

As mentioned earlier, the linear approximation of the wakefields is valid only for small radial perturbations of the transverse distribution of the bunch. Over a few meters of propagation in plasma, the depth of the bunch modulation increases significantly and linear theory becomes invalid. Moreover, the protons that are defocused out of the wakefields reach radial distance much larger than the initial bunch radius. However, the defocused protons carry information about the early

times of propagation in plasma, i.e., when SM is not yet saturated, and are subject of the measurements on the growth of the wakefields.

In the experiment presented in this thesis, we provide the seed wakefields using a preceding e^- bunch. So, the amplitude of the seed wakefields $W_{\perp 0}$ and the growth rate Γ of SM are independent from each other. I therefore study the variation of $W_{\perp 0}$ as a function of the properties of the e^- bunch (Section 6.4), and the variation of Γ as a function of the initial p^+ bunch density (Section 6.5).

Chapter 3

Experimental setup and concepts for the measurements

3.1 Experimental setup

AWAKE Run 2a makes use of the existing facility and setup [49] (see Figure 1.3 in Section 1.6). The 10-m-long Rb vapor source provides vapor density in the range $n_{vap} = (0.5 - 10) \cdot 10^{14} \, \text{cm}^{-3}$, measured to better than 0.5% [75]. The vapor source is connected to the beamline at each end through a 1-cm-diameter aperture. An $\sim 120 \, \text{fs}$, $\sim 100 \, \text{mJ}$ laser pulse ($\lambda = 780 \, \text{nm}$) produces a relativistic ionization front (RIF) that creates the plasma by ionizing the rubidium vapor (RbI$\rightarrow$RbII). The plasma column has a radius of approximately $1 \, \text{mm}$ [53]. Previous experiments showed that the RIF ionizes $\sim 100\%$ of the atoms along its path [50], so the density of the plasma is equal to that of the vapor. Hence, in the following $n_{pe} = n_{vap}$. In this work, we use $n_{pe} = (0.97 - 1.02) \cdot 10^{14} \, \text{cm}^{-3}$. The $400 \, \text{GeV/c}$ p^+ bunch is delivered by the CERN SPS with bunch charge Q_p that can be varied in the range $Q_p = (14.7 - 46.9) \, \text{nC}$. The duration of the p^+ bunch is in the range $\sigma_t = (236 - 255) \, \text{ps}$. The RIF is placed $t_p = 620 \, \text{ps}$ ($\sim 2.5 \, \sigma_t$) ahead of the center of the p^+ bunch. At this location, the p^+ bunch density is too low to drive wakefields with amplitude sufficient to seed SM [52].

An ultraviolet (UV) pulse derived from the same laser oscillator as the one

producing the RIF generates an $\sim 5\,\text{MeV}\ e^-$ bunch in a photo-injector [76]. Hence, the e^- bunch is inherently synchronized with the RIF and its timing can be adjusted with a translation stage. The electrons are accelerated to $\sim 18\,\text{MeV}$ with a 1-m-long booster cavity and then transported to the plasma entrance [77]. The charge contained in the e^- bunch Q_e is adjusted in the range $(150 - 800)\,\text{pC}$ by tuning the energy of the UV pulse on the photocathode and measured using a Faraday cup with $20\,\text{pC}$ accuracy [78]. The transverse size and position of the beam along the beamline (upstream of the plasma entrance) is measured using scintillating screens (BTVs) and beam position monitors (BPMs). The emittance of the e^- bunch is measured by measuring the beam transverse size on a BTV while scanning the strength of a quadrupole magnet after the accelerating cavity [79].

Downstream of the plasma exit, there are several diagnostics to measure the properties of the beams after interaction with plasma: an aluminum-coated silicon wafer producing optical transition radiation (OTR) that is imaged on a streak camera, an electron magnetic spectrometer and additional scintillating screens.

The electron beamline

After generation at the photoinjector and acceleration through the booster cavity, the e^- beam is transported through a vertical and a horizontal dispersive sections and merged with the proton beamline to be injected into the plasma. The strength of the quadrupole magnets in the last triplet can be adjusted to move the waist to different locations. During the experiment, the beam is focused at the plasma entrance. During the setup, it is focused at the position of the last BTV ($\sim 0.8\,\text{m}$ upstream of the plasma entrance) to measure the bunch transverse size, and at the position of an OTR screen ($\sim 2.8\,\text{m}$ upstream of the plasma entrance) to measure the bunch length.

As the electrons have low energy and the transfer beamline is not shielded from external magnetic fields, the trajectory of the e^- beam (blue arrow) is affected by the Earth's magnetic field. As shown schematically in Figure 3.1, the trajectory of the p^+ beam (red arrow) is essentially straight, while that of the e^- beam is bent by the Earth's magnetic field. The amplitude of the magnetic field in the experimental hall was measured $B_{x,y} \sim (0.2, 0.4)\,\text{G}$, (with a $\pm 15\%$ uncertainty),

corresponding to Larmor radii $R_{x,y} = \beta\gamma m_e c/eB_{y,x} \sim (1.5, 3)$ km. To effectively seed SM of the p^+ bunch, the seed wakefields must be aligned with the p^+ beam trajectory. Therefore, the e^- beam trajectory must be aligned in position and angle onto that of the p^+ beam at the plasma entrance. We use the last two corrector magnets upstream of the vapor source entrance to align the trajectory of the e^- beam on that of the p^+ beam [80, 81, 82]. Once inside of the vapor source, both beams travel on a straight trajectory, as the vapor source is shielded from external fields with a layer of mu-metal.
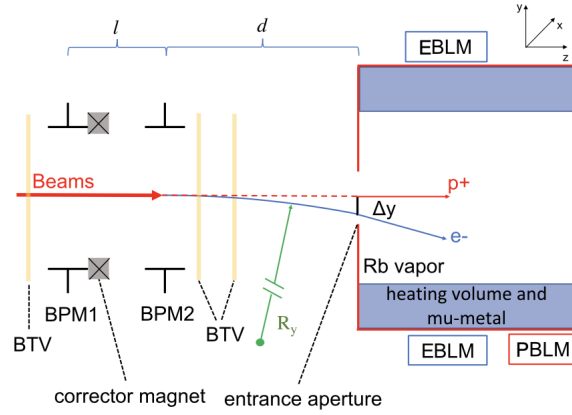

Figure 3.1: Schematics of the proton and electron beam transfer line and vapor source close to the entrance of the vapor source. Beams are overlapped at the last two BPMs: The p^+ beam propagates essentially straight (red arrow); the e^- beam trajectory (blue) is bent by the Earth's magnetic field with radius of curvature R_y. Δy is the deviation from the straight trajectory in the vertical plane. The drawing is not to scale. Figure from [81].

BPMs and BTVs

The trajectory of the e^- beam is monitored using 12 BPMs installed along the line [83]. A corrector magnet is paired with each BPM to correct for misalignment. Five BTVs are located along the electron beamline [84]. When the beam goes through a scintillaing screen, it deposits energy that is then re-emitted by the screen as visible light. The light is collected by a digital camera that produces

a time-integrated image of the transverse charge distribution of the beam. The beams have transverse Gaussian profiles, so the transverse size of the beam is measured by performing a Gaussian fit to the projections on the orthogonal axes.
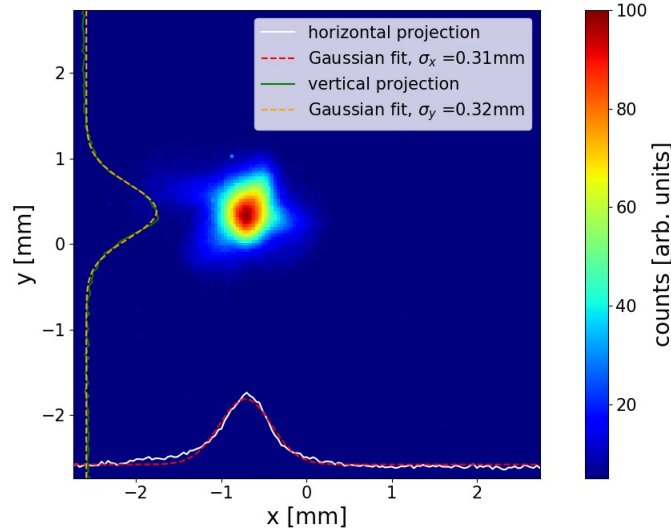

Figure 3.2: Electron beam imaged at the last BTV upstream of the plasma entrance. White and green continuous lines are the projections obtained as a sum of the counts on the horizontal and vertical axis, respectively. Red and yellow dashed lines are the Gaussian fit for each projection. The values of the transverse size $\sigma_{x,y}$ obtained from the fits are reported in the legend.

Figure 3.2 shows an image produced by the last BTV upstream of the plasma entrance. The e^- beam is focused at the screen. The Gaussian fits (red and yellow dashed lines) are in good agreement with the transverse projections (white and green lines). Therefore, the value of σ of the Gaussian function corresponds to the rms transverse size of the beam in each plane. In the following, the same colorbar as in Figure 3.2 is used for all images to indicate the number of counts per pixel, unless differently specified.

OTR foil and streak camera

When the p^+ bunch enters a 280-µm-thick silicon wafer coated with 1-µm-thick layer of mirror-finished aluminum, positioned 3.5 m downstream of the plasma exit, optical transition radiation (OTR) is emitted [50, 85]. The spatial and temporal distribution of the OTR represent the shape of the bunch at the screen. The OTR is imaged onto the entrance slit of a streak camera. Inside the streak camera, a photocathode converts the photons that pass through the slit into electrons. Electrons are multiplied by a micro-channel plate before the phosphor screen. Their trajectory is then bent through a streak tube onto a phosphor screen. The transverse bending voltage of the streak tube varies as a function of time and can be adjusted from the ps to ns timescale. Therefore, depending on the time of arrival of each photon on the photocathode, the trajectory of the corresponding emitted electrons is bent weaker or stronger and thus the electrons reach the phosphor screen on a different transverse position. The light emitted by the screen is imaged onto a CMOS camera. We use a streak camera produced by Hamamatsu (model C10910-05) with a 16-bit, 2048x2048 pixel ORCA-Flash4.0 CMOS sensor, binned to 512x672 pixels for streak operation.
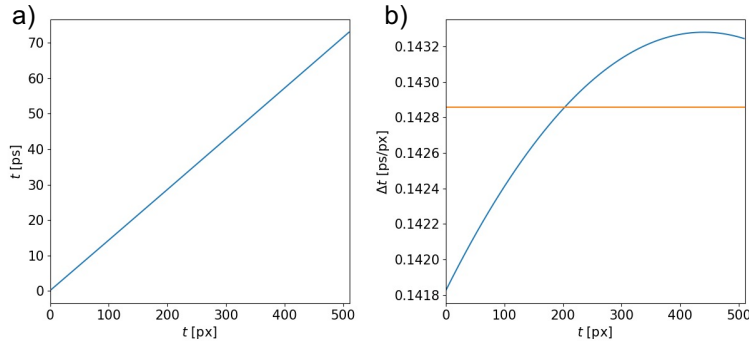

Figure 3.3: a) Time along 73 ps-scale time-resolved images. b) Time duration of the pixels along the images before (blue line) and after (orange line) linear interpolation of the time axis.

The time duration of the acquisition window can be varied between 73 ps and 56 ns. In the following, we use the shortest time windows (73 ps and 210 ps),

when we we want to study the structure of the microbunch train. In this case, the streak dynamics limit the temporal resolution to $\sim 1\,\mathrm{ps}$ [85, 74] We use a longer time window ($1.1\,\mathrm{ns}$), with longer temporal resolution, when we study the charge density distribution along the entire bunch. The spatial resolution of the system is $\sim 180\,\mathrm{\mu m}$ [74].

Since the sweeping time of the voltage inside of the streak tube is not constant over one acquisition, the time axis of the image is slightly non-linear. Figure 3.3(a) shows the time along a $73\,\mathrm{ps}$-scale time-resolved image Figure 3.3(b) shows the duration in time of each pixel as given by the manufacturer (blue line). Even though the deviation from linear is very small (the maximum difference of time duration between pixels is 1%), all images and their time axis are linearly interpolated in this thesis, so that each pixel corresponds to the same time interval (orange line).
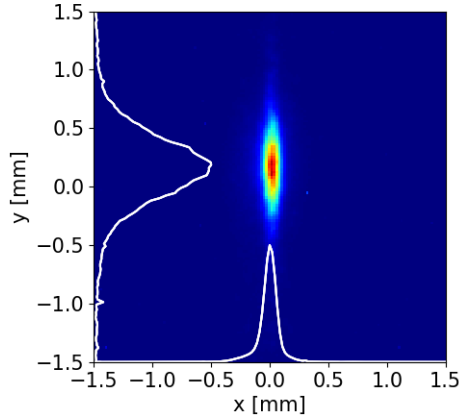
Figure 3.4: Time-integrated, transverse image of the p^+ bunch obtained using the streak camera while no sweeping voltage is applied. The slit width is $20\,\mathrm{\mu m}$. The image shows a restricted region of interest around the center of the distributon. White lines show the projections on the orthogonal axis.

The OTR goes through a slit before reaching the photocathode inside the streak camera. Thus, we obtain time-resolved images of a longitudinal slice of the three-dimensional distribution. In the experiment, we are normally interested in measuring the charge density distribution of the longitudinal slice on the beam

propagation axis, that is the axis of symmetry of the self-modulation. We therefore align the optical line so that the transverse distribution of the signal is centered on the center of the slit. To maximize the resolution, in the following the width of the slit is always set at its minimum value (20 µm). Figure 3.4 shows an image of the p^+ bunch, when no sweeping voltage is applied in the streak tube. As a consequence, the streak camera provides a time-integrated, transverse image of the charge density distribution. The distribution in the horizontal direction is clipped by the 20-µm-wide slit of the streak camera, as also shown by the projections on the orthogonal axis (white lines). The rms of the distribution in the horizontal plane is 0.16 mm. This is larger than the width of the slit due to the spatial resolution of the instrument (one pixel corresponds to 0.0217 mm).

The energy of the electrons emitted by the photocathode depends on the cathode radiant sensitivity (Figure 3.5). This represents the responsivity of the cathode to radiation and it is defined as the ratio between the current transmitted by the photocathode and the incident radiant power. When the light signal is not monochromatic, the energy spectrum of the electrons has a finite distribution. This may result in a different effect of the bending voltage on the electrons in the streak tube, resulting in a larger timing uncertainty on the final signal.

For the streak camera photocathode used in the experiment (purple line) the radiant sensitivity has a peak around $\lambda = 450$ nm and decreases exponentially for shorter and longer wavelengths. As the OTR is not monochromatic, we use a 25 nm band-pass filter around 450 nm in the optical line to limit the bandwidth of the signal. This ensures a uniform response of the photocathode and the time resolution of the system [85].

During the measurements with plasma, the ionizing laser pulse is stopped by a hard-tempered 200-µm-thick aluminum foil (laser beam dump) at the plasma exit so as to protect the screen and the streak camera.

A second OTR-streak camera system is used to measure the length of the e^- bunch (see Section 3.2.4).
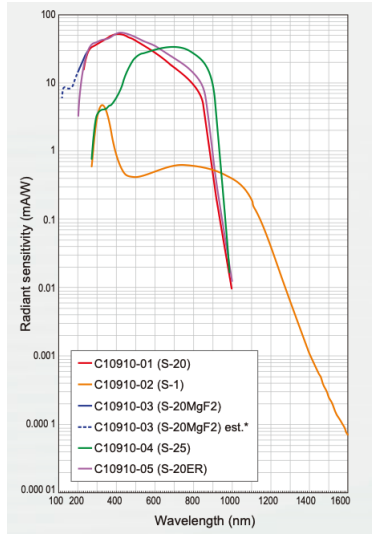
Figure 3.5: Radiant sensitivity of the photocathode as a function of the wavelength of the incident radiation. Specifications provided by the manufacturer [86].

Electron beam spectrometer

The electron beam spectrometer is composed by a quadrupole magnet doublet and a dipole magnet [87, 88] bending the e^- beam onto a scintillating screen positioned 8 m downstream of the plasma exit. Thus, the electrons are dispersed according to their energy. The light emitted by the screen is collected by an intensified camera, producing energy-resolved images.

Imaging stations

Two imaging stations (IS 1 and IS 2) are located 2 and 10 m downstream of the plasma exit [89] (see Figure 3.6(a)). Each of them is composed of a scintillating screen and an optical line splitting the light into two different paths, as shown in Figure 3.6(b). The light is then collected by digital cameras. One optical line on each station images the light directly on a camera. These are called *core* cameras, because they are dedicated to detect the bright signal from the inner core of the bunch. A mask is placed in the other optical line on each station so as to filter the light of the bunch core, before reaching the camera. These are called *halo*

cameras, because they are dedicated to detect the much less intense signal from the outer halo of the bunch. The transmission of the masks is 11.3% and 12.3% for IS 1 and for IS 2, respectively. The imaging stations are used to measure the transverse, time-integrated distribution of the p^+ bunch. In particular, we measure the transverse extent from the propagation axis reached by the protons that are defocused during SM [51]. Combining the halo and core images for each IS allows to increase the dynamic range of the detection system by one order of magnitude.

Figure 3.6: a) Schematic location of the imaging stations (IS1 and IS2) and of the OTR screen with respect to the plasma. The p^+ bunch moves from left to right. b) Schematic drawing of the optical setup of the imaging stations. Figure from [51].

3.2   Measurements

In this Section I illustrate the concepts for the measurements that I performed and how I made use of the diagnostics to extract information about the physics processes. The experimental results are discussed in Chapter 6.

3.2.1 Electron deceleration in plasma

The topic of this work is the seeding of the self-modulation instability of a long p^+ bunch in plasma using a short, preceding e^- bunch. Previous experiments showed that the amplitude of the seed wakefields must be larger than a threshold to effectively seed SM [52]. Therefore, we want to estimate the wakefields amplitude that can be driven by the e^- bunch.
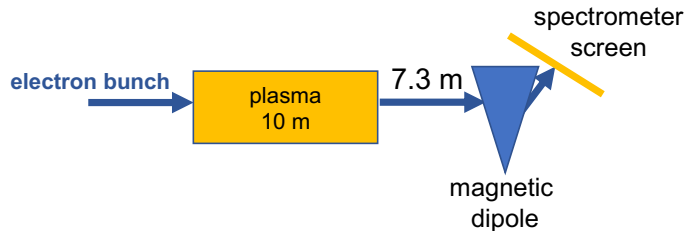

Figure 3.7: Schematic of the setup for the electron deceleration experiment.

Since there is no wakefields diagnostics installed along the plasma, we gain information on the wakefields driven by the e^- bunch by measuring its energy spectrum with the electron spectrometer. Figure 3.7 shows a schematic of the relevant equipment. The electrons that exit the vapor source through the 1-cm-diameter aperture, travel in vacuum and their trajectory is deflected according to their energy by the magnetic field of a dipole positioned 7.3 m downstream of the plasma exit. Then, they impact on a scintillating screen whose emitted light is collected by an intensified camera. Figure 3.8 shows an image of the e^- bunch with $Q_e = 250$ pC on the spectrometer screen after propagation in vacuum (a) and the projection on the energy axis (b). The energy spectrum is centered around the initial energy $E_{in} = (18.35 \pm 0.05)$ MeV (red dashed line in (b)). The beam is focused at the entrance of the vapor source (18 m upstream of the spectrometer screen) with transverse size in the range $\sigma_r = (0.2-1.3)$ mm and the Twiss parameter $\beta \sim 1$ m. Afterwards, the beam defocuses and reaches the exit of the source with a transverse size larger than the exit aperture and the transverse distribution of the beam is therefore clipped. Indeed, the vertical distribution of the beam at the screen is a "shadow" of the exit aperture, while the horizontal

distribution is a convolution of spatial and energy distribution. In fact, the rms of the energy spectrum in Figure 3.8(b) is $0.5\,\mathrm{MeV}$, that is larger than the nominal energy spread of the beam ($\sim 0.1\,\mathrm{MeV}$ [77]). To estimate the minimum energy E_{min}, I calculate the energy where the energy projection reaches the 10% of its peak value (green dot in the (b)).
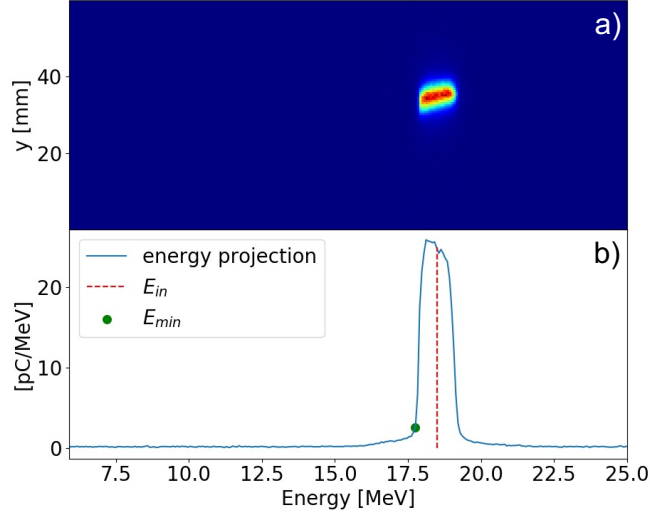

Figure 3.8: a) Image of the e^- on the spectrometer screen, after propagation in vacuum b) Blue line: energy projection, red dashed line: initial energy E_{in}, green dot: minimum energy E_{min}.

The e^- bunch loses energy driving wakefields, while it travels in plasma (see Figure 6.1 in Section 6.1). Thus, the energy spectrum extends to lower energies with plasma than without. In this case, the horizontal distribution at the spectrometer screen is dominated by the energy spectrum.

The maximum energy lost by the e^- bunch $\Delta E = E_{in} - E_{min}$ depends on the amplitude of the longitudinal wakefields E_z along the plasma as:

$$\Delta E = q \int_0^{10\,m} E_z(z)\,dz. \tag{3.1}$$

Due to the complex evolution of the e^- bunch along the plasma (see Chapter 5), the amplitude of E_z is not constant along the plasma. Thus, it cannot be calculated directly from the value of the maximum energy loss.

The optical system has been calibrated to convert digital *counts* in a value of charge reaching the screen of the spectrometer. The conversion factor is $7.4 \cdot 10^4$ digital counts/pC. The results of the measurements are discussed in Section 6.1.

3.2.2 Self-modulation timing reproducibility

The self-modulation instability of the p^+ bunch develops from the wakefields driven by the noise [72] or by the imperfections [52] within the initial bunch charge distribution. Therefore, the amplitude and timing of the wakefields varies from event to event. When SM is seeded, the timing of the wakefields is locked to the timing of the seed and the amplitude grows from the seed wakefields amplitude. Thus, when seeded, the amplitude and the timing of the wakefields are reproducible. The microbunches develop in the focusing phase of the wakefields, thus the timing of the microbunch train is tied to that of the wakefields. Therefore measuring the timing reproducibility of the microbunch train is equivalent to measuring that of the wakefields.
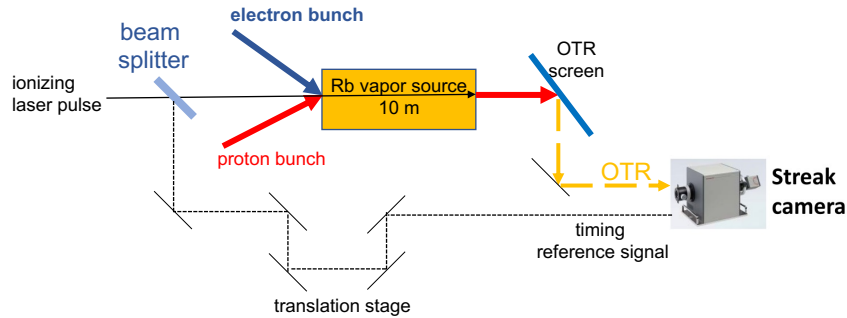

Figure 3.9: Schematics of the experimental setup used for the timing reproducibility measurement. The timing reference signal is generated as a reflection of a fraction of the ionizing laser pulse with a beam splitter. The timing of the timing reference signal is adjusted with a translation stage.

To study the structure of the microbunch train and to measure the timing reproducibility, we use the streak camera with its shortest time window (73 ps), so that the time resolution is short enough (~ 1 ps [74]) to resolve in time the

single microbunches. In the experiment described here, $n_{pe} = 0.97 \cdot 10^{14}\,\mathrm{cm}^{-3}$ and the plasma electron period (i.e., the period of the wakefields) $T_{pe} = 11.15\,\mathrm{ps}$.

The streak camera is triggered by an external signal, synchronized with the RIF, but the overall streak camera triggering system has a jitter of $\sim 4.8\,\mathrm{ps}$ rms, that is much larger than the time precision needed to perform the measurement. In order to align the images in time with ps-precision, we use a timing reference signal (a mirror bleed-through of the RIF) that is transported to the slit of the streak camera [90]. Figure 3.9 shows a schematics of the setup used for the measurement. The timing reference signal is synchronized with the RIF and its time of arrival at the slit can be adjusted with a translation stage. Figure 3.10(a) shows 3 consecutive $73\,\mathrm{ps}$-scale time-resolved images of the microbunch train (centered around $y = 0\,\mathrm{mm}$) and of the timing reference signal (at $t = 0\,\mathrm{ps}$ highlighted in the red circles). The bunch travels from left to right. By performing a Gaussian fit of the time profile on each image in the region where the reference signal appears, I measure its center value. I then shift each image along the time axis so that the center of the signal occurs at the same t on all images, as in Figure 3.10(b). The red dotted line show the time $t = 0\,\mathrm{ps}$ on which all images are aligned. With this method, we obtain the necessary precision to perform the measurement of timing reproducibility. In fact, the timing of the features along the time-resolved images (i.e., the microbunches) can be referred in time to the other images with sub-ps accuracy.

In this experiment, we seed SM of the p^{+} bunch with the wakefields driven by the preceding e^{-} bunch. Since both the seed e^{-} bunch and the timing reference signal are synchronized with the RIF, measuring the timing reproducibility of the modulation with respect to the timing reference signal is equivalent to measuring it with respect to the seed bunch. The results of the measurements on the timing reproducibility of SM seeded by the e^{-} bunch are discussed in Section 6.3.
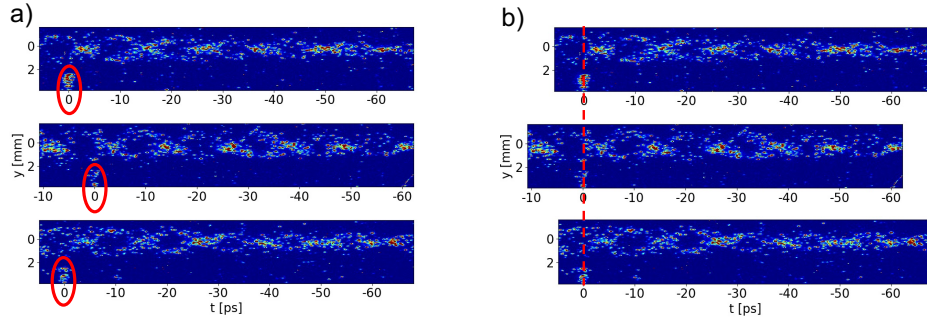
Figure 3.10: a) Three consecutive 73 ps-scale time-resolved images showing the microbunch train and the timing reference signal. The time $t = 0$ ps corresponds to the time of the reference signal on each image. b) Same events after timing alignment with respect to the center of the timing reference signal (red dashed line).

3.2.3 Variation of the seed wakefields amplitude and of the growth rate of the self-modulation

During the SM growth, a large fraction of the protons in the bunch are defocused out of the wakefields. Afterwards, these protons travel with a straight trajectory defined by the transverse momentum $p_\perp$ that they acquire from the wakefields, according to:

$$p_\perp = \frac{e}{c} \int_0^D W_\perp(z)\, dz, \tag{3.2}$$

where $W_\perp$ is the transverse wakefields and $D \leq L$ (L the plasma length) is the location along the plasma where they leave the wakefields. As SM takes place in the first meters of propagation in plasma, defocused protons carry information about the development of SM before saturation occurs [51, 91]. The transverse momentum acquired by each defocused proton defines the transverse position that the particle will reach at any position downstream of the plasma. Thus, the transverse distribution of the bunch, after propagation in plasma, is related to the amplitude of the wakefields experienced by the defocused protons.

We measure the width of the transverse distribution along the bunch to study the growth of the self-modulation. Since the wakefields grow along the bunch [51, 74], we use the OTR-streak camera system to obtain time-resolved images of the transverse distribution of the p^+ bunch. In this case, we study the evolution over

long time scales ($> 1/\omega_{pe}$) with the 1.1 ns-scale time window. The time resolution of the streak camera when using the ns-scale is not short enough to evidence the microbunch train (whose periodicity is $2\pi/\omega_{pe}$) and thus the p^+ bunch distribution appears continuous also after propagation in plasma.
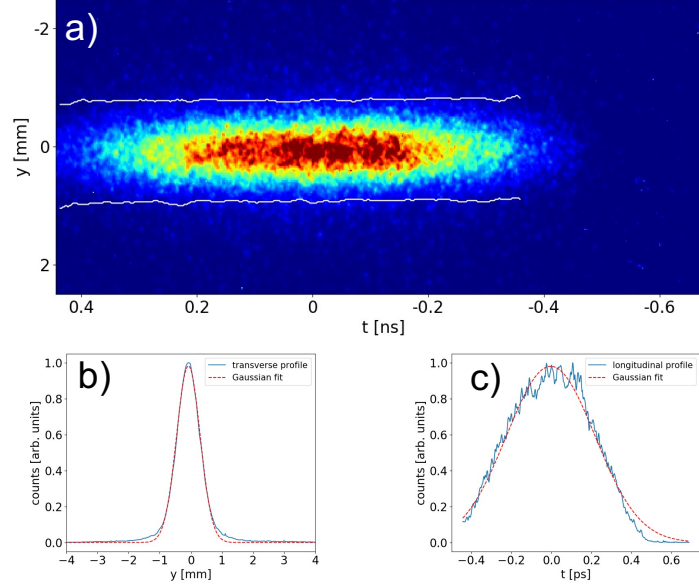

Figure 3.11: a) 1.1 ns-scale time-resolved image of the p^+ bunch. The white lines indicate the points where the transverse distribution crosses the 20% threshold (white lines) at any given time. b, c) Transverse and longitudinal projections, summing the counts of (a) along the horizontal and vertical axis, respectively. The red dashed lines show the Gaussian fits: $\sigma_y = 0.38\,\text{mm}$ (b), $\sigma_t = 255\,\text{ps}$ (c).

Figure 3.11(a) shows a 1.1 ns-scale time-resolved image of the p^+ bunch after propagation in vacuum. By summing the counts along the horizontal (t) and vertical (y) axis, I obtain the transverse (Figure 3.11(b)) and longitudinal (Figure 3.11(c)) projections, respectively. The Gaussian fits (red dashed lines) are in agreement with the projections (blue lines), although with some discrepancy on the tails of the distributions. The discrepancy in the transverse projection may be due to the fact that the transverse distribution is composed by a mixture of two bivariate Gaussian distributions [92], one of which defines the enlargement of the outer part of the bunch. The discrepancy in the longitudinal projection is

due to the low amplitude of the signal at the front of the bunch, that becomes smaller than the detection threshold.

During the experiment, I measure the width along the bunch of the self-modulated p^+ bunch. The blue line in Figure 3.12(a) shows a typical transverse profile of a time-column of a time-resolved image, after the p^+ bunch has propagated in plasma. The transverse distribution is not Gaussian anymore because the transverse wakefields are radially non-linear. Therefore, one cannot use a Gaussian fit to estimate the transverse size of the bunch. To quantify the transverse size along the bunch, on each time column I measure the points where the transverse distribution reaches 20% of its maximum, defining the contours of the distribution. The distance between these points defines the transverse extent w. This method of determination of the transverse extent is independent of the shape of the distribution (unlike, for example, the rms). The arbitrary choice of the value of the threshold does not affect the results. I choose 20% so that the points where the distribution crosses the threshold are above the noise and can be uniquely determined. As shown in Figure 3.12(a), the raw transverse profile (blue line) of a time-column is noisy and the random fluctuations may influence the contour determination. Thus, I bin the transverse distribution so as to smooth the profile (orange line).

In case of propagation without plasma, the transverse distribution is Gaussian and represents the incoming bunch (from Figure 3.11(c), $\sigma_y = 0.38\,\text{mm}$). The expected transverse extent is $w = 2\sigma_y\sqrt{-2log(0.2\sigma_y\sqrt{2\pi})} = 1.38\,\text{mm}$. Figure 3.12(b) shows the binned transverse profile from Figure 3.11(a) at $t = 0$ (i.e., center of the bunch, blue line), 1 and $1.5\,\sigma_t$ (orange and green lines) ahead of the center of the bunch. The red points show the transverse contours of the bunch at the corresponding time. The transverse extent measured on Figure 3.11(a) is $w_{off} = 1.7\,\text{mm}$, constant along the bunch (white lines in Figure 3.11(a) show the contours) and represents the transverse size along the bunch. This value is larger than the expected one because of the broadening introduced by binning the distribution.

Figure 3.12(c) shows the binned transverse distribution of the p^+ bunch after propagation in plasma at different locations along the bunch. The transverse

extent w (distance between the red points) clearly increases with the broadening
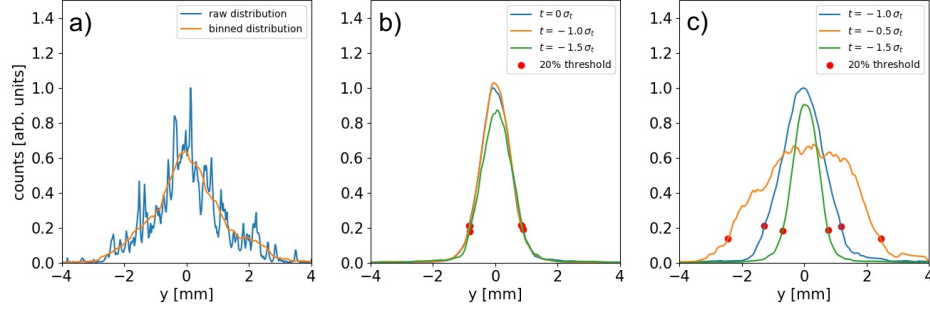of the distribution.

Figure 3.12: a) Transverse distribution of a single time-column of the p^+ bunch charge
density distribution after propagation in plasma. Raw distribution: blue line, binned
distribution: orange line. Each point of the binned distribution is obtained as the average
of 40 consecutive points of the raw distribution. Counts are normalized with respect to
the maximum value of the raw distribution. b) and c) Transverse distribution without (b)
and with (c) plasma at three different times along the bunch (see legends). In (b) counts
are normalized with respect to the maximum value of the $t = 0\,\sigma_t$ distribution. In (c)
counts are normalized with respect to the maximum value of the $t = -1.0\,\sigma_t$ distribution.
Each point of the distributions is the average of 40 points and the red points indicate
where each distribution reaches the 20% threshold. The distance between the red points
of each distribution defines the transverse extent w.

In this experiment, we measure the transverse extent w along the bunch for
different values of the seed e^- bunch charge Q_e and of the p^+ bunch charge Q_p
to measure their effect on $W_{\perp 0}$ and Γ. The parameters of the p^+ bunch for the
different charges are listed in Table 3.1. Varying the charge of the p^+ bunch Q_p
affects the optics of the beam in the SPS and in the transfer line. Therefore
also the bunch emittance, duration and transverse size change. Since the bunch
density appears explicitly in the expression of Γ (Equation 2.12), we calculate the
density of the bunch n_p at the plasma entrance as:

$$n_p = \frac{Q_p/e}{(2\pi)^{3/2}c\sigma_t\sigma_x\sigma_y}.\tag{3.3}$$

We measure σ_t for the different values of Q_p by performing a Gaussian fit of
the longitudinal profile of 1.1 ns-scale time-resolved images with no plasma, as in

Figure 3.11(c). We calculate $\sigma_{x,y}$ at the entrance of the plasma measuring the transverse size at multiple BTVs upstream and downstream of the plasma [92]. Figure 3.13 shows that n_p increases as a function of Q_p.

Table 3.1: Parameters of the p^+ bunch used in the experiment. The uncertainties on Q_p, $\sigma_{x,y}$, σ_t are the standard deviations obtained from repeated measurements. Q_p is measured in the SPS extraction line with a beam current transformer. The uncertainty on $\epsilon_{x,y}$ is the accuracy of the emittance measurement in the SPS [93, 94]. The uncertainty on n_p is obtained propagating the error from Q_p and on the geometrical parameters (see Equation 3.3).

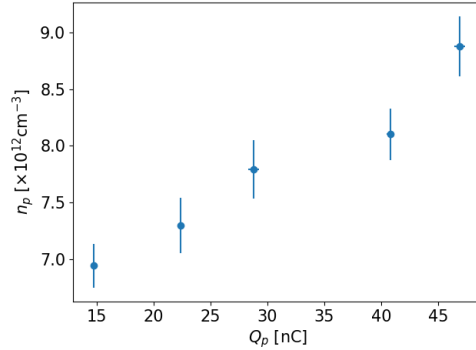| Q_p [nC]	$\sigma_{x,y}$ [$\pm 0.002\,\mathrm{mm}$]	σ_t [ps]	$(\epsilon_{x,y} \pm 20\%)$ [mm mrad]	n_p [$\times 10^{12}\,\mathrm{cm}^{-3}$]
(14.7 ± 0.2)	0.113, 0.112	(255 ± 4)	1.4, 1.4	(6.9 ± 0.2)
(22.4 ± 0.2)	0.129, 0.128	(244 ± 4)	1.5, 1.5	(7.3 ± 0.2)
(28.8 ± 0.5)	0.148, 0.139	(237 ± 5)	1.8, 1.8	(7.8 ± 0.3)
(40.8 ± 0.3)	0.169, 0.167	(236 ± 5)	2.2, 2.2	(8.1 ± 0.2)
(46.9 ± 0.5)	0.175,0.167	(239 ± 6)	3.4, 2.5	(8.8 ± 0.3)

Figure 3.13: p^+ bunch density n_p as a function of the bunch charge Q_p. The error bars are obtained from the standard deviation from the measurement of σ_t, σ_r and Q_p and indicate the variation from event to event of the parameters of the incoming bunch.

The parameters of the e^- bunch for the different values of the charge Q_e are listed in Table 3.2. Since the bunch evolves strongly as soon as it enters the plasma (see Chapter 5), I do not quote the initial density of the bunch.

The results of the measurements on the variation of the seed wakefields am-

plitude and of the growth rate are discussed in Sections 6.4 and 6.5.

Table 3.2: Parameters of the e^- bunch used in the experiment. The uncertainties on Q_e and on $\sigma_{x,y}$ are the standard deviation obtained from repeated measurements. The error on $\epsilon_{x,y}$ is the uncertainty on the parabolic fit of the quadrupole magnet scan [79]. The bunch duration σ_t is measured as discussed in the following Section.

Q_e	$\sigma_{x,y}$ [mm]	σ_t [ps]	$\epsilon_{x,y}$ [mm mrad]
$(147 \pm 22)\,\mathrm{pC}$	$(0.15 \pm 0.04), (0.22 \pm 0.01)$	~ 6	$(0.9 \pm 0.1), (0.8 \pm 0.1)$
$(249 \pm 17)\,\mathrm{pC}$	$(0.27 \pm 0.05), (0.27 \pm 0.02)$	~ 6	$(1.5 \pm 0.1), (1.2 \pm 0.2)$
$(777 \pm 29)\,\mathrm{pC}$	$(0.44 \pm 0.03), (0.41 \pm 0.01)$	~ 6.7	$(3.3 \pm 0.3), (4.3 \pm 0.3)$

3.2.4   Electron bunch duration

To measure the duration of the e^- bunch, we use an OTR screen located $\sim 2.8\,\mathrm{m}$ upstream of the vapor source entrance. A dedicated beam optics is used during this measurement to focus the e^- beam at the location of this screen. The OTR is imaged on the entrance slit of a second streak camera. Due to the small amount of OTR produced and transported to the streak camera, it is not possible to insert any band-pass filter and the measurement relies on the average of many single-event images, aligned in time using the ionizing laser pulse as a timing reference signal. Moreover, the photocathode of the streak camera does not respond uniformly for different OTR wavelengths (see Section 3.1) and the OTR signal is elongated due to the dispersion in the lenses in the optical line.

Figure 3.14a shows the average of 100 single-event time-resolved images. At $t = 0\,\mathrm{ps}$, the low-power ionizing laser pulse is clearly visible. The e^- bunch with $800\,\mathrm{pC}$ follows, with its center $\sim 33\,\mathrm{ps}$ behind the laser pulse. To measure the duration of the e^- bunch, I perform a Gaussian fit on the longitudinal profile, obtained by summing the counts in the transverse direction ± 20 pixels around the bunch centroid, as in Figure 3.14(b). For Q_e in the range between 200 and $800\,\mathrm{pC}$, the e^- bunch duration is measured between $\sigma_t = 6$ and $6.7\,\mathrm{ps}$ (corresponding to bunch length $\sigma_z = 1.8$ and $2\,\mathrm{mm}$). Because the measurement is affected by the averaging of many low-amplitude-signal images and by the long resolution of the

system, these values are upper limits on the real value of the e^- bunch duration, while the lower limit is given by the duration of the UV pulse ($\sigma_t \sim 2\,\mathrm{ps}$).
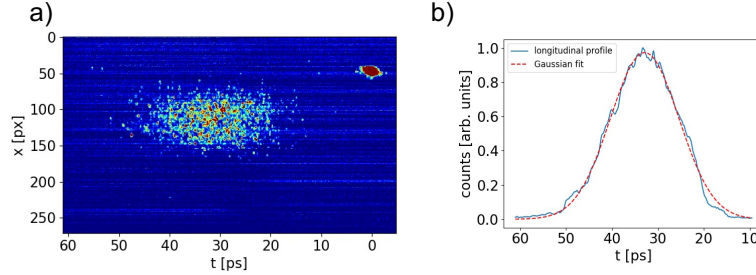

Figure 3.14: a) Average of 100 consecutive 73 ps-scale time-resolved single-event images of the e^- bunch (center at $t \sim 35\,\mathrm{ps}$) aligned in time using the low-power ionizing laser pulse (at $t = 0\,\mathrm{ps}$). The color scale is saturated to make the e^- bunch more visible. b) Longitudinal profile of the e^- bunch (blue line), obtained as a sum of the pixels in the transverse direction between ± 50 pixels around the centroid of the bunch. The red dashed line shows the Gaussian fit.

3.2.5 Three-dimensional self-modulation imaging

To obtain time-resolved images of a slice centered around the propagation axis of the p^+ bunch (where the microbunches develop), we align the OTR on the center of the entrance slit of the streak camera. We can also acquire images of longitudinal slices at different transverse positions by shifting the center of the OTR distribution at a higher or lower position with respect to the center of the slit. We vary the alignment of the OTR with respect to the slit by varying the position of the last reflecting mirror (0.95 m before the slit). The distance between the slit and the mirror is much longer than the variation of the OTR position at tge slit ($< 1\,\mathrm{mm}$) that the change in angle of the OTR is negligible. Effectively, we vary the position of the slit across the transverse distribution of the p^+ bunch, as shown by the red boxes in Figure 3.15(a).

To quantify the change in position introduced by moving the mirror, I scan its position while recording time-integrated images with the streak camera. Figure 3.15(b) shows that the sum of the counts of each image (blue points) follows

a Gaussian distribution, as a function of the position of the mirror. This is expected, since the transverse distribution of the p^+ bunch at the OTR screen is Gaussian (see Figure 3.11(b)). I therefore perform a Gaussian fit (red dashed line, $\sigma = 28.2$ steps). In this case, the rms transverse size at the screen is $\sigma = 0.27$ mm, thus one step variation of the mirror's position corresponds to a vertical shift of 0.01 mm of the OTR at the slit.

For this experiment, I collect sets of 210 ps-scale time-resolved images of the self-modulated p^+ bunch at different mirror's positions. Combining the averaged images obtained at different slices provides three-dimensional images of the p^+ bunch charge density distribution. I use the resulting images to study the evolution of the microbunches in the plane perpendicular to the slit. The results are discussed in Section 6.7.
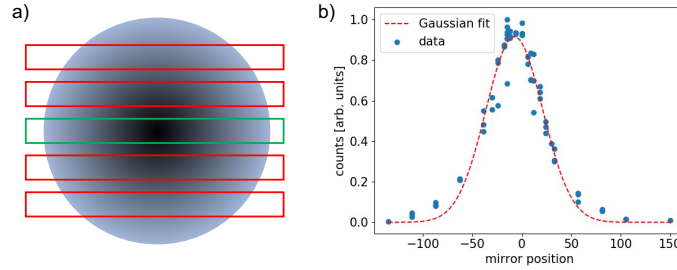

Figure 3.15: a) Schematics of the OTR transverse distribution at the slit of the streak camera. In normal operation, the signal is centered on the slit (green box). When misaligning the OTR with respect to the slit, we effectively change the position of the slit with respect to the signal. The red boxes show examples of misaligned positions of the slit. b) Sum of the counts of time-integrated images of the p^+ bunch obtained with the streak camera (see Figure 3.4) as a function of the position of the mirror. Blue points: data, red dashed line: Gaussian fit.

Chapter 4

Previous experimental results

In this Chapter I summarize the main experimental results obtained in AWAKE during Run 1 (2016-2018). The experimental setup is the one discussed in Section 1.6, Figure 1.3.

4.1 Self-modulation of the proton bunch in plasma

It has been shown in simulations and experiments that long lepton beams self-modulate in plasma [71], and that it is possible to seed the instability by tailoring the bunch distribution [95]. The self-modulation of a long p^+ bunch was discussed in theory and simulations [48], showing that the p^+ bunch self-modulates into a train of microbunches, with the frequency of the modulation equal to the plasma electron frequency. The concept of the ionization-front seeding was already included, by considering a hard-cut half-Gaussian initial charge density distribution of the bunch.

The first experimental demonstration that the p^+ bunch self-modulates in plasma is presented in [50]. Figure 4.1(a) shows a 210 ps-scale, single-event, time-resolved image. The train of microbunches is clearly visible on the propagation axis, as well as the defocused protons off axis. The red line indicates the time of the ionization front. The on-axis profile (green line) shows full modulation (i.e., no charge left between the microbunches) because SM reaches saturation before
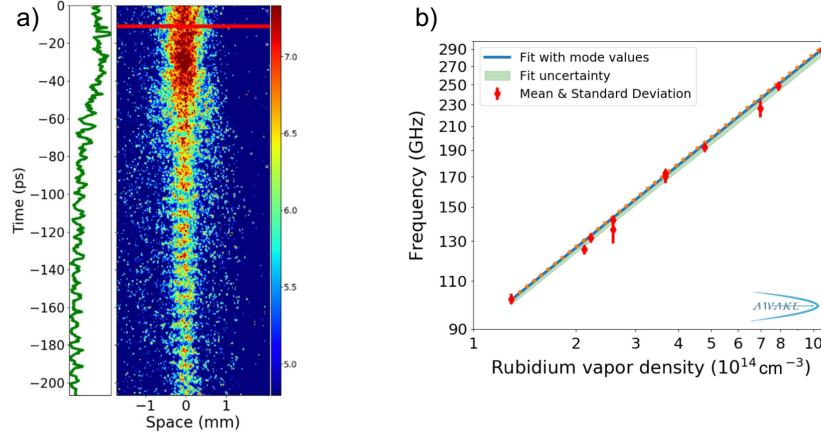
the p^+ bunch leaves the plasma.

Figure 4.1: a) 210 ps-scale, single-event, time-resolved image of the p^+ bunch with $Q_p = 48\,\text{nC}$ in plasma with $n_{pe} = 2.19 \cdot 10^{14}\,\text{cm}^{-3}$. The red line shows the timing of the ionization front. The green line is the on-axis longitudinal profile. b) Measured mean modulation frequency (red dots, with standard deviation of the measured frequencies) as a function of the Rb vapor density on a log-log plot. Figures from [50].

Since the microbunches develop in the focusing phase of the wakefields, the frequency of the charge distribution is expected to match that of the wakefields, that is the plasma electron frequency. The modulation frequency is obtained from the DFT on the time-resolved charge density distribution, as discussed in Section 3.2.2. In this work, the density of the Rb vapor is varied in the range $n_{vap} = (1.5 - 10) \cdot 10^{14}\,\text{cm}^{-3}$. Figure 4.1(b) shows that the measured modulation frequency (red points) is in very good agreement with the expected plasma electron frequency (orange dotted line) over the entire range. This demonstrates that the relativistic ionization front ionizes $\sim 100\%$ of the Rb atoms on its path ($n_{pe} \sim n_{vap}$) and that SM occurs at the expected frequency.

4.2 Growth of the wakefields amplitude

During the development of SM, the amplitude of the wakefields is predicted to grow [55, 56], reaching the maximum value when the bunch reaches full mod-

ulation. In case of seeding, the initial amplitude is that of the seed wakefields. The first experimental proof of growth of the plasma wakefields driven by a self-modulated bunch is presented in [51], as a joint publication with the one discussed in the previous Section. In this work, the maximum radial distance reached by the defocused protons at the two imaging stations (IS, see Section 3.1) is used to estimate the maximum amplitude of the wakefields during the SM growth. Each IS provides two time-integrated images of the transverse distribution: the *core* and the *halo*. The core cameras receive the light directly from the scintillating screens, while the optical line of each halo camera has a mask blocking the light of the core. The enhanced dynamic range allows to resolve the outermost part of the charge distribution.
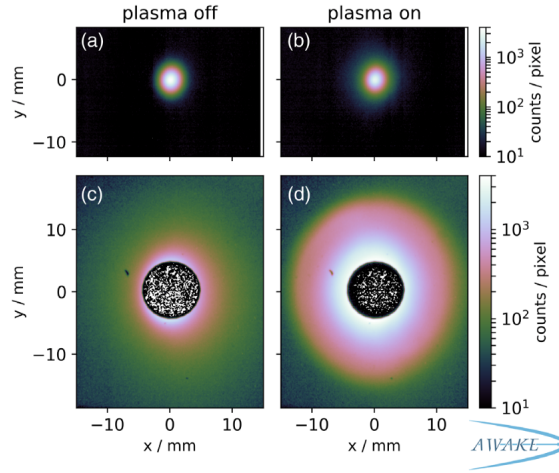

Figure 4.2: Time-integrated images of the $Q_p = 48$ nC p^+ bunch at IS 2 in Rb vapor with $n_{vap} = 7.7 \cdot 10^{14}$ cm^{-3} (a) and (c), and in plasma with $n_{pe} = 7.7 \cdot 10^{14}$ cm^{-3} (b) and (d). Panels (a) and (b) show the images from the core camera and panels (c) and (d) from the halo camera. In panels (c) and (d), the center of the proton bunch is blocked by a mask. Figure from [51].

Figure 4.2 shows core ((a) and (b)) and halo ((c) and (d)) images of the p^+ bunch at IS 2 (located ~ 10 m downstream of the plasma exit) without plasma ((a) and (c)) and with plasma ((b) and (d)). The halo images show that in the case with plasma (d) the defocused protons reach a much larger radial distance than in the case without plasma (c), demonstrating that some protons are defocused out

of the wakefields due to the self-modulation of the bunch. Combining the core and halo images, the total amount of charge is measured to be preserved at the percent level. Moreover, both the images and the corresponding transverse profiles (not shown here) are radially symmetric, indicating that the hosing instability did not take place.
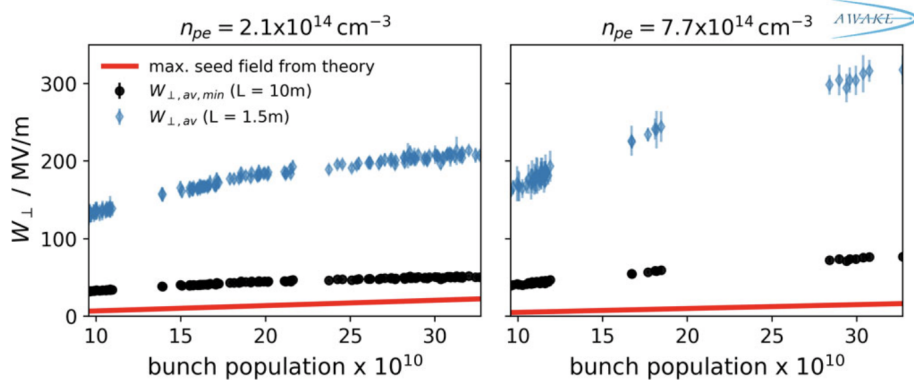

Figure 4.3: Amplitude of the transverse wakefields as a function of the p^+ bunch population for two plasma electron densities: $2.1 \cdot 10^{14}\,\mathrm{cm}^{-3}$ (left) and $7.7 \cdot 10^{14}\,\mathrm{cm}^{-3}$ (right). The red lines show the seed wakefield amplitude. The black dots are calculated assuming that the protons reaching the largest radii at IS 2 exit the wakefields after $L = 10\,\mathrm{m}$. The blue diamonds are calculated with $L = 1.5\,\mathrm{m}$ and assuming that the protons exit at $4\,\mathrm{m}$. Figure from [51].

In this experiment, the relativistic ionization front is located $0.25\,\sigma_t$ ahead of the center of the p^+ bunch, seeding SM. The maximum amplitude of the transverse wakefields is calculated using the largest radii reached by the defocused protons. Assuming the amplitude constant both along the plasma, over a distance L, and radially until the protons exit the wakefields transversely, it yields:

$$W_\perp = \frac{\theta \cdot p_{||}c}{qL}, \tag{4.1}$$

where θ is the defocusing angle that the protons must have when exiting the wakefields to reach the screen at the maximum measured radial distance.

Figure 4.3 shows the amplitude of the transverse wakefields $W_\perp$ as a function of the p^+ bunch population (left hand-side plot: $n_{pe} = 2.1 \cdot 10^{14}\,\mathrm{cm}^{-3}$, right hand-

side plot: $n_{pe} = 7.7 \cdot 10^{14} \, \text{cm}^{-3}$). The red lines show the maximum amplitude of the seed wakefields, calculated according to linear theory [17]. The amplitude of the wakefields exceeds the initial seed level both for the conservative assumption of $L = 10 \, \text{m}$ (black points in Figure 4.3) and for $L = 1.5 \, \text{m}$, that is the distance suggested by numerical simulations (blue points), reaching $\sim 300 \, \text{MV/m}$ for $n_{pe} = 7.7 \cdot 10^{14} \, \text{cm}^{-3}$ and $Q_p = 48 \, \text{nC}$. In conclusion, these results demonstrates for the first time that the amplitude of the wakefields driven by the p^+ bunch grows along the plasma due to the self-modulation.

4.3   Transition between instability and seeded self-modulation

The timing of the self-modulation is controlled by seeding the instability, i.e., by fixing the initial timing and amplitude of the wakefields. The amplitude of the seed wakefields that is needed to effectively seed the self-modulation of the p^+ bunch has been measured in the experiment presented in [52]. Seeding requires driving wakefields with amplitude larger than that of the wakefields driven by the initial imperfections (or noise [72]) in the p^+ bunch distribution. When the amplitude of the seed wakefields is smaller than the seeding threshold, SMI occurs and the timing of the wakefields varies from event to event. When seeding with the relativistic ionization front (RIF), the amplitude of the seed wakefields is determined by the local p^+ bunch charge density at the location of RIF along the bunch. The phase of the self-modulated p^+ bunch charge density distribution (i.e., of the microbunch train) is calculated on time-resolved images, aligned in time as discussed in Section 3.2.2.

Figure 4.4 shows the variation of the phase of the modulated distribution $\Delta\varphi$ over 2π as a function of the time of the RIF t_{RIF}. When $t_{RIF} > 2\,\sigma_t$ ahead of the center of the bunch (i.e., earlier along the bunch), $\Delta\varphi/2\pi$ (blue circles, left hand-side vertical axis) is larger than 20%, indicating that SM is not reproducible from event to event because seeding does not take place. When $t_{RIF} < 1.8\,\sigma_t$ ahead of the center of the bunch, SM is reproducible because seeding occurs.

The amplitude of the transverse wakefields at the ionization front location

(i.e., the amplitude of the seed wakefields, red points, right hand-side vertical axis) is calculated using linear theory (see Equation 2.5). The transition between SMI and seeded SM occurs between ~ 2.8 and $4\,\mathrm{MV/m}$.
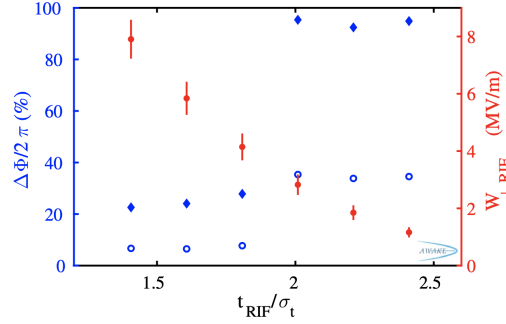

Figure 4.4: Measured rms (blue circles), full phase variation (blue diamond) and initial linear transverse wakefield amplitude (filled red circles, left hand-side vertical axis) as a function of the ionization front timing, in units of σ_t. Figure from [52].
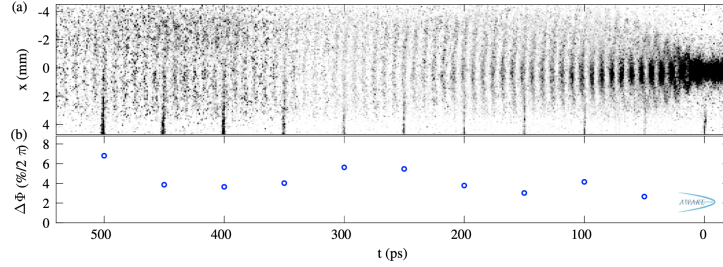

Figure 4.5: (a) Time-rsolved, "stitched" image of the self-modulated p^+ bunch with $t_{RIF} = 0.5\,\sigma_t$ and $n_{pe} = 1.81 \cdot 10^{14}\,\mathrm{cm}^{-3}$. RIF at $t = 0$ (not visible). The timing reference signal is visible every $50\,\mathrm{ps}$ at the bottom of the image. (b) Modulation rms phase variation for each set of 50-ps-long interval. Figure from [52].

Using the timing reference signal (see Section 3.2.2), it is possible to "stitch" time-resolved images one after the other to obtain a high-resolution, time-resolved image of the p^+ bunch charge density distribution over more than $500\,\mathrm{ps}$ ($> 2\,\sigma_t$), as in Figure 4.5a. Figure 4.5b shows the result of the phase analysis on $50\,\mathrm{ps}$ intervals, indicating that the value of $\Delta\varphi/2\pi$ is approximately constant and between 3% and 7% all along the bunch, indicating that the phase is reproducible and that

seeding occurred. In this experiment [52], $Q_p = 48\,\mathrm{nC}$ and $n_{pe} = 0.94 \cdot 10^{14}\,\mathrm{cm}^{-3}$.

4.4 Plasma density gradient

The theoretical studies discussing the growth of SM [55, 56] also show that the phase velocity of the wakefields is slower than that of the p^+ bunch during the growth. The resulting dephasing between the wakefields and the microbunch train has an effect on the maximum amplitude of the wakefields, that starts decreasing along the plasma, after saturation. It was suggested in simulations [59] that a positive plasma density step could reduce the dephasing and allow the amplitude of the wakefields to remain constant, at the saturation level, for a longer propagation distance.

In the experiment, it is possible to set a plasma density gradient by introducing a temperature difference between the Rb reservoirs at each end of the vapor sources. In [57], it is shown that a positive or negative plasma density gradient can diminish or enhance the dephasing, therefore increasing or decreasing the amount of charge in each microbunch, and possibly increasing or decreasing the amplitude of the wakefields at saturation. Figure 4.6 shows three time-resolved stitched images with density gradient gradient $g = +1.99/\mathrm{m}$ (a), $g = +0.03/\mathrm{m}$ (b) and $g = -1.93\%/\mathrm{m}$ (c). The timing of RIF is indicated by the red line in (b). The number and charge density of the microbunches are larger for a positive gradient than for a negative gradient. The corresponding on-axis profile below each image shows clear full modulation until $t \sim 450\,\mathrm{ps}$ in (a) and only until $t \sim 100\,\mathrm{ps}$ in (c). This indicates that the plasma density gradient has the expected effect on the self-modulation of the p^+ bunch. Moreover, the charge in each microbunch and the overall charge in the bunch core are measured to increase with a positive gradient.

The frequency of the modulation is measured with two simultaneous diagnostics: a screen producing coherent transition radiation (CTR) that is sent to a heterodyne frequency measurement, yielding the modulation frequency along the bunch [96], and the OTR-streak camera system. Figure 4.7 shows that the values of the frequency measured with the CTR (f_{CTR}, red circles) and with the OTR

(f_{streak}, blue square) are in agreement with each other and always between the expected plasma electron frequency f_{pe} at the plasma entrance and at the plasma exit, for different density gradients. With large positive or negative gradient values, two distinct frequency peaks are observed in the CTR power spectrum, as shown in the inset of Figure 4.7. This is due to the beating between the bunch modulation frequency and the local plasma frequency, that are constantly detuned by the density gradient.
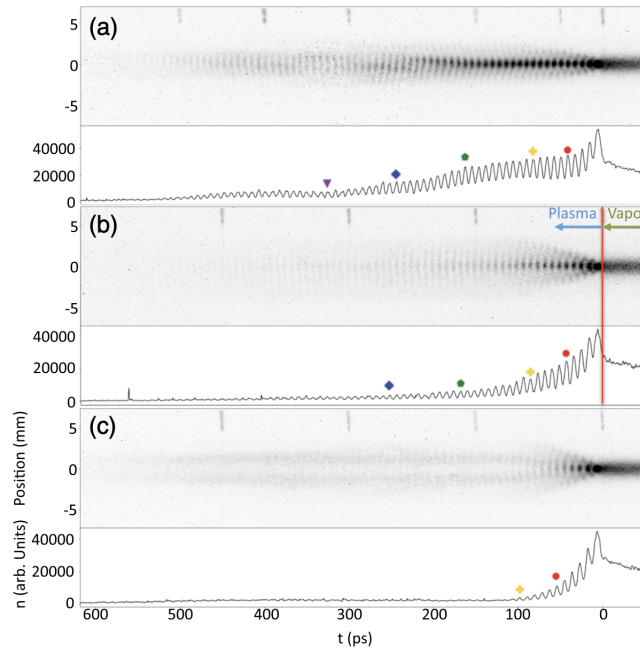

Figure 4.6: Images of the p^+ bunch transverse density distribution as a function of time for three plasma density gradient values (a) $g = +1.99\%/m$, (b) $+0.03\%/m$ (i.e. essentially constant density), and (c) $1.93\%/m$. The bunch front is on the right-hand side. Identical color scale for all images. The relativistic ionization front (not visible) is at $t = 0\,ps$ and its location marked by the red line on (b). The part of the bunch at $t > 0\,ps$ propagated in the plasma and self-modulation is clearly visible. Time profiles of the density distribution along the bunch axis are shown below each image. Color symbols indicate microbunches number 5, 10, 20, 30, and 40. Figure from [57].

In conclusion, it is shown in [57] that a plasma density gradient can compensate the stretching away of the wakefields from the seed point, occurring in a uniform

density plasma where the phase velocity of the wakefields is slower than that of the protons.
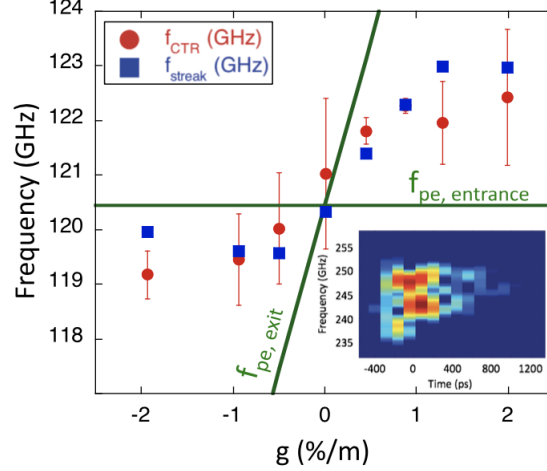

Figure 4.7: Proton bunch modulation frequency from CTR signals (f_{CTR}, red circles) and discrete Fourier transform of the streak camera profiles (f_{streak}, blue squares) versus plasma density gradient g. Green lines indicate the plasma frequencies at the plasma entrance ($f_{pe,entrance} = const$) and at the exit ($f_{pe,exit}$) calculated from the vapor density at these two locations. Inset: Spectrogram (frequency versus time) of the CTR signal recorded at the second harmonic for an event with appearance of two distinct frequency peaks obtained with $g = +1.99\%$/m. Figure from [57].

4.5   Electron acceleration

The acceleration of externally injected electrons was demonstrated in 2018 and discussed in [44]. In this experiment, the e^- bunch with $Q_e = 656\,\text{pC}$ and $E_{in} = 18.84\,\text{MeV}$ is injected in the wakefields driven by the self-modulated p^+ bunch with a vertical angle with respect to the p^+ beam trajectory. The off-axis scheme is chosen so that the electrons are captured by the wakefields after SM reaches saturation [80]. This avoids early defocusing of the electrons at the plasma entrance and increases the probability of charge capture, as the injection occurs after SM saturates and the phase velocity of the wakefields stops changing.

Figure 4.8(a) shows an image of the electrons accelerated in plasma ($n_{pe} = 1.8 \cdot 10^{14}\,\mathrm{cm}^{-3}$) at the spectrometer screen. The energy projection (Figure 4.8(b)) is well above the noise with a peak intensity at energy exceeding $700\,\mathrm{MeV}$.

The maximum amplitude that can be reached by the wakefields depends on the plasma electron density (see Equation 1.3). Also, as shown in Section 4.4, a plasma density gradient has an effect on the phase velocity of the wakefields. Indeed, Figure 4.8(c) shows that the maximum energy reached by the accelerated electrons μ_E increases when increasing n_{pe} (orange points: constant density along the plasma) and that a positive plasma density gradient (blue points) has an enhancing effect on the energy gain. A maximum energy exceeding $2\,\mathrm{GeV}$ is measured with $n_{pe} = 6.6 \cdot 10^{14}\,\mathrm{cm}^{-3}$ and $g = 0.22\%/\mathrm{m}$.
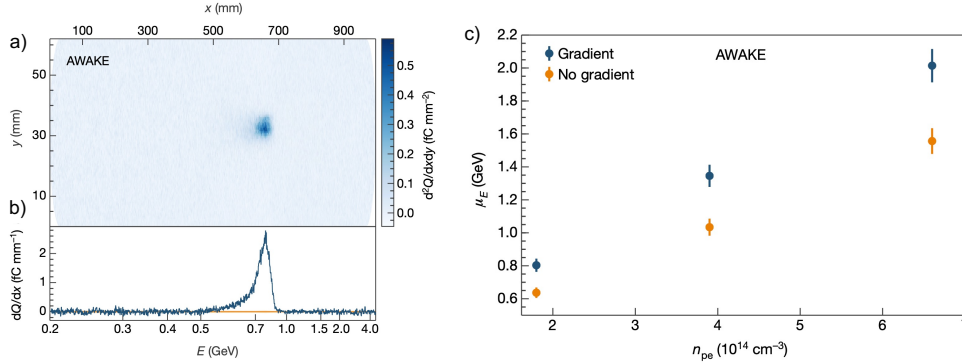

Figure 4.8: a) Image of the accelerated electrons at the spectrometer screen. b) Energy projection of the image (blue line) and $1\,\sigma$ uncertainty band (orange line). For this event, $n_{pe} = 1.8 \cdot 10^{14}\,\mathrm{cm}^{-3}$. c) Measurement of the highest peak energies μ_E achieved at different plasma densities n_{pe}, with (blue points) and without (orange points) a gradient in the plasma electron density. Figures from [44].

Chapter 5

Propagation of the electron bunch in plasma: simulation results

In the experiments discussed in this thesis, a short $\sim 18\,\text{MeV}$ e^- bunch seeds the self-modulation of a long p^+ bunch in plasma. For the seeding to be effective, the e^- bunch must drive seed wakefields with amplitude larger than the seeding threshold [52]. When the e^- bunch enters the plasma, its transverse size σ_r evolves according to:

$$\gamma m_e \frac{d^2 \sigma_r}{dt^2} = e W_\perp \tag{5.1}$$

According to linear optics [17], there is a value σ_{r0} of the transverse size at the injection in plasma for which the amplitude of the wakefields balances the divergence of the bunch and the size remains constant along the plasma. For $n_{pe} = 2 \cdot 10^{14}\,\text{cm}^{-3}$, $Q_e = 150\,\text{pC}$ and $\sigma_t = 2\,\text{ps}$, $\sigma_{r0} \sim 7\,\mu\text{m}$, that is much smaller than the minimum achievable size at the plasma entrance in the experiment ($\sigma_r > 150\,\mu\text{m}$). Therefore, in the experiment the bunch undergoes severe non-linear pinching in the first centimeters of propagation in plasma [97] due to the mismatch with the plasma focusing force, and numerical simulations are required to describe and compute the transverse bunch size and energy spectrum along the plasma.

Since the length of the plasma in the experiment L is long ($k_{pe}L > 10^4$) and the energy of the e^- bunch is small, the propagation of the bunch in plasma is a complicated process due to the slowdown of the electrons and the variation of the wakefields along the plasma.

Numerical quasi-3D simulations were performed [98] using the Fourier-Bessel-Particle-in-Cell (FBPIC) code [99]. The parameters of the simulations are similar to the experimental ones so as to study the dynamics of the process:

- $L = 10\,\mathrm{m}$, with $1\,\mathrm{cm}$-diameter exit aperture

- $n_{pe} = 2 \cdot 10^{14}\,\mathrm{cm^{-3}}$ (plasma wavelength $\lambda_{pe} = 2.4\,\mathrm{mm}$)

- plasma radius $= 1\,\mathrm{mm}$

- $Q_e = 150\,\mathrm{pC}$, $E = 18\,\mathrm{MeV}$

- $\sigma_r = 0.2\,\mathrm{mm}$ and $\sigma_t = 2\,\mathrm{ps}$ that corresponds to $\sigma_z = 0.6\,\mathrm{mm}$

- the waist of the e^- bunch is positioned at the plasma entrance

- grid size: $dz = 0.02\,k_{pe}^{-1}$ and $dr = 0.01\,k_{pe}^{-1}$

- number of azimuthal modes $= 3$ ($m = 0, 1, 2$).

The simulation results show that the transverse size of the e^- bunch pinches as soon as it enters the plasma due to its groce mismatch to the focusing force, reaching an equilibrium at $\sim 50\%$ of its initial value [74, 97, 98]. Thus, the charge density of the bunch and therefore the amplitude of the wakefields increase.

Figure 5.1 shows the longitudinal phase space of the e^- bunch (top image) and the amplitude of the transverse wakefields (bottom image) at different positions $z = ct$ along the plasma (indicated in the title of each image). The energy spectrum (red line on each phase space plot) shows that the e^- bunch immediately starts losing energy. In fact, it drives wakefields with amplitude of few MV/m (see the bottom images). Therefore, some electrons slow down and slip backwards with respect to the bunch center. As a result, for $z > 3\,\mathrm{m}$, the length of the e^- bunch is comparable to a plasma wavelength, so the amplitude of the wakefields

behind the bunch decreases and becomes ~ 0 (see the condition on the bunch duration for effective wakefields driving in Equation 2.8).
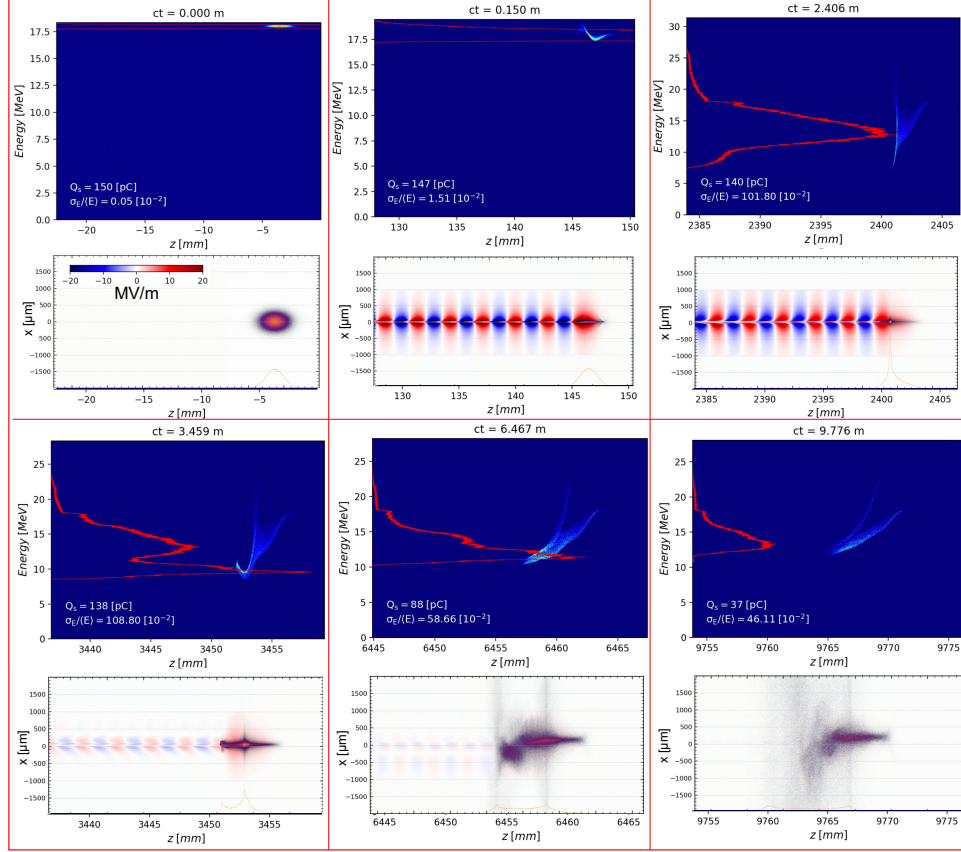

Figure 5.1: Longitudinal phase space and transverse wakefields amplitude at different location $z = ct$ along the bunch, going from left to right. The red line on each plot shows the energy spectrum.

At $z = 2.406\,\mathrm{m}$, the minimum energy is $\sim 7\,\mathrm{MeV}$. Afterwards, the minimum energy does not reach lower values, but it actually increases along the plasma (at $z = 9.776\,\mathrm{m}$, it is $> 10\,\mathrm{MeV}$). This is due to the fact that the electrons that slip backwards with respect to the center of the bunch enter the accelerating phase of the wakefields and may gain a fraction of their initial energy. In the case they lose so much energy that they dephase even further, they reach the defocusing phase of the wakefields. The bunch charge (calculated as the charge within $5\,\sigma_r$)

decreases dramatically after $z = 3.5\,\text{m}$ (bottom row). This indicates that the electrons that enter the defocusing phase are defocused out of the wakefields and of the plasma.

In the following, I further analyze the simulation results to study the evolution of the e^- bunch energy and the dynamics of the lowest-energy particles that reach the exit of the plasma.
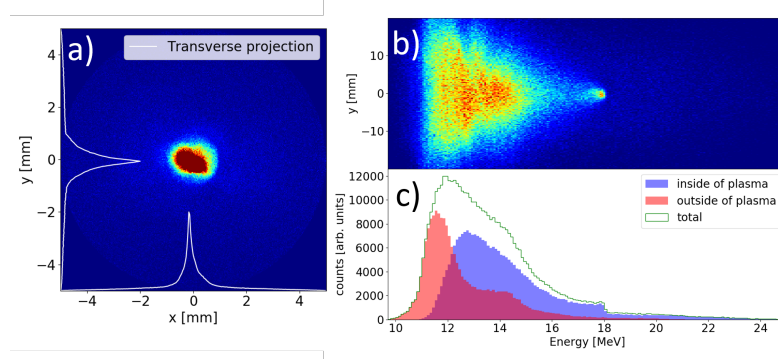

Figure 5.2: a) Transverse charge distribution of the e^- bunch at the plasma exit. The image is saturated to make visible the particles at $r > 1\,\text{mm}$. b) Energy distribution at the plasma exit. c) Green line: energy spectrum of the entire bunch obtained as the sum of the counts on the energy axis. Blue and red histograms: energy spectra of the particles that reached the exit inside and outside of the plasma, respectively.

Simulations provide the trajectory of each particle at any position along the plasma. In the analysis of the results, I only consider the particles that have radial position $r < 0.5\,\text{cm}$ at the plasma exit ($z = 10\,\text{m}$). In the experiment, these particles propagate through the exit aperture of the vapor source and reach the spectrometer screen, while the others are scattered or stopped. The transverse distribution of the bunch at the plasma exit (see Figure 5.2(a)), is made up of two populations: one composed by the electrons that travel inside the plasma for the whole propagation distance ($r < 1\,\text{mm}$ at the plasma exit) and one composed by the electrons that are defocused out of the wakefields, but with an angle that still let them reach the exit aperture ($1 < r < 5\,\text{mm}$ at the plasma exit). For each particle in the defocused population, I calculate the point along the plasma

where its trajectory crosses the propagation axis, reverting the particle velocity with respect to the propagation axis at the plasma exit. This value provides an estimate of the position along the plasma where each particle leaves the wakefields.

Figure 5.2(b) shows the simulated energy distribution of the e^- bunch after propagation in plasma. The green line in Figure 5.2(c) is the energy spectrum of the entire bunch calculated as the sum of the counts of (b) in the energy plane. The blue and red histograms show the spectra of the particles that reached the exit inside and outside the plasma, respectively. As discussed above, the lowest-energy particles are the ones that are defocused out of the wakefields before the end of the plasma.

The longitudinal phase space of the two ensembles (Figure 5.3) shows that, for the particles inside of the plasma (a), the peak of the distribution is at $\xi > -236\,\text{mm}$, while for the particles outside (b) is at $\xi < -237\,\text{mm}$. This confirms that the lowest-energy particles are defocused out of the wakefield at $z < 10\,\text{m}$ because they have slipped backwards and reached the defocusing phase.

Figure 5.3(c) shows the energy distribution of the defocused electrons as a function of the position where they cross the longitudinal axis. The first defocused particles are visible around $z \sim 2.5\,\text{m}$ (as already shown in Figure 5.1). The electrons with the lowest energy ($E \sim 10\,\text{MeV}$) are defocused out of the wakefields after $\sim 5\,\text{m}$. Then, most of them are defocused around $9\,\text{m}$ with $E \sim 12\,\text{MeV}$.
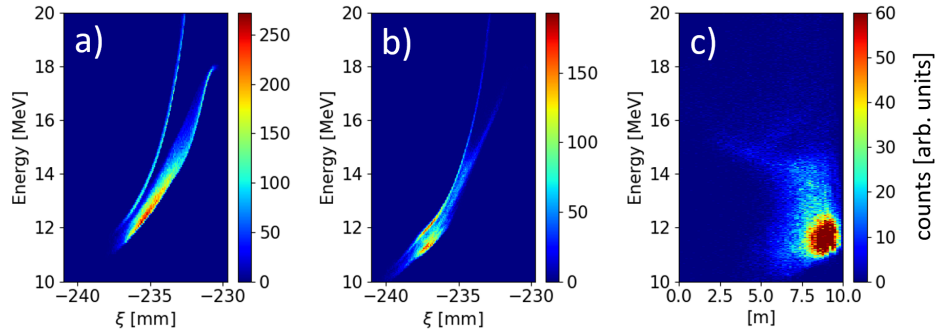

Figure 5.3: Longitudinal phase space of the particles that reach the exit inside (a) and outside (b) of the plasma exit. c) Energy distribution of the defocused electrons as a functions of the position where they leave the plasma.

Using linear wakefields theory (Equations 2.4,2.5) [17], I calculate the wakefields driven by the e^- bunch with the same parameters as in the simulations, after the transverse pinching occurs and the transverse size reaches the equilibrium. Therefore, I use $\sigma_r = 100\,\mu$m. Figure 5.4 shows the longitudinal (E_z, orange) and transverse ($W_\perp$, green) wakefields driven by the e^- bunch (longitudinal distribution shown as the blue dashed line). I calculate E_z on the propagation axis ($r = 0\,\mu$m) and $W_\perp$ at the proton bunch radius ($r = 200\,\mu$m), to compare it with the calculated value of the seeding threshold measured with ionization-front seeding [52]. The transverse wakefields are defocusing for electrons ($W_\perp > 0$) from 1.2 to 2.4 mm behind the center of the e^- bunch ($\xi = 0\,$mm). Therefore, to be defocused out of the wakefields, electrons initially at the bunch center must slip backwards by this distance with respect to the wakefields.
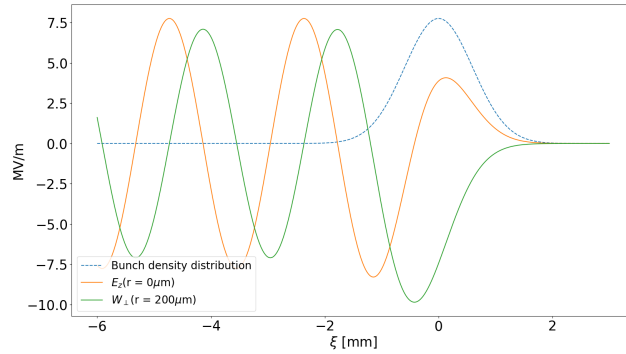

Figure 5.4: Longitudinal (E_z, green line) and transverse ($W_\perp$, orange line) wakefields driven by e^- bunch in plasma with $Q = 150\,$pC, $\sigma_t = 2\,$ps, $\sigma_r = 0.1\,$mm. $n_{pe} = 2 \cdot 10^{14}\,$cm^{-3}. The blue line show the longitudinal Gaussian distribution of the bunch. The calculations are performed following the linear wakefields theory [17].

Since E_z is accelerating for electrons ($E_z < 0$) before $W_\perp$ becomes defocusing, decelerated particles may gain some energy and their dephasing may be slowed down. Moreover, the phase velocity of the wakefields might change with the e^- bunch evolution, since it is tied to the velocity of the drive bunch.

The dephasing of a particle with velocity v_{min} with respect to one with velocity

v_{max} over a distance L_{lab} is calculated as:

$$\Delta x = \frac{L_{lab}}{v_{max}} \cdot \frac{1}{\gamma^2} \cdot \frac{v_{min} - v_{max}}{1 - \frac{v_{min} \cdot v_{max}}{c^2}} \tag{5.2}$$

The simulation results (see Figure 5.1) show that the energy loss occurs in the first $\sim 2\,\mathrm{m}$ of propagation. I therefore calculate the dephasing experienced by the particles after this point. For example, the dephasing distance of the particles that are defocused at $z = 9\,\mathrm{m}$ with $E = 12\,\mathrm{MeV}$ is $\Delta x = 2.8\,\mathrm{mm}$, and for those that are defocused at $z = 6.5\,\mathrm{m}$ with $E = 10\,\mathrm{MeV}$ is $\Delta x = 1.7\,\mathrm{mm}$. These values are within or very close to the ones mentioned above for the location of the defocusing phase of the wakefields behind the center of the bunch. The discrepancy may be due to the fact that the phase velocity of the wakefields is actually slower than the initial velocity of the bunch due to the slowdown of the electrons, and that particles recover some of the lost energy, when passing through the accelerating phase of the wave. Therefore, the dephasing time may increase.
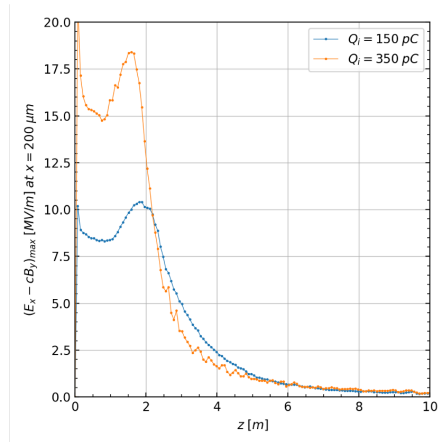

Figure 5.5: Simulated maximum amplitude of the transverse wakefields behind the bunch along the plasma for $Q_e = 150\,\mathrm{pC}$ (blue line) and $Q_e = 350\,\mathrm{pC}$ (orange line).

Figure 5.5 shows the simulated maximum amplitude of the transverse wakefields behind the e^- bunch, along the plasma for $Q_e = 150\,\mathrm{pC}$ (blue line) and $350\,\mathrm{pC}$ (orange line). When increasing the charge of the e^- bunch (while keeping the other parameters of the bunch constant), the transverse wakefields behind the bunch reach larger amplitude in the first meters of propagation. Indeed, the initial

charge density of the bunch determines the amplitude reached by the wakefields in the plasma.

In conclusion, simulation results show that the lowest-energy particles are the ones that experience the highest decelerating wakefields during the first ~ 2 meters of propagation in plasma. Then, due to dephasing, the bunch becomes longer and the amplitude of the wakefields behind the bunch decreases. The slowest particles slip backwards into the accelerating and then defocusing phase of the wakefields and are defocused out of the wakefields and of the plasma. If the divergence angles are small enough, these particles pass through the exit aperture and can be detected on the spectrometer screen, as discussed in Section 3.2.1. These are the electrons that carry the most important information on the amplitude of the wakefields in the first meters of propagation, where we expect the seeding of the self-modulation of the p^+ bunch to occur. In particular, their energy is a probe of the amplitude of the seed transverse wakefields.

Chapter 6

Experimental results

In this Chapter, I present the main experimental results of this work. I discuss the measurements on the deceleration of the e^- bunch in plasma (Section 6.1) and on the effect of the adiabatic response of the plasma on the p^+ bunch (Section 6.2). I demonstrate that the e^- bunch seeds the self-modulation of a long, relativistic p^+ bunch in plasma (Section 6.3). I also show that, when seeding with an e^- bunch, it is possible to control the growth of SM. When varying the charge of the seed e^- bunch, the amplitude of the seed wakefields varies (Section 6.4), while leaving the growth rate of SM unchanged. Analogously, when varying the charge of the p^+ bunch, the growth rate varies (Section 6.5). I show that the hosing instability of the p^+ bunch can be seeded by purposely misaligning the trajectory of the seed e^- beam trajectory with respect to that of the p^+ beam (Section 6.6). Finally, I present three-dimensional imaging of the self-modulated p^+ bunch (Section 6.7).

6.1   Electron deceleration in plasma

I measure the maximum energy lost by the e^- bunch in plasma using the magnetic spectrometer. The goal of the measurement is to estimate, with the help of numerical simulations, whether the amplitude of the wakefields driven by the e^- bunch in the first meters of propagation in plasma is sufficient to seed the

self-modulation of the long p^+ bunch.

Figure 6.1 shows a single-event image of the the e^- bunch on the spectrometer screen after propagation in vacuum (a) and propagation in plasma (b). The initial bunch charge measured in the transfer line is $Q_e = (161 \pm 20)\,\mathrm{pC}$ and the transverse size is measured at the waist $\sigma_r = (0.20 \pm 0.04)\,\mathrm{mm}$ during the setup. The blue projection line below each image shows the corresponding energy spectrum. In the case without plasma, the energy spectrum is centered around the initial energy $E_{in} = 18.3\,\mathrm{MeV}$. In the case with plasma, the spectrum extends to lower energies because the e^- bunch loses energy, driving wakefields along the plasma. The maximum energy loss is $\Delta E = E_{in} - E_{min} = 6.8\,\mathrm{MeV}$, where E_{min} is the minimum energy reached by the spectrum in the case with plasma. This is calculated as the energy where the distribution reaches 10% of its maximum value (orange point in (b), see Section 3.2.1).
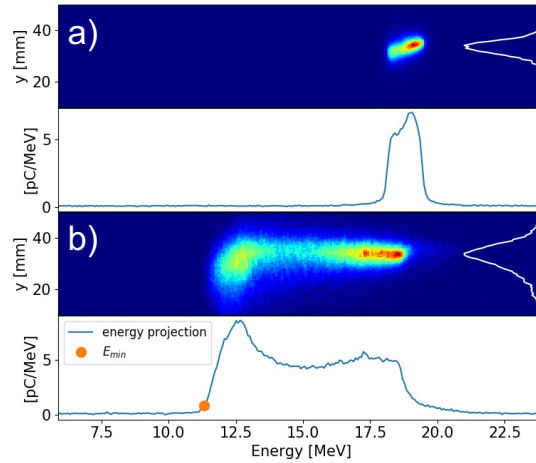

Figure 6.1: Single-event spectrometer image of the $Q_e = 161\,\mathrm{pC}$ e^- bunch after propagation in vacuum (a) and in plasma (b). The blue line below each image shows the corresponding energy spectrum obtained as a sum of the counts in the energy plane. The white lines on each image show the projection on the vertical plane.

In case of propagation without plasma (a), the transverse distribution (white line) at the screen is a shadow of the exit aperture of the vapor source, since the transverse size of the beam is larger than the aperture and the beam diverges

from the entrance of the vapor source. In case of propagation in plasma (b), the electrons that reach the spectrometer travel for some distance in plasma (see Chapter 5) and therefore may leave the vapor source with a divergence angle larger than in the case with no plasma. As a consequence, the transverse distribution at the screen is larger than in the case without plasma.
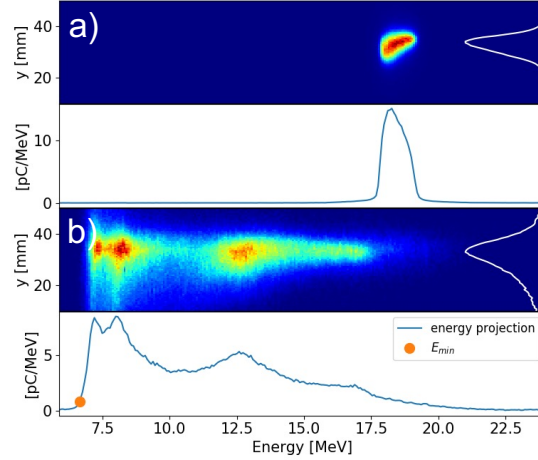

Figure 6.2: Single-event spectrometer image of the $Q_e = 461\,\mathrm{pC}\ e^-$ bunch after propagation in vacuum (a) and in plasma (b). The blue line below each image shows the corresponding energy spectrum obtained as a sum of the counts in the energy plane. The white lines on each image show the projection on the vertical plane.

When increasing the charge to $Q_e = (461 \pm 22)\,\mathrm{pC}$ ($\sigma_r = (0.30 \pm 0.05)\,\mathrm{mm}$) as in Figure 6.2, the energy spectrum reaches lower values after propagation in plasma (b). The value of the maximum energy loss increases to $\Delta E = 11.3\,\mathrm{MeV}$. As discussed in Chapter 5, numerical simulations show that the energy loss mostly occurs in the first $\sim 2\,\mathrm{m}$ of propagation, where it drives the wakefields with largest amplitude. Moreover, a larger initial charge density of the bunch leads to larger amplitude of the wakefields in the first meters of propagation in plasma and to a larger amount of energy lost by the electrons. Thus, larger energy loss corresponds to larger amplitude of the wakefields in the first meters of propagation.

Simulations also show that the electrons that slip backwards due to energy loss may gain energy when entering the accelerating phase of the wakefields. The

complex evolution of the energy spectrum along the bunch and along the plasma is the likely cause for the multi-peaked distribution of Figure 6.2(b).

Theoretical and simulation studies show that the transverse size σ_r of the e^- bunch becomes smaller as soon as it enters the plasma, because of its mismatch with the plasma focusing force. The transverse size reaches an equilibrium at $\sim 0.5\,\sigma_r$ [97]. Varying σ_r, we therefore vary the size and ultimately the charge density at the equilibrium. In the experiment, we can tune the optics of the transfer line so as to increase σ_r, while keeping Q_e and the other parameters of the bunch constant. Figure 6.3(a) shows a waterfall plot of 305 events of the e^- bunch with $Q_e = 161\,\mathrm{pC}$ while varying σ_r. The maximum energy loss is $\Delta E = (6.8 \pm 0.2)\,\mathrm{MeV}$ when $\sigma_r = 0.2\,\mathrm{mm}$ (from event 213 to 305, blue projection line). The uncertainty is calculated as the standard deviation of ΔE in the dataset. The maximum energy loss becomes smaller when $\sigma_r = 0.3\,\mathrm{mm}$ ($\Delta E = (6.3 \pm 0.4)\,\mathrm{MeV}$, from event 110 to 212, orange projection line), and decreases even more when $\sigma_r = 1.3\,\mathrm{mm}$ ($\Delta E = (2.5 \pm 0.3)\,\mathrm{MeV}$, from event 1 to 109, green projection line).

Figure 6.3(b) shows the same measurement with $Q_e = 461\,\mathrm{pC}$. $\Delta E = (11.4 \pm 0.2)\,\mathrm{MeV}$ when $\sigma_r = 0.3\,\mathrm{mm}$ (from event 108 to 228, blue projection line) and $\Delta E = (7.7 \pm 0.3)\,\mathrm{MeV}$ when $\sigma_r = 1.3\,\mathrm{mm}$ (from event 1 to 107, orange projection line). The same trend as in the previous case is visible, while the energy loss is overall larger, as the bunch charge is higher.
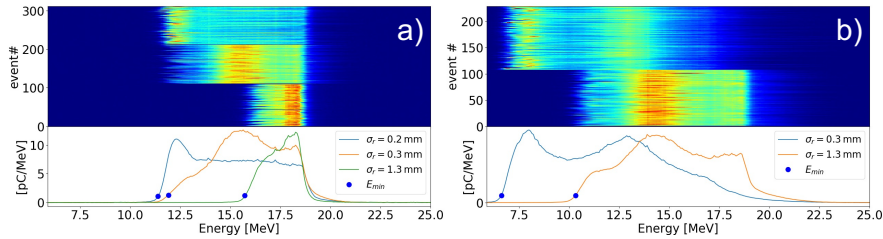

Figure 6.3: Waterfall plots of spectrometer images of the $Q_e = 161\,\mathrm{pC}$ (a) and $Q_e = 461\,\mathrm{pC}$ (b) e^- bunch. a) From event 1 to 107, $\sigma_r = 1.3\,\mathrm{mm}$ (green energy projection), from event 108 to 228, $\sigma_r = 0.3\,\mathrm{mm}$ (orange energy projection), from event 213 to 305, $\sigma_r = 0.2\,\mathrm{mm}$ (blue energy projection).b) From event 1 to 105, $\sigma_r = 0.1.3\,\mathrm{mm}$ (orange energy projection), from event 108 to 185, $\sigma_r = 0.3\,\mathrm{mm}$ (blue energy projection).

To summarize, the maximum energy loss decreases when increasing σ_r because the amplitude of the wakefields driven by the bunch decreases. Moreover, the entire distribution becomes skewed towards higher energies. When increasing the bunch charge, keeping σ_r constant, the maximum energy loss increases.

Since the e^- bunch duration $\sigma_t \sim 6\,\mathrm{ps}$ is close to the plasma electron period $T_{pe} = 7.9\,\mathrm{ps}$, a part of the bunch is in the accelerating phase of the wakefields (see Figure 5.4). Therefore, some electrons are accelerated and may reach the end of the plasma with energy higher than the initial one (see for example the first 150 events in Figure 6.3(b)). The energy spectra show more overall accelerated electrons when σ_r is larger, because the effect of the energy loss is smaller.

In the following Sections, I will discuss the measurements on the e^- bunch seeding of SM in plasma. In that experiment, $n_{pe} = 0.97 \cdot 10^{14}\,\mathrm{cm}^{-3}$. To better understand the results, I measured the energy loss of the e^- bunches with the same parameters as those used to study the seeding of SM (see Table 3.2). As the electron spectrometer is located downstream of the OTR foil, the measurements on the p^+ bunch and on the e^- bunch are not simultaneous (the laser beam dump and the OTR screen block the e^- bunch).

Figure 6.4 shows the energy spectrum of the e^- bunch with $Q_e = 147\,\mathrm{pC}$ (blue line), $249\,\mathrm{pC}$ (orange line), $777\,\mathrm{pC}$ (green line), after propagation in plasma. The red dashed line indicates the initial energy E_{in}. Also in this case, the energy spectrum reaches lower values when increasing the charge of the e^- bunch. In fact, the measured values of the energy loss are $\Delta E = (5.6 \pm 0.6), (8.9 \pm 0.1), (11.8 \pm 0.3)\,\mathrm{MeV}$, respectively. When increasing Q_e, all the other parameters of the e^- bunch increase as well. However, also the initial bunch density increases. Numerical simulations show that this results in a larger amplitude of the wakefields in the first meters of propagation.

For the e^- bunch to seed effectively SM of the p^+ bunch in plasma, the transverse wakefields behind the e^- bunch must have amplitude larger than the seeding threshold. Previous experiments (with the ionization-front seeding) measured the seeding threshold to be in the range between $(2.8 - 4.0)\,\mathrm{MV/m}$ [52], for $n_{pe} = 0.94 \cdot 10^{14}\,\mathrm{cm}^{-3}$ and p^+ bunch charge $Q_p = 48\,\mathrm{nC}$. In the following, I attempt to estimate the amplitude of the transverse wakefields behind the e^-
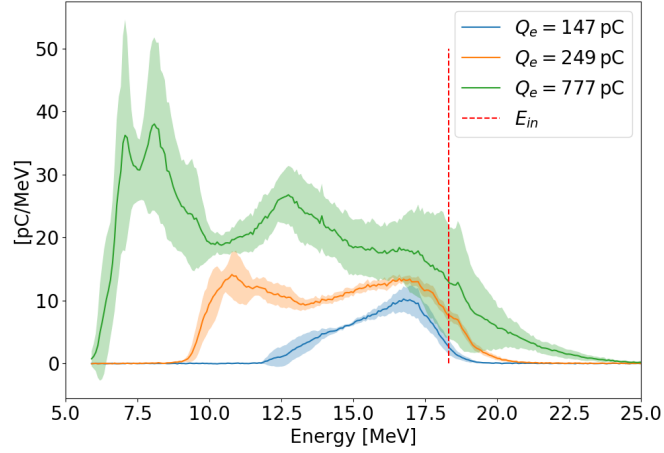
bunch at $r = 200\,\mu\text{m}$ (p^+ bunch radius).

Figure 6.4: Energy spectrum obtained from the energy projection of averaged spectrometer images of the $Q_e = 147\,\text{pC}$ (blue line), $249\,\text{pC}$ (orange line), $777\,\text{pC}$ (green line) e^- bunch after propagation in plasma. The vertical axis is converted into charge for every energy bin. The band around each spectrum indicates the uncertainty calculated as the standard deviation of each dataset. The red dashed line indicates the initial energy E_{in}.

The maximum amplitude of the decelerating wakefields within the bunch (causing the energy loss) and the maximum amplitude of the accelerating wakefields behind the bunch are related by the transformer ratio T:

$$T = \frac{|E_z|_{max,behind}}{|E_z|_{max,within}}. \tag{6.1}$$

For a single Gaussian bunch in the linear regime of PWFA, the maximum value of the transformer ratio is $T = 2$ [100].

The energy loss is the result of the propagation along the $10\,\text{m}$ of plasma, and it depends on the longitudinal wakefields E_z as $\Delta E = q \int_0^{10\,m} E_z(z)\,dz$. If I consider the electrons to lose energy uniformly along the entire distance, for the smallest e^- bunch charge ($Q_e = 147\,\text{pC}$, $\Delta E = 5.6\,\text{MeV}$) $E_z = 0.56\,\text{MV/m}$. In this case, for $T = 2$, the associated transverse wakefields behind the bunch $W_\perp(r = 200\,\mu\text{m}) = E_z(r = 0)\frac{dR(r=200\,\mu\text{m})/dr}{k_{pe}R(r=0)} \sim 1.6\,\text{MV/m}$ (Equation 2.7, where R is the geometrical factor calculated as in [17]). The amplitude of the transverse

wakefields would be smaller than the seeding threshold and the e^- bunch may not seed the SM of the p^+ bunch. Considering the deceleration to mainly occur in the first $2\,\mathrm{m}$ (as suggested by the simulation results), $E_z \sim 3\,\mathrm{MV/m}$, and the associated $W_\perp$ is larger than the seeding threshold even in the case of $T < 2$ (e.g., for $T = 1$, $W_\perp \sim 8\,\mathrm{MV/m}$). For the larger values of Q_e, the energy loss and therefore the amplitude of the wakefields is larger, always exceeding the seeding threshold.

In Section 6.3 I will show that the e^- bunch seeds SM of the p^+ bunch and that, therefore, it drives wakefields with amplitude exceeding the seeding threshold, at least over the first meters of propagation in plasma. Moreover, in Section 6.4 I will discuss the effect of the variation of the seed e^- bunch charge on the SM growth, demonstrating that larger energy loss corresponds to larger growth of SM due to larger seed wakefields amplitude.

6.2   Adiabatic focusing of the proton bunch in plasma

When a charged bunch travels in plasma, the free plasma electrons migrate so as to neutralize the space-charge field of the bunch [16], and the bunch is therefore focused by the azimuthal magnetic field generated by its own current, that is not balanced by the radial electric field [101, 102, 103]. When this effect occurs over successive equilibrium states, it does not set an oscillation of the plasma electrons and it is known as the *adiabatic* response of the plasma. When the duration of the bunch σ_t is much longer than the plasma electron period T_{pe}, the bunch also undergoes the self-modulation instability [50, 51]. Thus, the amplitude of the wakefields grows along the bunch and along the plasma, and the effect of the self-modulation can become dominant over the adiabatic focusing effect.

In order to study the plasma adiabatic focusing, we minimize the effect of SM by lowering the plasma electron density with respect to the value normally used in the experiment ($\mathcal{O}(10^{14}\,\mathrm{cm^{-3}})$). As the plasma radius is approximately five times larger than the initial transverse radius of the bunch, the plasma electron density n_{pe} must be $> n_p/25 \sim 8 \cdot 10^{10}\,\mathrm{cm^{-3}}$ for the plasma to supply enough electrons to effectively cancel the space-charge field of the bunch. For this value of

74

n_{pe}, $T_{pe} = 394\,\mathrm{ps}$, that is longer than the p^+ bunch duration σ_t. Thus, SMI does not occur. In the experiment, we obtain a low density by generating the plasma without opening the valves connecting the vapor source to the reservoirs where the rubidium is contained. The laser pulse ionizes the residual vapor in the source creating plasma with n_{pe} smaller than the one used in the normal operation. The value of the residual Rb vapor density is unknown because the density diagnostics cannot measure $n_{vap} < 0.5 \cdot 10^{14}\,\mathrm{cm}^{-3}$.
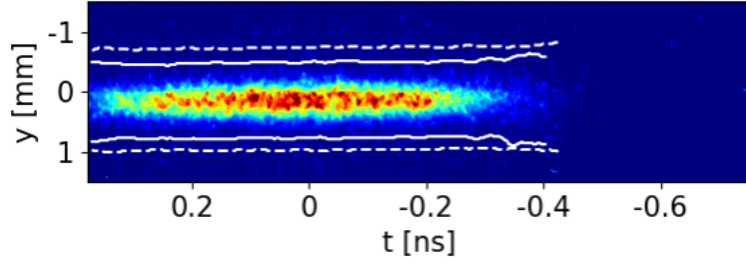

Figure 6.5: 1.1 ns-scale, averaged, time-resolved image of the p^+ bunch with $Q_p = 14.7\,\mathrm{nC}$ after propagation in plasma with residual density. The white continuous lines show the transverse contours of the distribution along the bunch. The white dashes lines are the transverse contours for the bunch with equal Q_p in case of no plasma.

Figure 6.5 shows a 1.1 ns-scale averaged time-resolved image of the the p^+ bunch after traveling in plasma with residual density. The white continuous lines show the transverse contours of the distribution, calculated as discussed in Section 3.2.3. The white dashed lines show the transverse contours of the corresponding case without plasma, representing that of the incoming bunch. Indeed, the transverse extent is smaller than the one of the incoming bunch because of the plasma adiabatic focusing effect. Since SM is not visible, $T_{pe} \gtrsim \sigma_t = (261 \pm 23)\,\mathrm{ps}$, that corresponds to $n_{pe} \lesssim 1.83 \cdot 10^{11}\,\mathrm{cm}^{-3}$.

Moreover, there is no visible oscillation of the contours along the bunch. This suggests that the entire bunch keeps converging for the entire propagation in plasma. Therefore, the period of oscillation of the transverse size (betatron oscillation) must be longer than four times the plasma length. Indeed, one can calculate the wavelength of the betatron oscillation $\lambda_\beta(t)$ as:

$$\lambda_\beta(t) = 2\pi/K_\beta(t), \tag{6.2}$$

where $K_\beta(t) = \sqrt{\frac{n_p(t)q^2(1-e^{-1/2})}{\gamma m_p c^2 \varepsilon_0}}$ is the strength of the self-focusing force along the bunch, resulting from the magnetic fields of the bunch evaluated at $r = \sigma_r$.
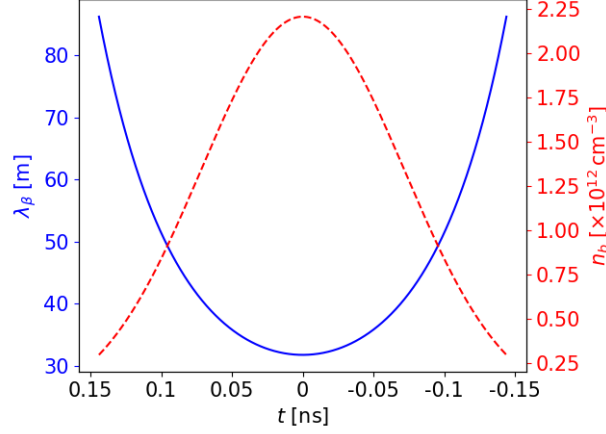

Figure 6.6: Wavelength λ_β of the betatron oscillation due to the self-focusing force (blue line, left hand-side vertical axis) and longitudinal charge density distribution (red dashed line, right hand-side vertical axis) along the p^+ bunch with $Q_p = 14.7\,\text{nC}$, corresponding to $n_p = 6.9 \cdot 10^{12}\,\text{cm}^{-3}$. The value of λ_β is calculated analytically with parameters equal to the experimental ones.

When $\lambda_\beta/4 > L$ ($L = 10\,\text{m}$ is the length of the plasma), the beam envelope stays in a converging phase for the entire propagation distance. Figure 6.6 shows that $\lambda_\beta/4 > L$ along most of the bunch. For $|t| < 0.07\,\text{ns}$, $\lambda_\beta < 40\,\text{m}$, so one may expect the beam transverse size to oscillate and therefore to increase around the center of the bunch, even though this is not visible in Figure 6.5.

Figure 6.7 shows the transverse extent w along the p^+ bunch, for different values of Q_p, with residual plasma density. Since the initial transverse size of the bunch varies when varying Q_p (see Table 3.1), I normalize w with respect to the transverse extent w_{off}, measured in the cases without plasma. The bunch is focused stronger for larger Q_p (i.e., larger n_p, see Table 3.1) because the amplitude of the magnetic field generated by the bunch increases. For all cases with $Q_p \geqslant 22.4\,\text{nC}$, the envelope reaches a minimum value around $\pm 1.5\,\sigma_t$ (i.e., ahead and behind the center of the bunch) and it slightly increases at the bunch center. This suggests that $\lambda_\beta/4 > L$ at the bunch center, and therefore this part of the

bunch is over-focused, towards the end of the plasma (see Equation 6.2).

In Sections 6.4 and 6.5 I will show that the adiabatic focusing effect is present also when n_{pe} is larger and the p^+ bunch self-modulates. I will show that the transverse extent at the front of the bunch (where the growth of the SM is small), always follows the same evolution for equal Q_p, and that, when seeding SM with a preceding e^- bunch, the transition between the effect of the adiabatic response and that of the self-modulation depends on the amplitude of the seed wakefields. The adiabatic focusing is a process substantially different from the wakefields because the self-focusing force acting on each longitudinal slice of the bunch depends on the local value of $n_p(t)$ and not on the convoluted effect of the preceding part of the bunch.
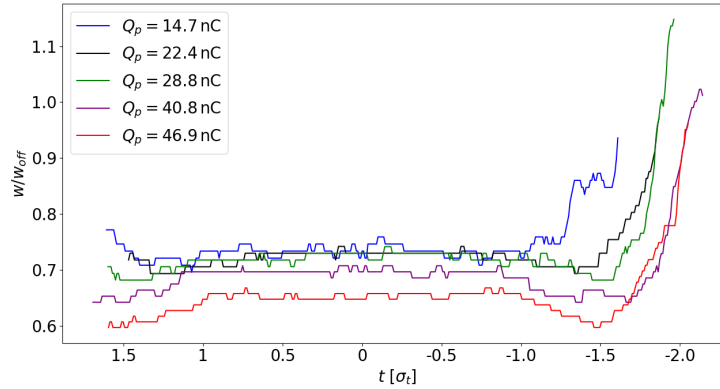

Figure 6.7: Transverse extent w along the bunch normalized with respect to the value of the case without plasma w_{off}, for different values of Q_p. The horizontal axis is in units of the bunch duration σ_t. Bunch center at $t = 0$.

6.3 Timing reproducibility of the self-modulation seeded by the electron bunch

The self-modulation instability (SMI) is a self-consistent process, where the wakefields driven in plasma by a long, narrow, relativistic, charged particle bunch act back on the bunch itself, modulating its transverse distribution along the

bunch. The modulated distribution drives enhanced wakefields, initiating a feedback loop that converts the bunch into a train of microbunches. Hence, the timing of the microbunch train along the bunch is tied to that of the transverse wakefields: the microbunches develop in their focusing phase. When a long ($\sigma_t \sim 240\,\text{ps}$) p^+ bunch enters a pre-ionized plasma, it undergoes the self-modulation instability. When not seeded, SMI develops from the noise [72] or from the imperfections [52] in the p^+ bunch charge distribution. Thus, it is not reproducible neither in amplitude nor in timing from event to event [52]. When a seed wakefield is applied, SM grows from the initial modulation of the radius along the bunch caused by the seed wakefields: the timing and initial amplitude of SM is defined by the seed wakefields.

In the experiment described here, the relativistic ionization front (RIF) is located $t_p \sim 2.5\,\sigma_t$ ahead of the center of the p^+ bunch. At this location, the charge density of the p^+ bunch is too small to drive wakefields with amplitude large enough to seed SM [52]. Thus, RIF ionizes the vapor but the onset of the beam-plasma interaction does not seed SM. We seed SM using a preceding e^- bunch with $Q_e = 249\,\text{pC}$, traveling $t_{seed} = 580\,\text{ps}$ ahead of the center of the p^+ bunch.

As discussed in Section 3.2.2, we use 73 ps-scale time-resolved images, aligned in time using the timing reference signal [90], to determine the timing reproducibility of SM. Figure 6.8(a) shows eight consecutive single-event images of the p^+ bunch in plasma between 294 and 347 ps ahead of the center of the bunch, when no seed wakefield is applied (i.e., the e^- bunch is not present). Each microbunch occurs at a different time t along the bunch on each image, indicating that the timing of SM is not reproducible: the self-modulation occurs as an instability (SMI).

When the e^- bunch is present (Figure 6.8(b), all other parameters are kept constant) each microbunch appears at the same t along the bunch on each image: SM is reproducible because the instability is seeded by the wakefields driven by the e^- bunch. For example, the first microbunch always appears at $t \sim -343\,\text{ps}$ and the third at $t \sim -321\,\text{ps}$.

In the SMI case, the full modulation occurs at different times along the bunch,
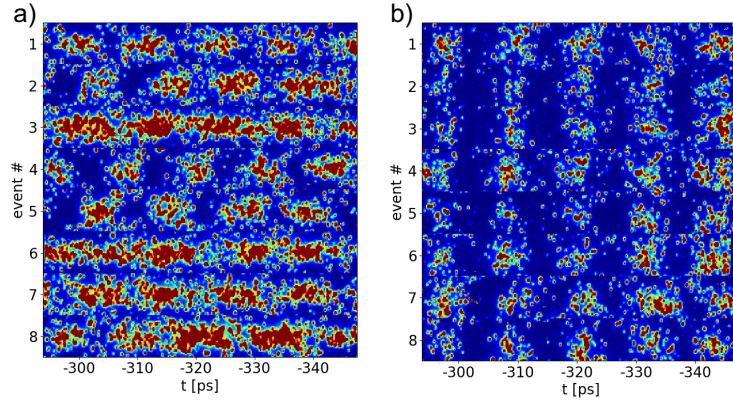
Figure 6.8: Waterfall plots of $73\,$ps-scale, single-event, time-resolved images of p^+ bunch with $Q_p = 40.8\,$nC in plasma with no seed e^- bunch (a) and with the seed e^- bunch ($Q_e = 249\,$pC, b). Each event shows a limited portion of the image between $y = \pm 0.5\,$mm around the propagation axis. Identical color scale. The p^+ bunch travels from left to right with center at $t = 0\,$ps.

suggesting that also the amplitude of the wakefields varies from event to event (see for example events #3 and #4 in Figure 6.8(a)), whereas in the seeded case the bunch modulation is already fully developed for all events. This indicates that, at the same location along the bunch, the wakefields reach larger amplitudes in the seeded case than in SMI, and therefore form the microbunches earlier along the bunch. This is due to the fact that the wakefields grow from the seed level ($\sim$MV/m) when seeding occurs and from the uncontrolled and lower-amplitude initial wakefields driven by the p^+ bunch otherwise.

The average of many periodic signals with the same frequency and timing shows the same characteristics of the original signals. Similarly, the average of the single-event images from Figure 6.8(b) is representative of the dataset, as shown in Figure 6.9(b), because the distribution is reproducible from event to event. Instead, no consistent pattern is visible when the individual signals have different timing with respect to each other as in Figure 6.9(a), that is the average of the events from Figure 6.8(a). Also the defocused protons are clearly visible in Figure 6.8(b). The distance from the propagation axis that they reach transversely increases along the bunch because the amplitude of the wakefields grows.
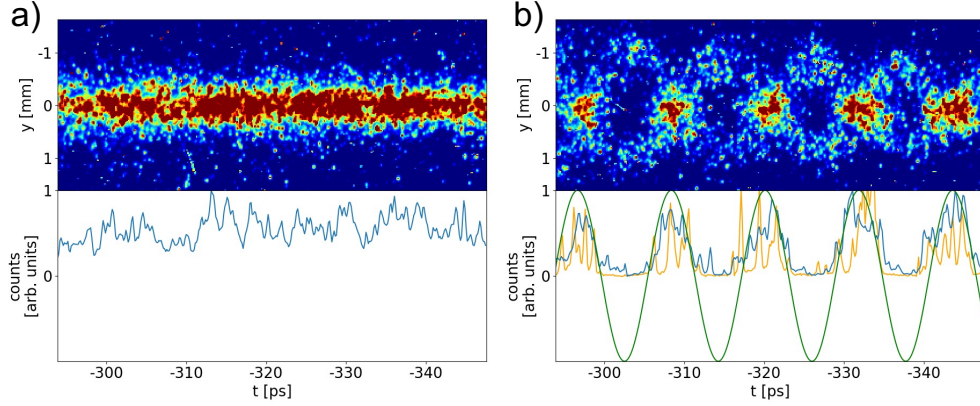
Figure 6.9: Averaged, 73 ps-scale, time-resolved images from Figure 6.8: a) no seed bunch, b) with seed bunch ($Q_e = 249$ pC). Below each image: on-axis profile (blue line), calculated as the sum of the counts in the transverse direction between $y = \pm 0.2$ mm. In (b): on-axis profile of a single image and the cosine function with frequency $f_{mod} = 85.13$ GHz and phase $\varphi = -1.83$ calculated from the DFT on the profile (green line).

Below each image, I plot the corresponding on-axis profile (blue line). In the SMI case (a) the profile shows no modulation, while in the seeded case (b) the profile shows full modulation with enhanced signal-to-noise ratio with respect to the one of a single-event image (orange line).

The time resolution of a streak camera is the highest when the signal is scattered as in the images in Figure 6.8. In fact, when the intensity of the light is too high, the space-charge effects inside of the streak tube cause the signal to broaden, limiting the time resolution. As a consequence, though, the profiles are noisy and it is difficult to determine the timing of each microbunch. Therefore, I determine the timing of the microbunch train using a discrete Fourier transform (DFT) method (as described in the Supplemental Material of [52]).

I calculate the power spectrum obtained from the DFT on the on-axis profile of the time-resolved images (calculated by summing the counts in the transverse direction between $y = \pm 0.2$ mm). The power spectrum of a 73 ps-scale time-resolved image has a bin size $\Delta f = \frac{1}{73\,\mathrm{ps}} = 13.7$ GHz. To increase the frequency resolution, I reduce the bin size by padding the time profile with an array of $P \times 512$ zero amplitudes, so $\Delta f = 13.7$ GHz$/P$. This is equivalent to including the effect

of the finite time window of the streak camera on a longer signal. The frequency of the modulation f_{mod} is obtained as the peak of the spectrum in the frequency range ± 20 GHz around the value expected from the measured Rb vapor density ($f_{pe} = 88.3$ GHz for $n_{pe} = 0.97 \cdot 10^{14}$ cm^{-3}). Figure 6.10(a) shows that the value of f_{mod}, obtained from the DFT on Figure 6.9(b), converges to 85.03 GHz (red dashed line) for $P \gtrsim 50$. For $P = 50$, $\Delta f = 0.27$ GHz, that is comparable with the uncertainty on the Rb vapor density (0.5%) and on the corresponding plasma frequency ($\propto n_{pe}^{1/2} < 0.7\%$). Figure 6.10(b) shows the frequency power spectrum with no zero padding (red dots) and with $P = 50$ (blue line). In the following, $P = 50$ is always used. For the distribution in Figure 6.9(b), $f_{mod} = 85.13$ GHz, that is smaller than the expected f_{pe} by a factor larger than the uncertainty on the plasma electron density. This discrepancy may be due to the growth of SM, that causes a slowdown of the wakefields phase velocity with respect to the p^+ bunch, and therefore a decrease in frequency of the modulation [55, 74].

I calculate the phase at f_{mod} as $\varphi = atan2(\text{Im}(\tilde{F}(f_{mod})), \text{Re}(\tilde{F}(f_{mod})))$, where $\tilde{F}(f_{mod})$ is the Fourier transform of the signal, evaluated at f_{mod}. This is then converted into time along the observation window as $t = T_{pe}\frac{\varphi}{2\pi}$, where $T_{pe} = f_{pe}^{-1} = 11.15$ ps is the plasma electron period. According to Fourier theorem, the original signal in the time domain $g(t)$ can be described by the sum of sinusoidal functions that in the exponential formulation yields:

$$g(t) = \sum_{n=0}^{N-1} c_n e^{i\frac{2\pi n t}{T}}, \tag{6.3}$$

where c_n is the Fourier coefficient, N is the number of bins and T is the period of the signal. Since the wakefields are sinusoidal with one main frequency component equal to f_{pe} [17], I plot in Figure 6.9(b) (green line) the cosine function (the real part of Equation 6.3) with the largest coefficient c_n, i.e. with frequency equal to f_{mod} and with the corresponding φ. Indeed, the microbunches are contained within half period of the cosine function, that we infer corresponds to the focusing phase of the wakefields.

In order to calculate the timing variation between different events, I perform the DFT on the on-axis distribution of the single-event images. Choosing f_{mod} as the peak of the power spectrum of each image, I obtain an rms variation of

1.14 GHz. This is much larger than the one expected from the variation of the Rb vapor density (0.2%) and it is in contradiction with the observation of timing reproduciblity in Figure 6.8(b). In fact, a random variation of the frequency of ± 1.14 GHz at the seed bunch location would correspond to a timing variation $\Delta t = 26.1$ ps at the measurement window (~ 330 ps $\sim 10\, T_{pe}$ behind the seed bunch), that is much larger than what is observed. This large variation of the measured modulation frequency is due to the small number of microbunches in the measurement window and to the large amount of noise in the single-event images. Thus, for the timing reproduciblity analysis I calculate for all events the phase value corresponding to the same frequency bin. I choose the latter as the one corresponding to the peak of the power spectrum f_{mod} calculated on the averaged image of all events.
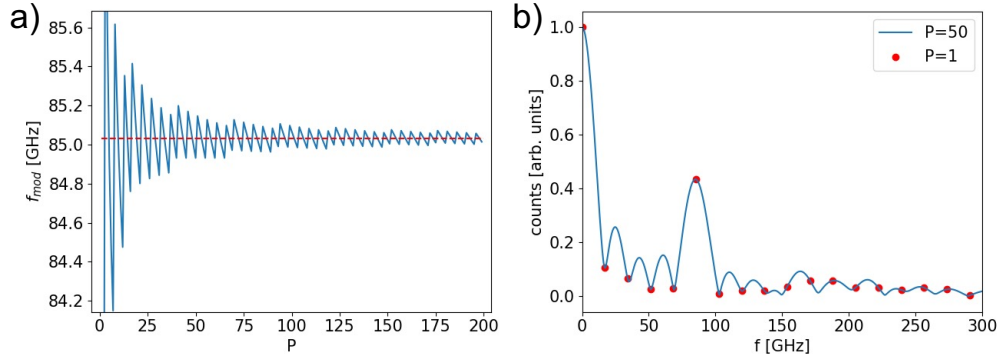

Figure 6.10: a) Peak frequency calculated with the DFT analysis on Figure 6.9b as a function of the number of zero padding arrays P (blue line). The red line indicates the frequency value to which f_{mod} converges. b) Frequency spectrum obtained from the DFT analysis on Figure 6.9b for $P = 1$ (red points) and $P = 50$ (blue line).

When the e^- bunch is not present (Figure 6.8(a)), the variation of timing over a plasma period is $\frac{rms(t)}{T_{pe}} = 0.23$. This values is close to the rms of a random distribution varying over its entire range ($1/\sqrt{12} = 0.29$). Thus, the measurement of the timing of the modulation is in agreement with random variation over T_{pe} from event to event: the self-modulation occurs as an instability (SMI). The discrepancy between the expected value of $\frac{rms(t)}{T_{pe}}$ for a random distribution and the measured one may be due to the small number of events.

When the e^- bunch is present (Figure 6.8(b)), $\frac{rms(t)}{T_{pe}} = 0.06$. The much lower value of the timing variation than in SMI demonstrates that the e^- bunch seeds SM. Figure 6.11 shows that the value of the timing variation remains essentially constant for different choices of f_{mod} around the one chosen above. Hence, the choice of the frequency bin for all events does not affect the result of the timing reproducibility analysis, as long as it is close to the frequency determined on the averaged image.
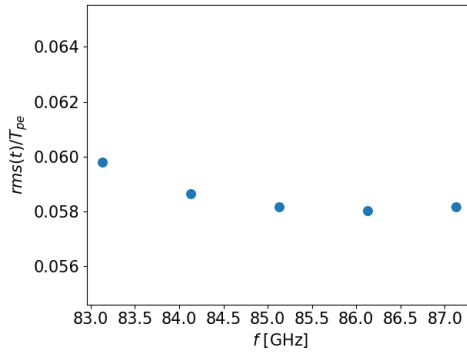

Figure 6.11: Variation of the timing over T_{pe} (rms) as a function of the frequency bin of the DFT for which the phase is calculated.

Uncertainties of the measurement

The timing variation of the microbunch train in time-resolved images may be caused by many sources of uncertainty, both due to the physics of the process and due to the diagnostics and the analysis of the images. The variation due to the physics of the process could be caused by jitters in the time of arrival of the bunches with respect to the RIF.

The p^+ bunch is synchronized with the RIF (and with the timing reference signal) with rms variation of $15\,\mathrm{ps} \ll \sigma_t$. The charge density variation at any time along the bunch is therefore 0.2%. Thus, the jitter of the time of arrival of the p^+ bunch cannot cause the seeding before the e^- bunch seeding occurs ($t_{seed} = 580\,\mathrm{ps}$, i.e. the e^- bunch travels $40\,\mathrm{ps}$ behind RIF) and it is negligible for the growth of the process.

The relative timing jitter between the timing reference signal, that is used to align the images in time, and RIF was measured to be 143 fs (rms) [90]. Since this value is convoluted with, and smaller than the uncertainty in determining the timing of the signal of 157 fs [90], we consider the effect of this jitter negligible.
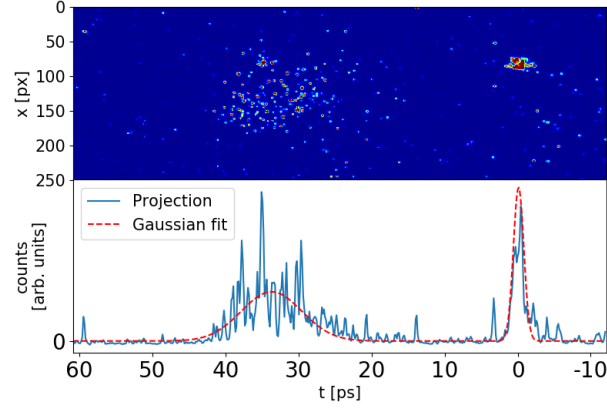

Figure 6.12: Time-resolved, 73 ps-scale, single-event image of the low-power ionizing laser pulse (at $t = 0$ ps) and the e^- bunch (centered at $t = 35$ ps). Below the image, corresponding projection along the time axis (blue line). The dashed line shows the Gaussian fit used to calculate the duration of the bunches and the center of their longitudinal distribution.

The jitter of the time of arrival of the seed e^- bunch was previously measured $rms(\Delta t_{seed}) = 0.7$ ps$\sim 0.06\, T_{pe}$ [74]. A variation of the timing of the seed bunch is crucial for the seeding process and for the timing reproducibility measurement because it induces a variation of the wakefields timing. The jitter of the time of arrival is measured calculating the variation of the delay between the ionizing laser pulse and the e^- bunch on time-resolved images using the OTR-streak camera system upstream of the vapor source [1]. Figure 6.12 shows a single-event time-resolved image of the low-power ionizing laser pulse (at $t = 0$ ps) and of the e^- bunch (at $t \sim 35$ ps). The corresponding longitudinal projection (blue line) and the Gaussian fits (red dashed line) are shown below each image. I calculate the

---

[1]For this measurement, the streak camera was positioned next to the beamline and therefore the light collection is sufficient to perform the analysis on single-event images.

delay between the two bunches as the difference in time between the center of the two Gaussian functions. This measurement is affected by the uncertainty on the determination of the center of each bunch on single-event images. I calculate this contribution using the covariance matrix of each fit. The uncertainty on the centroid of the laser pulse is $0.02\,\mathrm{ps}$ and on that of the e^- bunch is $0.2\,\mathrm{ps}$. The centroid determination is therefore a source of uncertainty, accounting for a fraction of the measured timing jitter, and it is due to the small amount of signal on single-event images.

The measured timing variation of SM with the e^- bunch seeding is in agreement with the one obtained with the ionization-front seeding [52]. In that case, the main source of uncertainty is given by the diagnostics and by the timing and frequency determination, as the timing jitter of the timing reference signal and of the p^+ bunch have negligible effects. Since I measure here a similar timing variation, I conclude that the jitter of the time of arrival of the e^- bunch does not introduce an additional source of uncertainty.

Variation of proton and electron bunch charges

The amplitude of the wakefields driven by a particle bunch increases as a function of the drive bunch density n_b (Equation 2.4 and 2.5). Since SMI develops starting from the wakefields initially driven by the p^+ bunch distribution, we expect the amplitude of these wakefields to increase when increasing the p^+ bunch charge density n_p. The seed wakefields amplitude has to be larger than the one of the initial wakefields to effectively seed SM [52]. As discussed in Section 6.5, in the experiment we increase n_p by increasing Q_p (see Figure 3.13).

Even though the amplitude of the initial wakefields driven by the p^+ bunch increases, Figure 6.13(a) shows that the $Q_e = 249\,\mathrm{pC}$ e^- bunch seeds SM for p^+ bunch charges up to $Q_p = 46.9\,\mathrm{nC}$ (the maximum value available), corresponding to $n_p = 8.9 \cdot 10^{12}\,\mathrm{cm}^{-3}$. In fact, the rms timing variation of SM remains smaller than 0.085 for all values of Q_p, when $Q_e = 249\,\mathrm{pC}$ (blue dots), and it is always larger than 0.21 when $Q_e = 0$ (red dots). In previous experiments using the ionization-seeding [52], the seeding threshold was measured between $(2.8 - 4.0)\,\mathrm{MV/m}$ for $Q_p = 48\,\mathrm{nC}$ and $n_{pe} = 0.94 \cdot 10^{14}\,\mathrm{cm}^{-3}$. The e^- bunch

seeding of SM with similar parameters of the plasma and of the p^+ bunch demonstrates that the e^- bunch drives transverse wakefields over the first meters of propagation in plasma with amplitude exceeding the seeding threshold.

The amplitude of the wakefields is also dependent on the plasma electron density ($\propto n_{pe}^{1/2}$). We therefore expect the amplitude of the initial wakefields driven by the p^+ bunch to increase as a function of n_{pe}. We will study in further experiments the effect of larger n_{pe} on the seeding threshold.
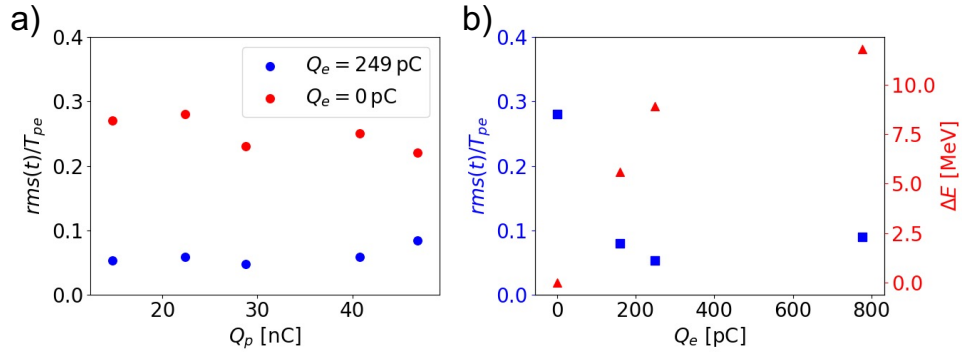

Figure 6.13: a) Variation of the modulation timing t over T_{pe} (rms) as a function of Q_p, when no seed is applied ($Q_e = 0$ red dots), and when the $Q_e = 249$ pC e^- bunch seed is present (blue dots). b) Variation of the modulation timing t over T_{pe} (rms) (blue squares, left hand-side vertical axis) for $Q_p = 14.7$ nC and energy loss measured on the electron spectrometer (red triangles, right hand-side axis) as a function of Q_e.

As discussed in Section 6.1, an e^- bunch with larger initial charge density experiences larger energy loss, indicating larger amplitude of the wakefields (see Chapter 5). The blue squares in Figure 6.13(b) show that SM is reproducible for all values of $Q_e > 0$ (minimum value is $Q_e = 147$ pC), while it is not reproducible when the e^- bunch is not present (i.e., $Q_e = 0$ pC). For each bunch, we measure the energy loss ΔE with the electron spectrometer (right hand-side vertical axis, red triangles in Figure 6.13(b)). As already discussed in Section 6.1, ΔE increases as a function of Q_e, indicating larger amplitude of the seed wakefields. This measurement validates the estimate of the seed wakefields amplitude discussed in Section 6.1.
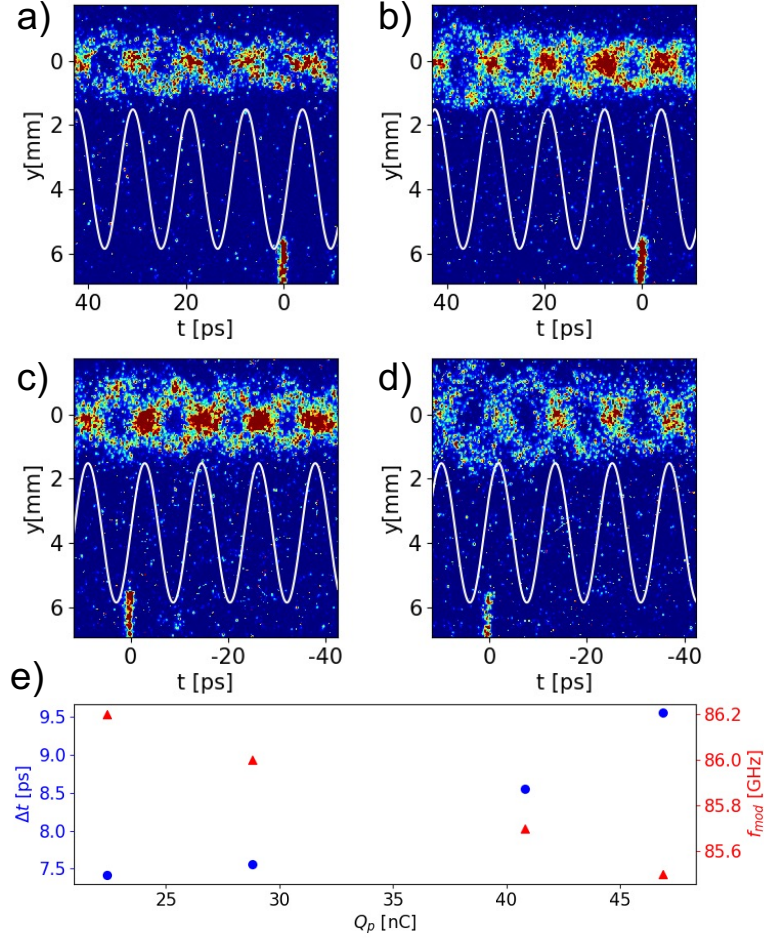
Frequency shift of the self-modulation

Figure 6.14: Averaged, $73\,\text{ps}$-scale, time-resolved images of the p^+ bunch with $Q_p = 22.4\,\text{pc}$ (a), $28.8\,\text{nC}$ (b), $40.8\,\text{nC}$ (c), $46.9\,\text{nC}$ (d). SM seeded by the e^- bunch with $Q_e = 249\,\text{pC}$. The timing reference signal is visible on each image at $t = 0\,\text{ps}$. The white lines show the cosine functions with frequency and phase calculated from the DFT on on-axis profile of each image. e) Distance in time between the timing reference signal and the first following microbunch (blue dots, left hand-side vertical axis) and frequency of the modulation f_{mod} (red triangles, right hand-side vertical axis) as a function of Q_p.

The plasma wakefields and the charge distribution of the p^+ bunch are coupled through SM. Therefore the wakefields-bunch system acts as an amplifier of the

wakefields. Previous experiments and simulation results showed that the amplitude of the wakefields grows during SM [51, 91], reaching a saturation value [59]. The growth induces a shift in the frequency of the wakefields and of the charge modulation of the bunch that is larger for larger growth rate (i.e., larger amplification) [55], depending on the drive bunch charge density. In Figure 6.14 I show 73 ps-scale, averaged, time-resolved images of the microbunch train for different values of Q_p (i.e., n_p). SM is seeded by the e^- bunch with $Q_e = 249$ pC. The parameters of the plasma and of the seed e^- bunch are kept constant. On each image, the timing reference signal is visible at $t = 0$ ps. I indicate with the white lines the cosine functions with frequency and phase obtained from the DFT analysis on each image. As summarized in Figure 6.14(e), the time interval between the timing reference signal and the first following microbunch (left hand-side vertical axis, blue dots) increases as a function of Q_p, showing that the timing of the microbunch train is delayed due to the larger growth of the wakefields. Since SM is seeded, it starts from a fixed moment in time that is given by the e^- bunch timing. A variation of the phase is thus linked to a variation in frequency. In fact, the modulation frequency (right hand-side vertical axis, red triangles), decreases as a function of Q_p.

Timing control of the self-modulation

As discussed above, the timing of the SM is determined by the timing of the seed. Therefore, we expect that, when the time of arrival of the seed e^- bunch with respect to the p^+ bunch is delayed (or advanced) by Δt_{seed}, the timing of the distribution of the microbunch train shifts by the same amount ($Q_p = const$). Figure 6.15 shows 210 ps-scale, averaged, time-resolved images of the p^+ bunch without (a) and with plasma and seed e^- bunch ((b), (c)). For (c), the e^- bunch is delayed by $\Delta t_{seed} = 6.7$ ps with respect to the case of (b). Both (b) and (c) clearly show full charge density modulation of the microbunch train charge distribution, because SM is reproducible and seeded by the e^- bunch. I perform the DFT analysis on the on-axis profiles (Figure 6.15(d), blue line: profile of (b), orange line: profile of (c)) and I measure the timing difference $\Delta t = T_{pe} \frac{\Delta \varphi}{2\pi} = (7.2 \pm 1.0)$ ps. The error is calculated by propagating the rms

timing variation of the two datasets obtained from the DFT analysis on the single-event images. This confirms that the timing of the wakefields is tied to the timing of the seed ($\Delta t \sim \Delta t_{seed}$), and that it is possible to control the timing of the p^+ driven wakefields by tuning the delay between the seed e^- and p^+ bunches.
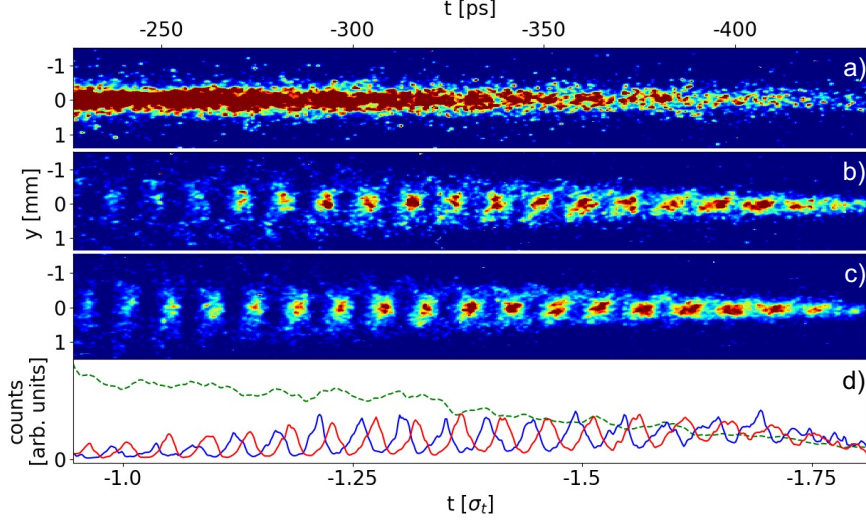

Figure 6.15: Averaged, 210 ps-scale, time-resolved images of the p^+ bunch with $Q_p = 14.7$ nC in case of: a) no plasma, b) plasma and $Q_e = 249$ pC e^- bunch, with $t_{seed} = 6$ ps, c) $t_{seed} = 12.7$ ps. d) On-axis profiles of (a): green dashed line, (b) and (c): blue and red line, respectively. The profiles are obtained by summing the counts in the transverse direction between $y = \pm 0.1$ mm. The center of the p^+ bunch is at $t = 0$ ps.

Comparing the images without (Figure 6.15(a)) and with (Figure 6.15(b) and (c)) plasma, one can see that SM develops from the (visible) front of the bunch (the images are taken between 0.95 and 1.82 σ_t ahead of the center of the p^+ bunch), as expected from the fact that the seed wakefields act on the entire p^+ bunch. I also note that the charge density at the bunch front ($t < -350$ ps) is higher in the cases with plasma than in the cases without. This is both due to the formation of the microbunches and to the global focusing effect discussed in Section 6.2.

The microbunches are formed along the propagation axis of the p^+ bunch, whose trajectory is aligned with that of the ionizing laser pulse. Thus, the mi-
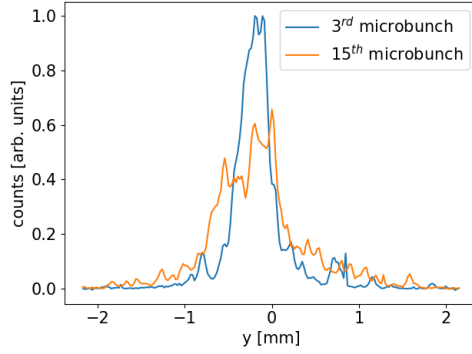
Figure 6.16: Transverse profile of the 3rd (blue line) and of the 15th microbunch (orange line) from Figure 6.15(c).

crobunches travel in plasma for the entire propagation distance. They drive the wakefields and are influenced by their amplitude, since SM is a self-consistent process. Their parameters are the result of the effect of the transverse wakefields integrated over the plasma length. The analysis of the defocused regions along the bunch (see Sections 6.4 and 6.5) shows that, as expected from previous experimental results [51, 74], the amplitude of the wakefields grow along the bunch. Therefore, one may expect the effect of the transverse wakefields to produce a smaller size of the microbunches along the bunch at the plasma exit, possibly also with larger emittance due to the nonlinear nature of the transverse wakefields. The smaller transverse size and larger emittance of the successive microbunches at the plasma exit are the likely causes for the increase in transverse size at the screen of the microbunches along the bunch (as observed in Figure 6.15(b) and (c)), since the OTR screen is positioned 3.5 m downstream of the plasma exit. For example, as visible in Figure 6.16, the transverse profile of the 15th microbunch (orange line, $t = -260$ ps in Figure 6.15(c)) is broader than that of the 3rd microbunch (blue line, $t = -394$ ps in Figure 6.15(c)).

The increase of the transverse width of the successive microbunches at the OTR screen is also the reason for the decreasing in charge density along the microbunch train. In fact, the slit of the streak camera collects less light per unit transverse size for a larger than for a narrower bunch. This also explains the smaller amount of signal in the seeded SM case than in the SMI case in Figure 6.8.

At the same location along the bunch, the seeded SM is already fully developed and the microbunches experience wakefields with larger amplitude.
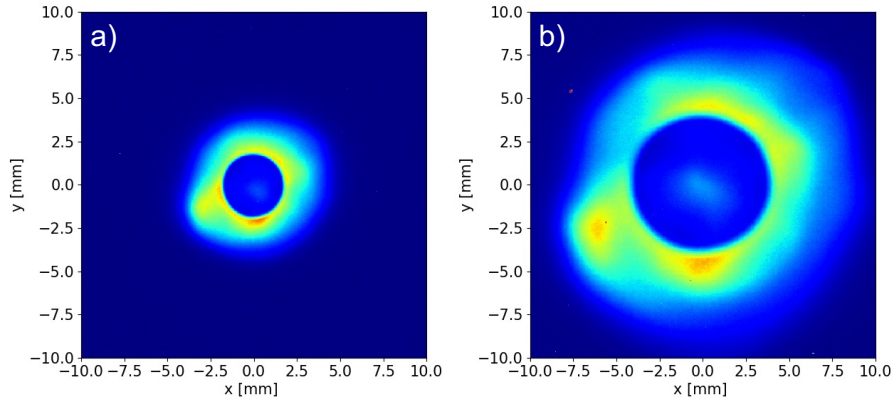
Transverse time-integrated imaging

Figure 6.17: Time-integrated, transverse images of the self-modulated $Q_p = 14.7\,\text{nC}$ p^+ bunch acquired by the halo cameras. SM is seeded by the $Q_e = 249\,\text{pC}$ e^- bunch. a) IS 1, b) IS 2.

From Figure 6.15(b) and (c), I note that the microbunch train develops symmetrically with respect to the propagation axis of the p^+ bunch, showing no sign of the hosing instability [104], as the seed wakefields are aligned on the p^+ beam trajectory. However, an oscillation in the plane perpendicular to that of the slit of the streak camera would be not visible on the time-resolved images. Thus, we use the Imaging Stations (IS, see Section 3.1) to study the time-integrated, transverse distribution of the p^+ bunch.

The images of the halo cameras (Figure 6.17(a): IS 1, (b): IS 2) show no obvious sign of hosing instability. In that case (see Section 6.6), the IS images would not be round and would show a clear elongation along the axis where the instability occurs. Hence, in the results discussed in this Section the hosing instability does not occur. As SM develops from the front of the bunch, the light visible in the bunch core corresponds to the charge contained in the microbunch train. Further studies on the seeded hosing are ongoing and will be briefly discussed in Section 6.6.

Summary

In conclusion, I have shown that an e^- bunch can seed SM of a long p^+ bunch in plasma. I have demonstrated that the timing of SM is reproducible and that it is controlled by the timing of the e^- bunch. When increasing the charge of the p^+ bunch, the frequency of the modulation is shifted due to the slowdown of the wakefields during the SM growth.

6.4   Seed wakefields amplitude

Theoretical and numerical simulation results [48, 55, 56, 105] show that, in the linear regime, the amplitude of the transverse wakefields grows along the bunch (t) and along the plasma (z) as:

$$W_\perp(t, z) = W_{\perp 0} \exp\left(\Gamma(t, z)z\right). \qquad (6.4)$$

When seeding with an e^- bunch, the amplitude of the initial wakefields $W_{\perp 0}$ depends solely on the e^- bunch parameters (see Equation 2.5), while the growth rate $\Gamma(t, z)$ depends solely on those of the p^+ bunch (see Equation 2.12).

The protons that are defocused during the growth of the self-modulation are probes of the wakefields at early times along the plasma, before saturation [51, 91] because they reach a transverse position at the OTR screen that depends on the transverse momentum they have acquired from the transverse wakefields (see Equation 3.2). Thus, the transverse distribution of the bunch at the screen is related to the amplitude of the wakefields experienced by the defocused protons, even though this amplitude cannot be calculated directly because the position along the plasma where the protons leave the wakefields is unknown (the length of the plasma is much longer than the saturation length).

Using 1.1 ns-scale, time-resolved images of the p^+ bunch as in Figure 6.18, we measure the width of the transverse distribution along the bunch so as to study the growth of the self-modulation. As discussed in Section 3.2.3, I define the contours of the transverse distribution calculating for each time-column the points where the transverse profile reaches 20% of its maximum. The transverse

distance between the contour lines defines the transverse extent w along the bunch.
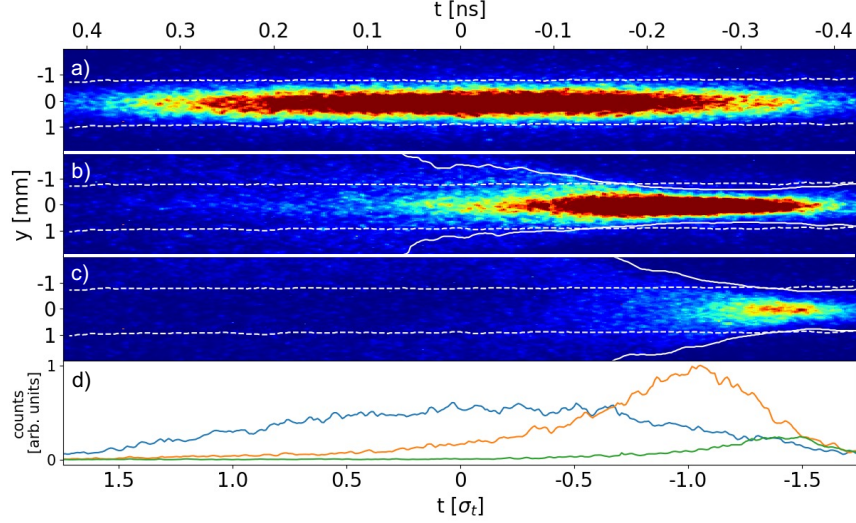

Figure 6.18: 1.1 ns-scale, time-resolved images of the p^+ bunch with $Q_p = 14.7$ nC in case of: a) no plasma, b) plasma and no e^- bunch, c) plasma and $Q_e = 249$ pC seed e^- bunch. d) Longitudinal profiles calculated as the sum of the counts between $y = \pm 0.2$ mm on (a), (b) and (c): blue, orange and green lines, respectively. Bunch center at $t = 0$ ps, the bunch travels from left to right. Horizontal axis: time along the bunch normalized to the incoming bunch duration σ_t.

In case of no plasma (Figure 6.18(a)), the transverse charge density distribution is Gaussian ($\sigma_y = 0.38$ mm), and represents the incoming bunch. The transverse extent $w_{off} = 1.7$ mm is constant along the bunch (the white dotted lines show the contours).

Figure 6.18(b) shows the result of the same analysis for the case with plasma and without seed e^- bunch, for which SMI occurs (see previous Section, Figure 6.8(a)). The transverse extent along the bunch (white continuous lines) first becomes smaller than the initial one ($t < -0.8\,\sigma_t$) showing the effect of the global focusing due to adiabatic response of the plasma. Later along the bunch, the effect of defocusing due to SM dominates and w increases. The global focusing effect can also be seen in Figure 6.18(d) where the on-axis profile for the SMI case (orange

line) is above that of the case without plasma (blue line) for $-1.5 < t < -0.7\,\sigma_t$.

Figure 6.18(c) shows the case with plasma (n_{pe} and Q_p are the same as in (b)) and the seed e^- bunch ($Q_e = 249\,\mathrm{pC}$), for which seeded SM occurs (see previous Section, Figure 6.8(b)). The same global focusing effect dominates at the front of the bunch as in the SMI case (b), but the effect of defocusing starts earlier: $t \sim -1.5\,\sigma_t$ rather than $t \sim -0.8\,\sigma_t$ (Fig. 6.18(b)). Since w depends on the transverse momentum $p_\perp$ acquired from $W_\perp$, this indicates the the transverse wakefields reach larger amplitudes earlier along the bunch in the seeded case than in the SMI case. I also note that, comparing the time axis of Figure 6.18(c) and Figure 6.15(b,c) (plotted with respect to the same time from the center of the bunch), in the seeded case the microbunches are already present during the global focusing, whereas in the SMI case the full modulation becomes visible only later along the bunch, as already discussed on Figure 6.8(a). This is due to the fact that the seed wakefields act on the entire bunch, with amplitude larger than that of the wakefields initially driven by the p^+ bunch. Thus, SM occurs earlier along the bunch and along the plasma, when seeded.

I calculate the radial distance reached by the protons and the transverse extent w along the bunch using averaged images to take advantage of the improved signal-to-noise ratio of these images. Figure 6.19 shows that the value of w along the bunch obtained from an averaged image (blue curve) is equivalent to the average of w calculated on the single-event images (green points).

When the charge of the seed e^- bunch Q_e increases, the bunch loses more energy in plasma (see Section 6.1). Along with the analysis on the simulation results (Chapter 5), I concluded that larger energy loss corresponds to larger amplitude of the wakefields driven over the first meters of propagation in plasma. Since seeding occurs (see previous Section) the amplitude of the seed wakefields exceeds the seeding threshold [52].

Figure 6.20(a) shows the transverse extent w along the p^+ bunch after propagation in plasma, for various values of Q_e. The red points indicate the time along the bunch when w reaches the value of the transverse extent in case of no plasma (w_{off}), showing that the defocusing effect due to SM becomes dominant earlier for larger Q_e. This and the increase in w at all times when defocusing
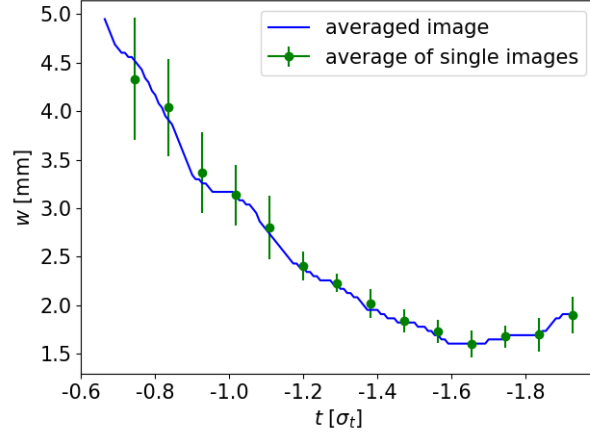
Figure 6.19: Transverse extent calculated on the charge density distribution of Figure 6.18(c) (blue line). The green points show the average of the transverse extent calculated on the single-event images. The errorbars indicate the standard deviation. The horizontal axis is in units of the bunch duration σ_t. The bunch center is at $t = 0$.

dominates are directly caused by the increase in $W_{\perp 0}$ with Q_e, since all other parameters are kept constant (in particular, $\Gamma = const$), and it is in agreement with the observation of larger energy loss of the e^- bunch. In fact, larger $W_{\perp 0}$ causes larger growth of $W_\perp$ at all times along the bunch and along the plasma (see Equation 6.4).

Figure 6.20(b) shows the value of w as a function of Q_e, at $t = -1.19\,\sigma_t$ (blue points) and $-0.84\,\sigma_t$ (red points), confirming that the value of w is consistently larger for larger Q_e, at a fixed t along the bunch. The vertical error bars indicate the variation of w from single images and the horizontal error bars calculated from variation of Q_e.

In all cases, w initially follows the same evolution as in the case with residual density (gray line in Figure 6.20(a)). This shows that the focusing effect due to the plasma adiabatic response is independent of n_{pe} (as long as there are enough plasma electrons to cancel out the space-charge field of the bunch) and that the transition between global focusing and global defocusing (i.e., the time along the bunch when $w = w_{off}$) depends on Q_e, that defines $W_{\perp 0}$. The superimposition of the two effects on the transverse extent of the bunch is schematically shown in
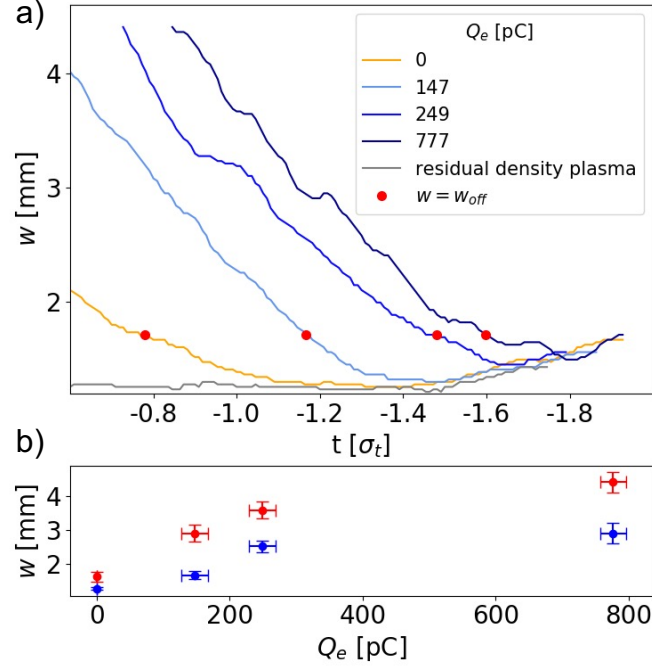
Figure 6.20: a) Transverse extent w along p^+ bunch with $Q_p = 14.8\,\text{nC}$ in case of plasma with residual density (gray line), plasma and $Q_e = (0, 147 \pm 22, 249 \pm 17, 777 \pm 29)\text{pC}$ (orange, light blue, blue, dark blue lines). The red points show when $w = w_{off}$. The time axis is in units of the incoming bunch duration. b) Transverse extent w calculated at $t = -1.19\,\sigma_t$ (blue points) and $-0.84\,\sigma_t$ (red points) from Fig.(a). The vertical error bars indicate the variation of w on the single images. Horizontal error bars are calculated from the variation on the geometrical properties of the p^+ bunch σ_t and $\sigma_{x,y}$.

Figure 6.21. The blue dashed line shows the effect on w of the adiabatic focusing, that increases along the bunch following its Gaussian density distribution. The red dashed line shows the SM defocusing effect, that grows along the bunch. The sum of the two components (green line) shows a first decreasing of w to values smaller than the initial one (w_0) and then an increasing with the growth of SM. When increasing $W_{\perp 0}$, while keeping the parameters of the p^+ bunch constant, SM defocusing dominates earlier but the front of the bunch follows the same evolution in all cases, as shown in Figure 6.20(a).

When the seed bunch is not present ($Q_e = 0\,\text{pC}$, orange line in Figure 6.20(a))
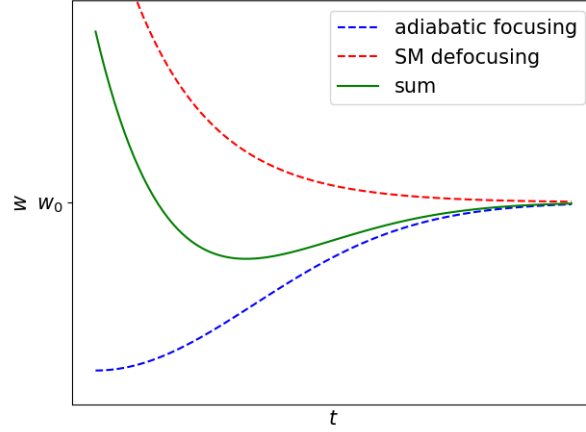
Figure 6.21: Transverse extent w along the bunch (green line, the bunch travels from left to right) calculated as the sum of the contribution from the adiabatic focusing (blue dashed line) and from SM defocusing (red dashed line).

the process occurs in the SMI regime. In this case, not only does the transverse extent stay in the global focusing for longer than when seeding occurs, but w also grows with a slope considerably smaller than in the seeded case. This may be due to the fact that less charge contributes to the driving and to the growth of the wakefields. In fact, the growth rate is defined as $\Gamma(t - t_0)$, where t_0 is time of the start of SM. In the seeded case, $t_{seed} = t_0$, whereas in the SMI case $t_0 > t_{seed}$.

Also the transverse, time-integrated charge distribution observed at IS 2 (Figure 6.22) shows that when the value of Q_e is larger, the halo formed by the defocused protons reaches larger extent, indicating larger amplitude of the wakefields due to the larger growth of the wakefields. These images are complementary to the time-resolved images: the portion of OTR passing through the slit of the streak camera corresponds to a diameter of the transverse distribution visible on the halo images.

In the case with $Q_e = 0\,\mathrm{pC}$ (SMI, (a)) the core of the p^+ bunch is much brighter than in the seeded cases and the radius of the halo is shorter. When SM occurs as an instability the full modulation occurs later along the bunch and along the plasma than when SM is seeded. For this reason, more charge remains on the propagation axis (the total amount of charge is preserved), especially at
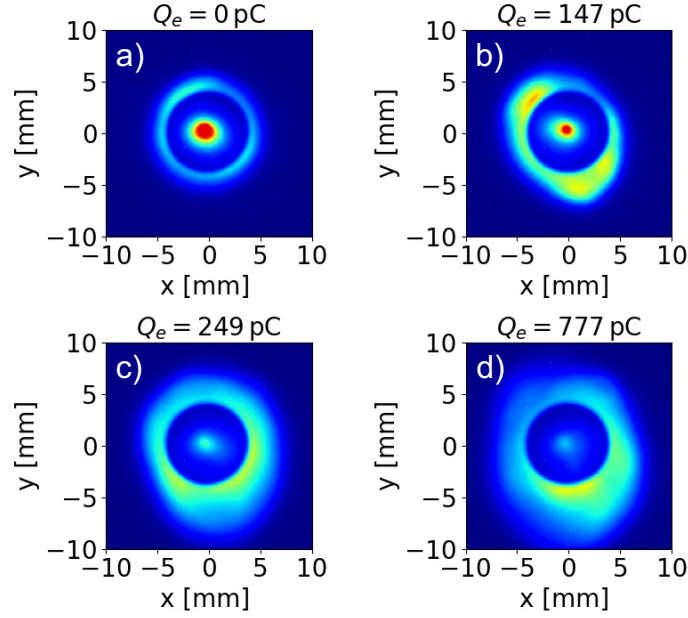
Figure 6.22: Time-integrated, transverse images of the self-modulated $Q_p = 14.7\,\text{nC}$ p^+ bunch from the halo camera of IS 2. a) $Q_e = 0\,\text{pC}$ (no seed bunch). b, c, d) $Q_e = 147, 249, 777\,\text{pC}$, respectively.

the bunch front, as it was already discussed on Figure 6.8. The elongation of the transverse distribution in Figure 6.22(b) indicates that the alignment of the e^- beam trajectory is not optimal and that a hosing component may be present.

In conclusion, I have shown in this Section that when seeding SM with an e^- bunch it is possible to control the amplitude of the seed wakefields, and therefore the growth of SM, by varying the properties of the e^- bunch ($\Gamma = const$). I have also shown that the effect of the plasma adiabatic response is dominant at the bunch front independently of the plasma electron density and that the transition to the SM defocusing effect depends on the amplitude of the seed wakefields.

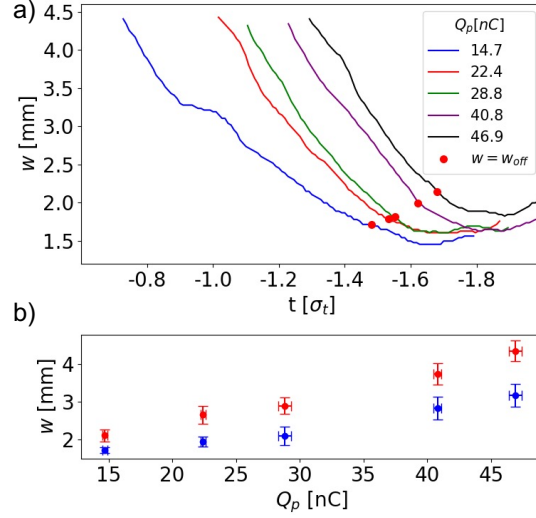Figure 6.23: a) Transverse extent w along the self-modulated p^+ bunch for different values of Q_p. $Q_e = 249\,\mathrm{pC}$ kept constant. The horizontal axis is in units of the incoming bunch duration σ_t. b) Transverse extent w as a function of Q_p for $t = -1.48\,\sigma_t$ (blue points) and $-1.30\,\sigma_t$ (red points) from the measurements on (a). The vertical error bars indicate the variation of w on the single images. Horizontal error bars are calculated from the variation on the geometrical properties of the p^+ bunch σ_t and $\sigma_{x,y}$.

6.5   Growth rate of the self-modulation

The amplitude of the wakefields in the linear regime driven by the self-modulated p^+ bunch increases along the plasma as $e^{\Gamma z}$, where Γ is the SM growth rate (see Equation 6.4). At a fixed position z along the plasma, Γ is a function of the peak p^+ bunch charge density n_p and of the time along the bunch t as $\Gamma \propto (n_p \cdot t)^{1/3}$ (see Equation 2.12). Thus, increasing n_p, while keeping all the other parameters constant, increases the value of Γ, without changing the seed wakefields amplitude $W_{\perp 0}$. As a consequence the amplitude of the wakefields increases at all times along the bunch and at any position along the plasma.

To study the effect of the variation of Γ on SM, we measure the transverse extent w along the p^+ bunch while varying n_p (see Section 3.2.3). In the experiment, we vary n_p by varying Q_p (see Figure 3.13 and parameters of the bunch in
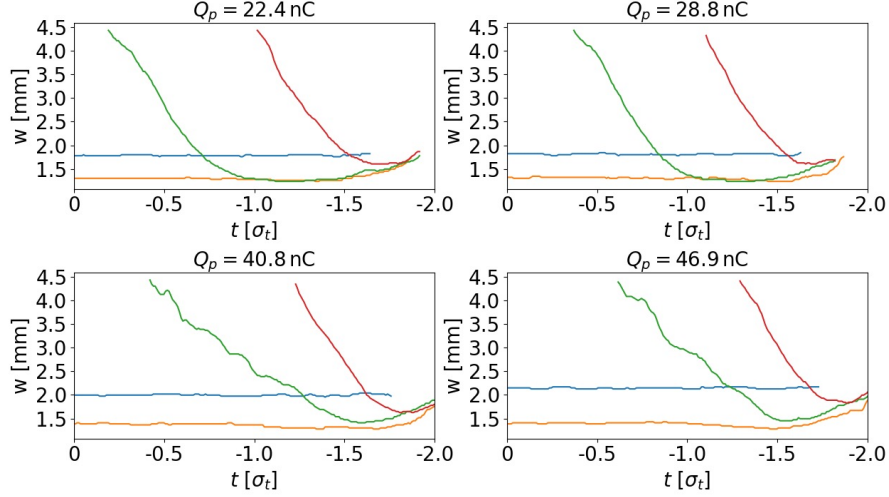
Table 3.1).

Figure 6.24: Transverse extent w along the p^+ bunch for different values of Q_p (indicated in the title of each plot) in case of no plasma (blue lines), plasma with residual density (orange lines), plasma and no seed bunch (green lines) and with seed bunch (red lines). The horizontal axis is expressed in units of the bunch duration for each image.

Figure 6.23(a) shows that the transverse extent w along the p^+ bunch for different values of Q_p, while all the parameters of the plasma and of the seed e^- bunch are kept constant. For all cases, the plasma adiabatic response dominates at the bunch front. As discussed in Section 6.2, this focusing effect is stronger for larger Q_p (i.e., larger n_p). Therefore, the fact that the defocusing effect due to SM dominates earlier along the bunch for larger Q_p, as shown by the red points, indicates that the transverse wakefields reach larger amplitude earlier along the bunch when increasing Q_p. Figure 6.23(b) shows w as a function of Q_p for $t = -1.48\,\sigma_t$ (blue points) and $-1.30\,\sigma_t$ (red points). The increasing values of w with Q_p at all time along the bunch when $w > w_{off}$ is directly caused by the increase in the growth rate of the self-modulation, since all other parameters are kept constant (in particular, $W_{\perp 0} = const$).

Figure 6.24 shows that, for different values of n_p, the effect of defocusing due to SM always dominates earlier in the seeded case (red lines) than in SMI (green

lines). In all cases with plasma, w at the bunch front follows the same trend as in the case with residual density (orange lines), showing again that the focusing effect due to the plasma adiabatic response dominates until the transverse wakefields grow to comparable amplitude.
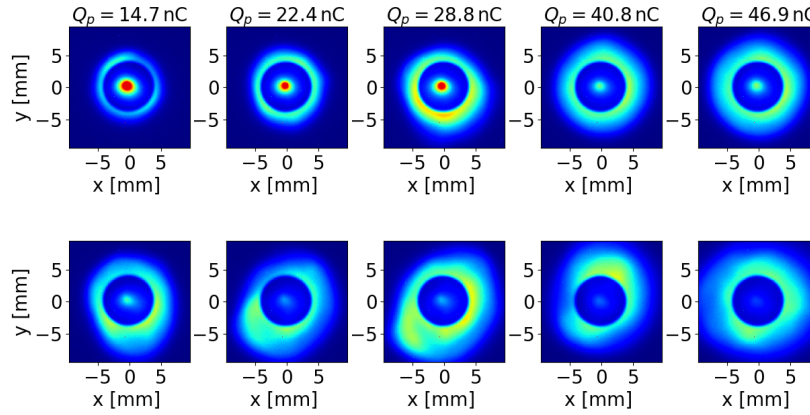
Figure 6.25: Time-integrated transverse images of the self-modulated p^+ bunch from the halo camera of IS 2. Top row: no seed bunch. Bottom row: $Q_e = 249\,\mathrm{pC}$. The value of the p^+ bunch charge density Q_p is indicated above each column. Same color scale for all the images.

Also the transverse, time-integrated charge distribution of the p^+ bunch observed at the IS 2 (Figure 6.25, top row: SMI, bottom row: $Q_e = 249\,\mathrm{pC}$, seeded SM) shows that, for a larger value of Q_p, the halo formed by the defocused protons becomes larger, indicating larger amplitude of the wakefields due to the larger growth rate of SM. For the same reason, the halo reaches larger transverse distance when seeding, indicating larger growth [51].

I have shown in this Section that when seeding SM with the e^- bunch it is possible to control the growth rate, and therefore the growth, of SM by varying the properties of the p^+ bunch ($W_{\perp 0} = const$).

6.6   Seeded hosing of the proton bunch in plasma

Hosing is a beam-plasma instability where the centroid of the bunch transverse distibution oscillates along the bunch [104], akin to the beam break-up instability in conventional accelerators. As a consequence, and unlike in SM, the transverse charge distribution along the bunch becomes asymmetric with respect to the propagation axis. When the oscillation of the transverse centroid is coupled to the transverse wakefields, it has periodicity $\sim T_{pe}$. Moreover, the amplitude of the oscillation grows along the bunch and along the plasma [104, 106, 107]. Theoretical and simulation studies have shown that hosing instability can grow from the variation of the centroid in the initial transverse distribution along the bunch or from an asymmetric transverse interaction with the wakefields (e.g. when one side of the beam is closer to the boundary of the ion channel [104]).

In previous experiments with the p^+ bunch in AWAKE, the hosing instability was observed only at low density ($n_{pe} \sim 0.5 \cdot 10^{14}\,\mathrm{cm}^{-3}$) and when SM was not seeded [108]. As the instability grows from the random variations in the bunch charge distribution or from a trajectory misalignment, the timing of the centroid oscillation changes from event to event, similarly to the radius oscillation in the SMI case.

In the experiment presented in the previous Sections, hosing was not observed. When the trajectories of the e^- and p^+ beam coincide, the seed wakefields driven by the preceding e^- bunch act on the p^+ bunch symmetrically around the propagation axis, modulating the transverse size along the bunch but not the transverse position of the centroid. Similarly to SM, hosing can also be seeded by initial seed wakefields that impose a first oscillation of the transverse centroid position along the bunch, from which the instability grows.

Figure 6.26(a) shows a 73 ps-scale, averaged, time-resolved image of the p^+ bunch when the trajectory of the preceding e^- bunch is purposely misaligned with respect to that of the p^+ bunch at the plasma entrance. The timing setup and plasma electron density are the same as in the previous Sections. The p^+ bunch develops in a series of beamlets whose distribution is clearly asymmetric with respect to the propagation axis ($y = 0\,\mathrm{mm}$), which is the main signature

of the hosing instability. Moreover, the averaged image shows high contrast and signal-to-noise ratio, indicating that the distribution is reproducible throughout the single-event images.
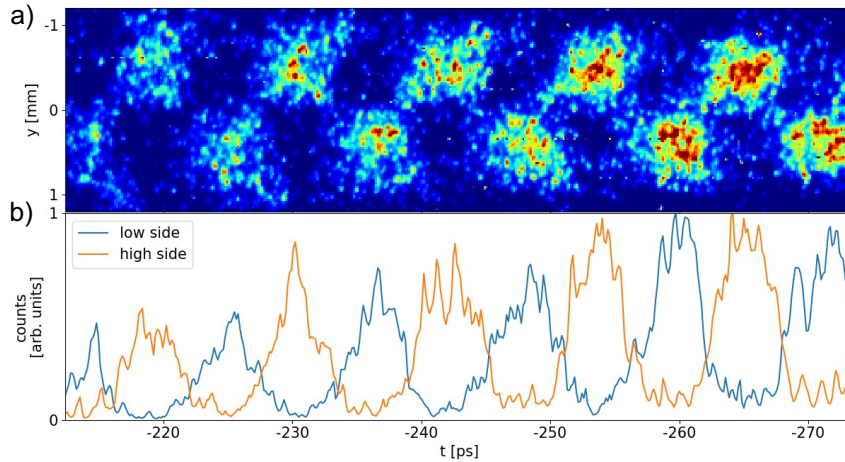

Figure 6.26: a) 73 ps-scale, time-resolved image of the $Q_p = 14.7\,\mathrm{nC}$ p^+ bunch between 205 and 278 ps ahead of the center of the bunch. Average of 10 events. The trajectory of the e^- bunch is misaligned with respect to that of the p^+ bunch. $Q_e = 249\,\mathrm{pC}$. b) Longitudinal profile between $y = 0.2$ and $0.8\,\mathrm{mm}$ (low side: blue line) and between $y = -0.2$ and $-0.8\,\mathrm{mm}$ (high side: orange line).

The profile of the distribution of each "side" is shown in Figure 6.26(b). The modulation of the two profiles have periodicity $T_{mod} = 10.8\,\mathrm{ps}$ (low side, blue line) and 10.9 ps (high side, orange line) $\sim T_{pe}$ and are π out of phase with respect to each other. Analyzing the timing of each profile with the DFT analysis already discussed in Section 6.3, I calculate the variation of the timing over one plasma period $rms(t)/T_{pe} = 0.05$ for both profiles. This demonstrates that the charge distribution is reproducible from event to event and that the oscillation of the bunch centroid is seeded by the wakefields driven by the preceding e^- bunch.

The intensity of the successive beamlets decreases along the bunch. This may be explained as for the SM case (Section 6.3), considering the increasing divergence of the successive beamlets at the plasma exit due to the growth of the instability

and of the oscillaton along the bunch.
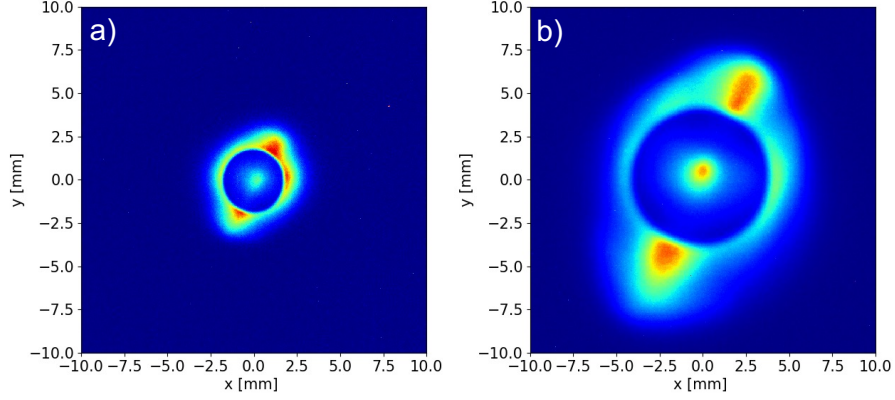
Figure 6.27: Time-integrated, transverse images of the p^+ bunch for one of the events composing Figure 6.26 a) IS 1, b) IS 2.

Figure 6.27((a): IS 1, (b): IS 2) shows the transverse, time-integrated images of the p^+ bunch for one of the events composing Figure 6.26. The transverse charge distribution is not round and an elongation is clearly visible along the axis where the hosing instability occurs. Moreover, a larger amount of charge remains in the bunch core than in the SM case (Figure 6.17), indicating that hosing is the dominating process.

In conclusion, when the p^+ beam trajectory is not aligned with the seed wakefields, we do not observe the self-modulation of the p^+ bunch. Instead, the p^+ bunch evolves into an asymmetric distribution with periodic oscillation of the bunch centroid, in agreement with the hosing instability. Further studies on the tolerances on the trajectory misalignment are ongoing. As already mentioned, in previous experiments hosing was only observed as an instability [108] and therefore the bunch charge distribution was not reproducible from event to event. I have shown here for the first time that the hosing instability can be seeded by a preceding e^- bunch, hence it is reproducible from event to event.

6.7 Three-dimensional self-modulation imaging

In the previous Sections, I have shown that SM of the p^+ bunch is seeded by the e^- bunch and that the charge density distribution on time-resolved images is axisymmetric when hosing instability does not occur. However, a hosing component in the plane perpendicular to the slit of the streak camera would not be visible in the time-resolved images and may only be inferred from the time-integrated, transverse images.
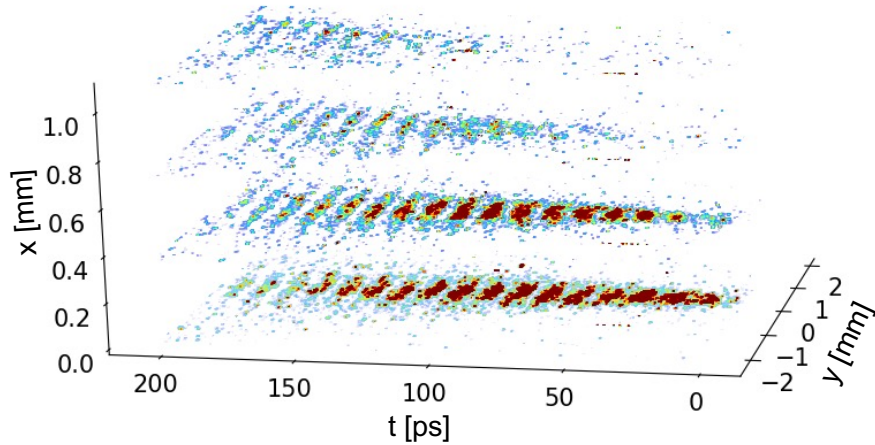
Figure 6.28: Three-dimensional image of the self-modulated p^+ bunch with $Q_p = 14.7$ nC. The SM is seeded by the $Q_e = 249$ pC e^- bunch. Each slice is the average of ten consecutive 210 ps-scale time-resolved images. The vertical axis corresponds to the transverse position of the OTR on the slit of the streak camera.

We can obtain time-resolved images of longitudinal slices of the charge density distribution of the p^+ bunch at different heights (see Section 3.2.5), by varying the alignment of the OTR on the slit of the streak camera. Figure 6.28 shows four 210 ps-scale, averaged, time-resolved images of the p^+ bunch, when SM is seeded by the e^- bunch. Each slice is positioned on the vertical axis depending on the position of the OTR on the slit, composing a three-dimensional image. The distribution in each slice is axi-symmetric. For example, the microbunch at $t = 150$ ps is always visible and its transverse distribution is centered on-axis

(y) on all slices (x). Figure 6.29 shows the sum of all slices from Figure 6.28. The distribution is axi-symmetric, further confirming that hosing instability is not visible in any plane, included the one perpendicular to the slit of the streak camera.
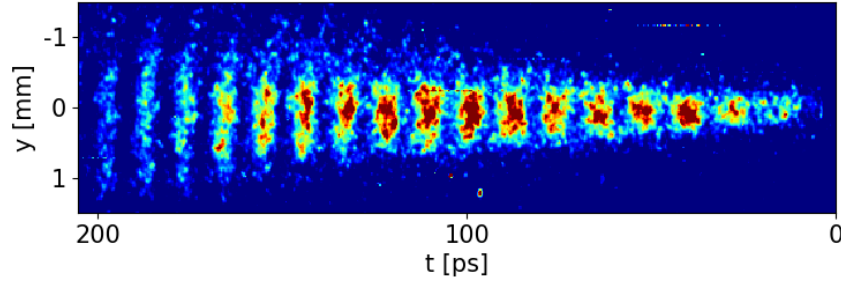
Figure 6.29: Sum of the slices from Figure 6.28.

The three-dimensional reconstruction also allows to study the evolution of the width of the microbunches along the bunch. The first microbunch (at $t = 16\,\text{ps}$) is only visible in the slice on-axis ($x = 0\,\text{mm}$). This means that its transverse width is smaller than the minimum displacement on the slit ($x = 0.36\,\text{mm}$). From the eight microbunch on ($t > 100\,\text{ps}$), the signal becomes visible on the third slice. Therefore, the transverse width of the microbunch becomes larger than $x = 0.72\,\text{mm}$. A clear microbunch structure is visible on the fourth slice ($x = 1.08\,\text{mm}$) only for $t > 150\,\text{ps}$. As already discussed in Section 6.3, this shows an increasing width of the successive microbunches at the screen, likely due to a smaller size and larger emittance at the plasma exit. This is caused by the growing amplitude of the wakefields along the bunch. Moreover, the three-dimensional image shows that the microbunches are radially symmetric, since the transverse broadening of the microbunches is also visible on each slice.

I have shown here for the first time a method to reconstruct the three-dimensional charge density distribution of the self-modulated p^+ bunch. This method allows to perform physics studies complementary to those done on the central slice, such as the evolution of the microbunch width in the horizontal plane

and the diagnosis of the hosing instability in the plane perpendicular to the slit of the streak camera.

Chapter 7

Conclusions & Outlook

When a long, narrow, relativistic, charged particle bunch travels in plasma, it undergoes the self-modulation instability. In this thesis, I have shown experimentally for the first time, using a long, relativistic p^+ bunch, that a preceding e^- bunch can seed the instability. I have demonstrated that the timing of the p^+ microbunch train, and therefore of the wakefields, is defined by the timing of the seed e^- bunch and that it is reproducible from event to event.

The characteristics of the defocused protons yield more information about the evolution of the self-modulation than the microbunches. This is because the effect of the defocusing fields stops once the protons leave the wakefields. So, defocused protons have in general experienced the wakefields only over the growth of the self-modulation. I have shown that, when seeding with the e^- bunch, the amplitude of the seed wakefields and the growth rate of the instability can be varied independently from one another. When increasing the charge of the seed e^- bunch, the amplitude of the seed wakefields is larger, as indicated by the larger amount of energy lost by the electrons in plasma. Therefore the wakefields driven by the self-modulated p^+ bunch reach larger amplitude at all positions along the plasma and at all times along the bunch, due to the larger growth of the self-modulation. Analogously, increasing the p^+ bunch charge increases the growth rate of the self-modulation and therefore the amplitude of the wakefields at all times along the bunch, while leaving the seed wakefields unchanged.

I have also demonstrated that the front of the bunch is focused by the effect of the adiabatic response of the plasma to the presence of the bunch. After the effect of self-modulation has grown to comparable amplitude, the defocusing effect dominates on the transverse profile of the bunch. The transition between the two effects depends on the amplitude of the seed wakefields.

I have shown that, when the trajectory of the seed e^- bunch is misaligned with respect to that of the p^+ bunch, the hosing instability occurs. The experimental results presented here show for the first time indication of seeded hosing.

I have also discussed a method to obtain three-dimensional images of the self-modulated p^+ bunch, by varying the position of the OTR with respect to the entrance slit of the streak camera. This method allows to study the evolution of the microbunch train along the bunch in the plane perpendicular to the slit.

These studies took place in the context of the AWAKE experiment, whose goal is to use the wakefields driven by a long, self-modulated p^+ bunch to accelerate an externally injected e^- bunch to GeV energies, while preserving its initial bunch quality. To allow for on-axis external injection in vacuum, after the self-modulation reaches saturation, the setup of future experiments will consist of two plasma sections, separated by a gap region. Thus, it is needed that the entire p^+ bunch self-modulates with timing and amplitude reproducible from event to event. This can be obtained by seeding the instability with the wakefields driven by a preceding e^- bunch.

This thesis summarizes the main achievements of the first year of AWAKE Run 2a. The work presented here contributes significantly to the understanding and control of the self-modulation and to the feasibility of the future design of the experiment. The e^- bunch seeding of the self-modulation in plasma is an important milestone on the path towards proton driven plasma wakefield acceleration of e^- bunches, with quality and energy suitable for high-energy physics applications.

For the remaining part of Run 2a, the experimental program will focus on the study of the e^- bunch seeding at higher plasma electron densities, on the competition between the self-modulation instability in the front of the bunch with

the seeded self-modulation in the back of the bunch, and on the seeded hosing.

In 2023, a new vapor source will be installed to study the effect of plasma density step on the self-modulation (Run 2b).

Starting in 2024, major interventions on the experimental facility are planned to take place to allow for the installation of the second vapor source, of a new 150 MeV electron beamline, of a second ionizing laser pulse line and of additional diagnostics. The start of Run 2c is foreseen for 2028. The goal is to demonstrate high-quality plasma wakefield acceleration to GeV energies.

Afterwards, the use of novel plasma sources will be investigated (Run 2d) to prove the scalability of the process to higher energies (tens of GeVs), leading to the first particle physics applications within the next decade.

Glossary

arb. units	arbitrary units	
AWAKE	Advanced Wakefield Experiment	
B	magnetic field	
B_{theta}	azimuthal magnetic field	
$B_{x,y}$	Earth's magnetic field in the experimental hall	
BPM	Beam Position Monitor	
BTV	Beam Scintillating Screen	
c	speed of light in vacuum	$c = 2.998 \cdot 10^8 \,\mathrm{m/s}$
CLIC	Compact Linear Collider	
CERN	European Centre of Nuclear Research	
CTR	coherent transition radiation	
CPA	chirped pulse amplificiation	
δn	plasma density perturbation	
DESY	Deustsches Elektronen-Synchrotron	
DFT	discrete Fourier transform	
ε_0	vacuum permittivity	$\epsilon_0 = 8.85 \cdot 10^{-12} \,\frac{\mathrm{As}}{\mathrm{Vm}}$
ϵ_N	normalized bunch emittance	
e	elementary charge	$e = 1.602 \cdot 10^{-19} \,\mathrm{C}$
e^-	electron	

E	particle energy	
E_b	energy content of the drive bunch	
E_{in}	initial energy	
E_{min}	minimum energy	
E_{WB}	non-relativistic cold wave-braking field	
E_r	radial electric field	
E_z	longitudinal wakefield	
f	frequency	
f_{mod}	frequency of the bunch density modulation	
f_{pe}	cold plasma electron frequency	
FCC	Future Circular Collied	
FEL	Free Electron Laser	
γ	Lorentz factor	
Γ	SM growth rate	
g	plasma density gradient	
I_0	zeroth order modified Bessel function of the first kind	
IS	Imaging Station	
k_B	Boltzmann constant	$k_B = 1.381 \cdot 10^{-23}\,\mathrm{J/K}$
k_{pe}	plasma electron wave number	
K_0	zeroth order modified Bessel function of the second kind	
K_β	strength of the self-focusing force	
λ_β	beam betatron wavelength	
λ_D	Debye length	
λ_{pe}	plasma electron wavelength	
L	collider luminosity	
L_{bunch}	square bunch length	
LBNL	Lawrence Berkley National Laboratory	
LCLS	Linac Coherent Light Source	

LEP	Large Electron-Positron Collider	
LINAC	Linear Accelerator	
LHC	Large Hadron Collider	
LWFA	Laser Wakefield Acceleration	
μ_E	highest peak energy of accelerated electrons	
m_e	electron rest mass	$m_e = 9.109 \cdot 10^{-31}\,\mathrm{kg}$
m_i	plasma ion mass	
m_0	particle rest mass	
m_p	proton rest mass	$m_p = 1.6 \cdot 10^{-27}\,\mathrm{kg}$
n_b	initial bunch density	
$n_{b,0}$	bunch peak density	
n_{pe}	plasma electron density	
n_{vap}	Rubidium vapor density	
N_D	number of particles in a Debye sphere	
ω	angular frequency	
ω_{pe}	plasma electron angular frequency	
ω_{pi}	plasma ion angular frequency	
OTR	optical transition radiation	
p^+	proton	
$p_\perp$	transverse momentum	
P	number of zero-padding arrays	
PIC	Particle-in-cell	
PWFA	Plasma Wakefield Acceleration	
Q_e	electron bunch charge	
Q_p	proton bunch charge	
ρ	bending radius of a particle in the magnetic field B	
r_e	classical electron radius	$r_e = 2.8 \cdot 10^{-15}\,\mathrm{m}$

R	geometrical factor of the wakefields
$R_{x,y}$	Larmor radii
R&D	research and development
Rb	Rubidium
RF	radio-frequency
RIF	relativistic ionization front
rms	root mean square
$\sigma_{r,x,y}$	bunch width in r, x, y
σ_t	bunch duration
SLC	Stanford Linear Collider
SM	Self-Modulation
SMI	Self-Modulation Instability
SPS	Super Proton Synchrotron
Θ	Heaviside function
t	time in the bunch frame
t_p, t_{RIF}	time interval between RIF and p^+ bunch center
t_{seed}	time interval between e^- and p^+ bunch center
T_c	mean time between collisions in plasma
T_e	plasma electron temperature
T_{pe}	plasma electron period
T_{mod}	period the modulation
UV	ultra-violet
v_w	velocity of the witness bunch
w	transverse extent of the proton bunch
w_{off}	transverse extent of the proton bunch without plasma
$W_\perp$	transverse wakefields
$W_{\perp 0}$	seed wakefields

| ξ | spatial coordinate in the co-moving bunch frame |
| φ | SM phase |

Bibliography

[1] "Luminosity determination in pp collisions at $\sqrt{s} = 13$ TeV using the AT-LAS detector at the LHC," June 2019.

[2] P. Jenni and T. S. Virdee, *The Discovery of the Higgs Boson at the LHC*, pp. 263–309. Cham: Springer International Publishing, 2020.

[3] K. Wille and J. McFall, *The Physics of Particle Accelerators: An Introduction*. The Physics of Particle Accelerators: An Introduction, Oxford University Press, 2000.

[4] J. T. Seeman, "The Stanford Linear Collider," *Proceedings of the Linear Accelerator Conference 1990, Albuquerque, New Mexico, USA*, 1990.

[5] J. M. J. Madey, "Stimulated emission of bremsstrahlung in a periodic magnetic field," *Journal of Applied Physics*, vol. 42, no. 5, pp. 1906–1913, 1971.

[6] E. Schneidmiller and M. Yurkov, "Baseline Parameters of the European XFEL," in *38th International Free-Electron Laser Conference*, 2018.

[7] A. Abada, M. Abbrescia, S.S. AbdusSalam et al., "FCC-hh: The Hadron Collider," *The European Physical Journal Special Topics*, vol. 228, no. 4.

[8] A. Abada, M. Abbrescia, S.S. AbdusSalam et al., "Fcc-ee: The lepton collider," *The European Physical Journal Special Topics*, vol. 228, no. 2, pp. 261–623, 2019.

[9] M. Aiba, B. Goddard, K. Oide, Y. Papaphilippou, Saá Hernández, D. Shwartz, S. White, and F. Zimmermann, "Top-up injection schemes for

future circular lepton collider," *Nuclear Instruments and Methods in Physics Research Section A: Accelerators, Spectrometers, Detectors and Associated Equipment*, vol. 880, pp. 98–106, 2018.

[10] M. Aicheler et al., "A Multi-TeV Linear Collider Based on CLIC Technology: CLIC Conceptual Design Report," 2012.

[11] Aihara, Hiroaki et al., "The International Linear Collider. A Global Project," tech. rep., Jan 2019.

[12] M. Tigner, "Does accelerator-based particle physics have a future?," *Physics Today*, vol. 54, no. 1, pp. 36–40, 2001.

[13] N. A. Solyak, "Gradient limitations in room temperature and superconducting acceleration structures," *AIP Conference Proceedings*, vol. 1086, no. 1, pp. 365–372, 2009.

[14] F. F. Chen, "Excitation of large amplitude plasma waves," *Physica Scripta*, vol. T30, pp. 14–23, jan 1990.

[15] T. Tajima and J. M. Dawson, "Laser electron accelerator," *Phys. Rev. Lett.*, vol. 43, pp. 267–270, Jul 1979.

[16] P. Chen et al., "Acceleration of electrons by the interaction of a bunched electron beam with a plasma," *Phys. Rev. Lett.*, vol. 54, pp. 693–696, Feb 1985.

[17] R. Keinigs and M. E. Jones, "Two-dimensional dynamics of the plasma wakefield accelerator," *The Physics of Fluids*, vol. 30, no. 1, pp. 252–263, 1987.

[18] P. Muggli, "Beam-driven systems, plasma wakefield acceleration," 2020.

[19] C. Clayton et al., "Ultrahigh-gradient acceleration of injected electrons by laser-excited relativistic electron plasma waves," *Phys. Rev. Lett.*, vol. 70, pp. 37–40, Jan 1993.

[20] D. Strickland and G. Mourou, "Compression of amplified chirped optical pulses," *Optics Communications*, vol. 56, no. 3, pp. 219–221, 1985.

[21] C. G. R. Geddes et al., "High-quality electron beams from a laser wake-field accelerator using plasma-channel guiding," *Nature*, vol. 431, no. 7008, pp. 538–541, 2004.

[22] S. P. D. Mangles et al., "Monoenergetic beams of relativistic electrons from intense laser–plasma interactions," *Nature*, vol. 431, no. 7008, pp. 535–538, 2004.

[23] J. Faure et al., "A laser–plasma accelerator producing monoenergetic electron beams," *Nature*, vol. 431, no. 7008, pp. 541–544, 2004.

[24] W. P. Leemans et al., "Multi-gev electron beams from capillary-discharge-guided subpetawatt laser pulses in the self-trapping regime," *Phys. Rev. Lett.*, vol. 113, p. 245002, Dec 2014.

[25] A. J. Gonsalves et al., "Petawatt laser guiding and electron beam acceleration to 8 gev in a laser-heated capillary discharge waveguide," *Phys. Rev. Lett.*, vol. 122, p. 084801, Feb 2019.

[26] S. Steinke et al., "Staging of laser-plasma accelerators," *Physics of Plasmas*, vol. 23, no. 5, p. 056705, 2016.

[27] J. van Tilborg et al., "Active plasma lensing for relativistic laser-plasma-accelerated electron beams," *Phys. Rev. Lett.*, vol. 115, p. 184802, Oct 2015.

[28] M. Kirchen et al., "Optimal beam loading in a laser-plasma accelerator," *Phys. Rev. Lett.*, vol. 126, p. 174801, Apr 2021.

[29] S. Jalas et al., "Bayesian optimization of a laser-plasma accelerator," *Phys. Rev. Lett.*, vol. 126, p. 104801, Mar 2021.

[30] W. Wang, K. Feng, L. Ke et al., "Free-electron lasing at 27 nanometres based on a laser wakefield accelerator," *Nature*, vol. 595, 2021.

[31] J. B. Rosenzweig et al., "Experimental observation of plasma wake-field acceleration," *Phys. Rev. Lett.*, vol. 61, pp. 98–101, Jul 1988.

[32] I. Blumenfeld et al., "Energy doubling of 42 gev electrons in a metre-scale plasma wakefield accelerator," *Nature*, vol. 445, no. 7129, pp. 741–744, 2007.

[33] E. Kallos et al., "High-gradient plasma-wakefield acceleration with two sub-picosecond electron bunches," *Phys. Rev. Lett.*, vol. 100, p. 074802, Feb 2008.

[34] M. Litos et al., "High-efficiency acceleration of an electron beam in a plasma wakefield accelerator," *Nature*, vol. 515, no. 7525, pp. 92–95, 2014.

[35] N. Vafaei-Najafabadi et al., "Beam loading by distributed injection of electrons in a plasma wakefield accelerator," *Phys. Rev. Lett.*, vol. 112, p. 025001, Jan 2014.

[36] C. A. Lindstrøm et al., "Energy-spread preservation and high efficiency in a plasma-wakefield accelerator," *Phys. Rev. Lett.*, vol. 126, p. 014801, Jan 2021.

[37] S. Schröder et al., "High-resolution sampling of beam-driven plasma wakefields," *Nature Communications*, vol. 11, no. 1, p. 5984, 2020.

[38] R. Pompili et al., "Energy spread minimization in a beam-driven plasma wakefield accelerator," *Nature Physics*, vol. 17, no. 4, pp. 499–503, 2021.

[39] V. Shpakov et al., "First emittance measurement of the beam-driven plasma wakefield accelerated electron beam," *Phys. Rev. Accel. Beams*, vol. 24, p. 051301, May 2021.

[40] R. Pompili et al, "First lasing of a free-electron laser with a compact beam-driven plasma accelerator," *submitted to Nature*, 2021.

[41] R. W. Assmann et al., "Eupraxia conceptual design report," *The European Physical Journal Special Topics*, vol. 229, no. 24, pp. 3675–4284, 2020.

[42] A. Caldwell, K. Lotov, A. Pukhov, and F. Simon, "Proton-driven plasma-wakefield acceleration," *Nature Physics*, vol. 5, no. 5, pp. 363–367, 2009.

[43] K. V. Lotov, "Simulation of proton driven plasma wakefield acceleration," *Phys. Rev. ST Accel. Beams*, vol. 13, p. 041301, Apr 2010.

[44] AWAKE Collaboraion, "Acceleration of electrons in the plasma wakefield of a proton bunch," *Nature*, vol. 561, no. 7723, pp. 363–367, 2018.

[45] E. Gschwendtner et al., "AWAKE, The Advanced Proton Driven Plasma Wakefield Acceleration Experiment at CERN," *Nuclear Instruments and Methods in Physics Research Section A: Accelerators, Spectrometers, Detectors and Associated Equipment*, vol. 829, pp. 76–82, 2016. 2nd European Advanced Accelerator Concepts Workshop - EAAC 2015.

[46] D. T. Farley, "Two-stream plasma instability as a source of irregularities in the ionosphere," *Phys. Rev. Lett.*, vol. 10, pp. 279–282, Apr 1963.

[47] O. Buneman, "Excitation of field aligned sound waves by electron streams," *Phys. Rev. Lett.*, vol. 10, pp. 285–287, Apr 1963.

[48] N. Kumar et al., "Self-modulation instability of a long proton bunch in plasmas," *Phys. Rev. Lett.*, vol. 104, p. 255003, Jun 2010.

[49] P Muggli et al. (AWAKE Collaboration), "AWAKE readiness for the study of the seeded self-modulation of a 400 GeV proton bunch," *Plasma Physics and Controlled Fusion*, vol. 60, p. 014046, nov 2017.

[50] AWAKE Collaboration, "Experimental observation of proton bunch modulation in a plasma at varying plasma densities," *Phys. Rev. Lett.*, vol. 122, p. 054802, Feb 2019.

[51] M. Turner et al. (AWAKE Collaboration), "Experimental observation of plasma wakefield growth driven by the seeded self-modulation of a proton bunch," *Phys. Rev. Lett.*, vol. 122, p. 054801, Feb 2019.

[52] F. Batsch, P. Muggli et al. (AWAKE Collaboration), "Transition between instability and seeded self-modulation of a relativistic particle bunch in plasma," *Phys. Rev. Lett.*, vol. 126, p. 164802, Apr 2021.

[53] G. Demeter, et al., "Long-range propagation of ultrafast ionizing laser pulses in a resonant nonlinear medium," *Phys. Rev. A*, vol. 104, p. 033506, Sep 2021.

[54] L. Verra, E. Gschwendtner and P. Muggli, "Study of external electron beam injection into proton driven plasma wakefields for AWAKE run2," *Journal of Physics: Conference Series*, vol. 1596, p. 012007, jul 2020.

[55] A. Pukhov et al., "Phase velocity and particle injection in a self-modulated proton-driven plasma wakefield accelerator," *Phys. Rev. Lett.*, vol. 107, p. 145003, Sep 2011.

[56] C. Schroeder et al., "Growth and phase velocity of self-modulated beam-driven plasma waves," *Phys. Rev. Lett.*, vol. 107, p. 145002, Sep 2011.

[57] F. Braunmüller et al. (AWAKE Collaboration), "Proton bunch self-modulation in plasma with density gradient," *Phys. Rev. Lett.*, vol. 125, p. 264801, Dec 2020.

[58] P. Muggli, "Physics to plan AWAKE run 2," *Journal of Physics: Conference Series*, vol. 1596, p. 012008, jul 2020.

[59] A. Caldwell and K. V. Lotov, "Plasma wakefield acceleration with a modulated proton bunch," *Physics of Plasmas*, vol. 18, no. 10, p. 103101, 2011.

[60] W. Lu, C. Huang, M. Zhou, W. B. Mori, and T. Katsouleas, "Nonlinear theory for relativistic plasma wakefields in the blowout regime," *Phys. Rev. Lett.*, vol. 96, p. 165002, Apr 2006.

[61] T. C. Katsouleas, S. Wilks, P. Chen, J. M. Dawson, and J. J. Su, "Beam Loading in Plasma Accelerators," *Part. Accel.*, vol. 22, pp. 81–99, 1987.

[62] V. K. Olsen et al., "Emittance preservation of an electron beam in a loaded quasilinear plasma wakefield," *Phys. Rev. Accel. Beams*, vol. 21, p. 011301, Jan 2018.

[63] N. Arkani-Hamed et al., "A theory of dark matter," *Phys. Rev. D*, vol. 79, p. 015014, Jan 2009.

[64] E. Gschwendtner, K. Lotov, P. Muggli, M. Wing et al. (AWAKE Collaboration), "The AWAKE Run 2 programme and beyond," *Submitted to Symmetry*, 2022.

[65] S. N. Gninenko, "Search for MeV dark photons in a light-shining-through-walls experiment at CERN," *Phys. Rev. D*, vol. 89, p. 075008, Apr 2014.

[66] A. Caldwell and M. Wing, "Vheep: a very high energy electron–proton collider," *The European Physical Journal C*, vol. 76, no. 8, p. 463, 2016.

[67] F. F. Chen, *Introduction to Plasma Physics and Controlled Fusion*. Springer International Publishing, 2016.

[68] V. S. Popov, "Tunnel and multiphoton ionization of atoms and ions in a strong laser field (keldysh theory)," *Physics-Uspekhi*, vol. 47, pp. 855–885, sep 2004.

[69] J. T. Moody et al., "Multi Keldysh regime resonant ionizing laser pulse propagation through a ten meter Rubidium vapor source at AWAKE," *COFIL, Geneva, Switzerland*, 2018.

[70] B. Allen et al., "Experimental study of current filamentation instability," *Phys. Rev. Lett.*, vol. 109, p. 185007, Nov 2012.

[71] J. Vieira et al., "Transverse self-modulation of ultra-relativistic lepton beams in the plasma wakefield accelerator," *Physics of Plasmas*, vol. 19, no. 6, p. 063105, 2012.

[72] K.V. Lotov et al., "Natural noise and external wakefield seeding in a proton-driven plasma accelerator," *Phys. Rev. ST Accel. Beams*, vol. 16, p. 041301, Apr 2013.

[73] Y. Fang, "Resonant excitation of plasma wakefield," *PhD Thesis, University of Southern California*, 2014.

[74] A.-M. Bachmann, "Self-Modulation Development of a Proton Bunch in Plasma," *PhD thesis, Technical University Munich, CERN-THESIS-2021-094*, 2021.

[75] F. Batsch et al., "Interferometer-based high-accuracy white light measurement of neutral rubidium density and gradient at awake," *Nuclear Instruments and Methods in Physics Research Section A: Accelerators, Spectrometers, Detectors and Associated Equipment*, vol. 909, pp. 359–363, 2018. 3rd European Advanced Accelerator Concepts workshop (EAAC2017).

[76] K. Pepitone et al., "The electron accelerators for the awake experiment at cern—baseline and future developments," *Nuclear Instruments and Methods in Physics Research Section A: Accelerators, Spectrometers, Detectors and Associated Equipment*, vol. 909, pp. 102–106, 2018. 3rd European Advanced Accelerator Concepts workshop (EAAC2017).

[77] J. S. Schmidt et al., "The AWAKE Electron Primary Beam Line," pp. 2584–2586, June 2015. https://doi.org/10.18429/JACoW-IPAC2015-WEPWA039.

[78] I. Gorgisyan et al., "Commissioning of beam instrumentation at the CERN AWAKE facility after integration of the electron beam line," *Journal of Physics: Conference Series*, vol. 1067, p. 072015, sep 2018.

[79] K. T. McDonald and D. P. Russell, *Methods of emittance measurement.* Springer Berlin Heidelberg, 1989.

[80] M. Turner et al., "External electron injection for the awake experiment," pp. 1–4, 2018.

[81] L. Verra et al., "Electron beam characterization with beam loss monitors," *Phys. Rev. Accel. Beams*, vol. 23, p. 032803, Mar 2020.

[82] L. Verra, "Electron beam measurements with beam loss monitors in awake," *Master Thesis, University of Milan, CERN-THESIS-2019-003*, 2019.

[83] S. Liu et al., "The Installation and Commissioning of the AWAKE Stripline BPM," pp. 253–256, Jan. 2019. https://doi.org/10.18429/JACoW-IBIC2018-TUPB01.

[84] S. Mazzoni et al., "Beam Instrumentation Developments for the Advanced Proton Driven Plasma Wakefield Acceleration Experiment at CERN," pp. 404–407, May 2017. https://doi.org/10.18429/JACoW-IPAC2017-MOPAB119.

[85] K. Rieger et al., "GHz modulation detection using a streak camera: Suitability of streak cameras in the AWAKE experiment," *Review of Scientific Instruments*, vol. 88, no. 2, p. 025110, 2017.

[86] "https://www.hamamatsu.com,"

[87] F. Keeble et al., "The AWAKE Electron Spectrometer," pp. 4947–4950, June 2018. https://doi.org/10.18429/JACoW-IPAC2018-THPML118.

[88] J. Bauche et al., "A magnetic spectrometer to measure electron bunches accelerated at awake," *Nuclear Instruments and Methods in Physics Research Section A: Accelerators, Spectrometers, Detectors and Associated Equipment*, vol. 940, pp. 103–108, 2019.

[89] M. Turner et al., "The two-screen measurement setup to indirectly measure proton beam self-modulation in awake," *Nuclear Instruments and Methods in Physics Research Section A: Accelerators, Spectrometers, Detectors and Associated Equipment*, vol. 854, pp. 100–106, 2017.

[90] F. Batsch, "Setup and characteristics of a timing reference signal with sub-ps accuracy for AWAKE," *Journal of Physics: Conference Series*, vol. 1596, p. 012006, jul 2020.

[91] M. Turner, P. Muggli et al. (AWAKE Collaboration), "Experimental study of wakefields driven by a self-modulating proton bunch in plasma," *Phys. Rev. Accel. Beams*, vol. 23, p. 081302, Aug 2020.

[92] V. Hafych, A. Caldwell et al. (AWAKE Collaboration), "Analysis of proton bunch parameters in the AWAKE experiment," *Journal of Instrumentation*, vol. 16, p. P11031, nov 2021.

[93] O. E. Berrig et al., "CERN-SPS Wire Scanner Impedance and Wire Heating Studies," Sep 2014.

[94] G. Baud et al., "Performance Assessment of Wire-Scanners at CERN," p. 4 p, Sep 2013.

[95] Y. Fang et al., "Seeding of self-modulation instability of a long electron bunch in a plasma," *Phys. Rev. Lett.*, vol. 112, p. 045001, Jan 2014.

[96] F. Braunmueller et al., "Novel diagnostic for precise measurement of the modulation frequency of seeded self-modulation via coherent transition radiation in awake," *Nuclear Instruments and Methods in Physics Research Section A: Accelerators, Spectrometers, Detectors and Associated Equipment*, vol. 909, pp. 76–79, 2018. 3rd European Advanced Accelerator Concepts workshop (EAAC2017).

[97] K. V. Lotov, "Radial equilibrium of relativistic particle bunches in plasma wakefield accelerators," *Physics of Plasmas*, vol. 24, no. 2, p. 023119, 2017.

[98] K.-J. Moon et al., "Numerical Study of Electron Bunch Seeded Proton Bunch Self-Modulation," *47th EPS Conference on Plasma Physics*, 2021.

[99] R. Lehe et al., "A spectral, quasi-cylindrical and dispersion-free particle-in-cell algorithm," *Computer Physics Communications*, vol. 203, pp. 66–82, 2016.

[100] K. L. F. Bane et al., "Wake fields and wake field acceleration," *AIP Conference Proceedings*, vol. 127, no. 1, pp. 875–928, 1985.

[101] P. Chen et al., "Plasma-based adiabatic focuser," *Phys. Rev. Lett.*, vol. 64, pp. 1231–1234, Mar 1990.

[102] G. Hairapetian et al., "Experimental demonstration of dynamic focusing of a relativistic electron bunch by an overdense plasma lens," *Phys. Rev. Lett.*, vol. 72, pp. 2403–2406, Apr 1994.

[103] J. S. T. Ng et al., "Observation of plasma focusing of a 28.5 gev positron beam," *Phys. Rev. Lett.*, vol. 87, p. 244801, Nov 2001.

[104] D. Whittum et al., "Electron-hose instability in the ion-focused regime," *Phys. Rev. Lett.*, vol. 67, pp. 991–994, Aug 1991.

[105] K. V. Lotov and P. V. Tuev, "Plasma wakefield acceleration beyond the dephasing limit with 400 GeV proton driver," *Plasma Physics and Controlled Fusion*, vol. 63, p. 125027, nov 2021.

[106] M. Lampe et al., "Electron-hose instability of a relativistic electron beam in an ion-focusing channel," *Physics of Fluids B: Plasma Physics*, vol. 5, no. 6, pp. 1888–1901, 1993.

[107] A. A. Geraci and D. H. Whittum, "Transverse dynamics of a relativistic electron beam in an underdense plasma channel," *Physics of Plasmas*, vol. 7, no. 8, pp. 3431–3440, 2000.

[108] M. Hüter, "Direct observation of the hosing instability of a long relativistic proton bunch in the awake experiment," *PhD thesis, Technical University Munich*, 2020.

Acknowledgments

During one of the first weeks of my PhD, I was in the cafeteria with my advisor, Patric Muggli. While I was trying to present some ideas, he interrupted me abruptly saying: "You have to be careful and speak precisely". Since then, this has been my constant endeavour. I want to profoundly thank him for being a real mentor in these years, guiding me on every aspect of my growth as a scientist. Above all, for teaching me with the example the intellectual honesty needed to admit that a measurement is wrong or that the results are unclear. This work stands as my uttermost attempt of precision and honesty.

Thanks to Edda Gschwendtner for offering me the outstanding opportunity of carrying out my PhD at CERN. Thanks for the trust she has always given me, and for the one granted for the next years.

Thanks to my University Professor, Allen Caldwell, for the support and supervision.

Thanks to Giovanni Zevi Della Porta for the countless hours in the control room working with me on the electron beamline. Thanks for the almost as many capzises on the catamaran and for taking some of the final data when I was racing a triathlon or when I was too tired to align the beam one more time.

This is the result of a choral effort, and it could have not been possible without the contribution of many people in the AWAKE team. Among them, I want to thank Michele Bergamaschi, Kook-Jin Moon and Joshua T. Moody for their help and contribution.

I believe that a big part of a PhD is understanding what it actually is. Thanks to Dr. Anna-Maria Bachmann for sharing with me her path of discovery. Thanks

for paving the way and for leaving behind this beautiful research topic. And most importantly, thanks for being a real friend.

Thanks to Marlene Turner, with whom I miss working very much, for setting me on the right trajectory in my early days in the experiment.

Thanks to Lucia for always being there and for reminding me what are the cardinal points to aim for in a life.

Thanks to Nicolò and Simone for being the friends I deserve.

Thanks to *La Zanzara*, ungodly radio show that, any given day, makes me laugh and reminds me that there are more things in heaven and earth than are dreamt of in my mind.

Thanks to my whole family for the discreet support. To my dad for always wanting more from me. To my mum for loving me no matter what. To my sister for wanting me different. To Roberto for accepting all of us as we are.

Dear Marta, if I have arrived at the end of this journey holding myself together, it is only thanks to you. Thank you for being my Polar Star in the nights of frustration and of joy. I found you while going to the most beautiful place in the world; since then, the most beautiful place is anywhere I am with you.

Ringraziamenti

Durante una delle prime settimane del mio dottorato, ero in caffetteria con il mio advisor, Patric Muggli. Mentre cercavo di esporre una qualche idea, lui mi interruppe bruscamente dicendo: "Devi fare attenzione e parlare precisamente." Da allora, questo è stato il mio costante impegno. Voglio ringraziarlo per essere stato un vero maestro in questi anni, guidandomi in ogni aspetto della mia crescita come ricercatore. Soprattutto, per avermi insegnato con l'esempio l'onestà intellettuale necessaria per ammettere che una misura è sbagliata o che i risultati sono incerti. Questo lavoro è il mio estremo tentativo di precisione ed onestà.

Grazie a Edda Gschwendtner per avermi offerto la straordinaria opportunità di svolgere il mio dottorato al CERN. Grazie per la fiducia che mi ha sempre concesso, e per quella accordata per i prossimi anni.

Grazie al mio Professore universitario, Allen Caldwell, per aver sostenuto questo lavoro.

Grazie a Giovanni Zevi Della Porta per le innumerevoli ore in control room a lavorare con me sulla beamline. Grazie per le quasi altrettante scuffie in catamarano e per aver preso alcuni dei dati finali mentre ero a gareggiare in un triathlon o ero troppo stanco per allineare il fascio ancora una volta.

Questo è il risultato di uno sforzo corale, e non sarebbe stato possibile senza il contributo di molte persone nell'AWAKE team. Tra loro, vorrei ringraziare Michele Bergamaschi, Kook-Jin Moon e Joshua T. Moody per il loro aiuto e contributo.

Credo che buona parte di un dottorato sia capire che cos'è. Grazie a Dr. Anna-Maria Bachmann per aver condiviso con me il proprio percorso di scoperta. Grazie

per aver battuto la via e per avermi lasciato questo magnifico argomento di ricerca. Ma soprattutto, grazie per essere una vera amica.

Grazie a Marlene Turner, con cui mi manca molto lavorare, per avermi messo sulla giusta traiettoria nei miei primi tempi nell'esperimento.
Grazie a Lucia per esserci sempre e per ricordarmi quali sono i punti cardine della vita a cui aspirare.

Grazie a Nicolò e Simone per essere gli amici che mi merito.

Grazie a *La Zanzara*, disgraziata trasmissione radiofonica che ogni giorno mi fa ridere e ricordare che esistono più cose in cielo e in terra che nel mio pensiero.

Grazie a tutta la mia famiglia per il sostegno discreto. A mio papà per aver sempre voluto da me qualcosa in più. A mia mamma per volermi bene sempre e comunque. A mia sorella per volermi diverso. A Roberto per accettarci tutti così come siamo.

Cara Marta, se sono arrivato in fondo a questo percorso tenendo insieme i pezzi, è solo grazie a te. Grazie per essere la mia Stella Polare nelle notti di frustrazione e di gioia. Ti ho trovata andando nel luogo più bello del mondo; da allora, il luogo più bello è ovunque io sia con te.

Appendix

Controlled Growth of the Self-Modulation of a Relativistic Proton Bunch in Plasma

L. Verra,[1, 2, 3, *] G. Zevi Della Porta,[1] J. Pucek,[2, 3] T. Nechaeva,[2, 3] S. Wyler,[4] M. Bergamaschi,[2]
E. Senes,[1] E. Guran,[1] J.T. Moody,[2] M.Á. Kedves,[5] E. Gschwendtner,[1] and P. Muggli[2]

(AWAKE Collaboration)

R. Agnello,[4] C.C. Ahdida,[1] M.C.A. Goncalves,[1] Y. Andrebe,[4] O. Apsimon,[6, 7] R. Apsimon,[7, 8] J.M. Arnesano,[1]
A.-M. Bachmann,[2] D. Barrientos,[1] F. Batsch,[2] V. Bencini,[1, 9] P. Blanchard,[4] P.N. Burrows,[9] B. Buttenschön,[10]
A. Caldwell,[2] J. Chappell,[11] E. Chevallay,[1] M. Chung,[12] D.A. Cooke,[11] C. Davut,[7, 13] G. Demeter,[5] A.C. Dexter,[7, 8]
S. Doebert,[1] F.A. Elverson,[1] J. Farmer,[1, 2] A. Fasoli,[4] V. Fedosseev,[1] R. Fonseca,[14, 15] I. Furno,[4] A. Gorn,[16, 17]
E. Granados,[1] M. Granetzny,[18] T. Graubner,[19] O. Grulke,[10, 20] V. Hafych,[2] J. Henderson,[7, 21] M. Hüther,[2]
V. Khudiakov,[22, 16] S.-Y. Kim,[12, 1] F. Kraus,[19] M. Krupa,[1] T. Lefevre,[1] L. Liang,[7, 13] S. Liu,[23] N. Lopes,[15]
K. Lotov,[16, 17] M. Martinez Calderon,[1] S. Mazzoni,[1] D. Medina Godoy,[1] K. Moon,[12] P.I. Morales Guzmán,[2]
M. Moreira,[15] E. Nowak,[1] C. Pakuza,[9] H. Panuganti,[1] A. Pardons,[1] K. Pepitone,[24] A. Perera,[7, 6] A. Pukhov,[22]
R.L. Ramjiawan,[1, 9] S. Rey,[1] O. Schmitz,[18] F. Silva,[25] L. Silva,[15] C. Stollberg,[4] A. Sublet,[1] C. Swain,[7, 6]
A. Topaloudis,[1] N. Torrado,[15] P. Tuev,[16, 17] F. Velotti,[1] V. Verzilov,[23] J. Vieira,[15] M. Weidl,[26] C. Welsch,[7, 6]
M. Wendt,[1] M. Wing,[11] J. Wolfenden,[7, 6] B. Woolley,[1] G. Xia,[7, 13] V. Yarygova,[16, 17] and M. Zepp[18]

[1] *CERN, Geneva, Switzerland*
[2] *Max Planck Institute for Physics, Munich, Germany*
[3] *Technical University Munich, Munich, Germany*
[4] *Ecole Polytechnique Federale de Lausanne (EPFL),*
Swiss Plasma Center (SPC), Lausanne, Switzerland
[5] *Wigner Research Centre for Physics, Budapest, Hungary*
[6] *University of Liverpool, Liverpool, UK*
[7] *Cockcroft Institute, Daresbury, UK*
[8] *Lancaster University, Lancaster, UK*
[9] *John Adams Institute, Oxford University, Oxford, UK*
[10] *Max Planck Institute for Plasma Physics, Greifswald, Germany*
[11] *UCL, London, UK*
[12] *UNIST, Ulsan, Republic of Korea*
[13] *University of Manchester, Manchester, UK*
[14] *ISCTE - Instituto Universitéario de Lisboa, Portugal*
[15] *GoLP/Instituto de Plasmas e Fusão Nuclear, Instituto Superior Técnico, Universidade de Lisboa, Lisbon, Portugal*
[16] *Budker Institute of Nuclear Physics SB RAS, Novosibirsk, Russia*
[17] *Novosibirsk State University, Novosibirsk, Russia*
[18] *University of Wisconsin, Madison, Wisconsin, USA*
[19] *Philipps-Universität Marburg, Marburg, Germany*
[20] *Technical University of Denmark, Lyngby, Denmark*
[21] *Accelerator Science and Technology Centre, ASTeC, STFC Daresbury Laboratory, Warrington, UK*
[22] *Heinrich-Heine-Universität Düsseldorf, Düsseldorf, Germany*
[23] *TRIUMF, Vancouver, Canada*
[24] *Angstrom Laboratory, Department of Physics and Astronomy, Uppsala, Sweden*
[25] *INESC-ID, Instituto Superior Técnico, Universidade de Lisboa, Lisbon, Portugal*
[26] *Max Planck Institute for Plasma Physics, Munich, Germany*

(Dated: March 25, 2022)

A long, narrow, relativistic charged particle bunch propagating in plasma is subject to the self-modulation (SM) instability. We show that SM of a proton bunch can be seeded by the wakefields driven by a preceding electron bunch. SM timing reproducibility and control are at the level of a small fraction of the modulation period. With this seeding method, we independently control the amplitude of the seed wakefields with the charge of the electron bunch and the growth rate of SM with the charge of the proton bunch. Seeding leads to larger growth of the wakefields than in the instability case.

Introduction.— Instabilities are of paramount importance in plasma physics [1]. Similar instabilities occur in vastly different plasmas, from astrophysical [2, 3], to laboratory [4] and fusion [5], to quantum [6] and even to quark-gluon plasmas [7]. They can be disruptive and must then be suppressed, or beneficial and must then be controlled. Charged particle beams propagating in plasma are subject to a number of instabilities, including

different occurrences of the two-stream instability [8, 9]. In the case of a long, narrow, relativistic charged particle bunch, the instability is transverse and it is called the self-modulation instability (SMI) [10].

Relativistic charged particle bunches traveling in plasma leave behind a perturbation in the plasma electron density. This perturbation provides a restoring force that induces an oscillation of the plasma electrons with angular frequency $\omega_{pe} = \sqrt{\frac{n_{pe}e^2}{m_e \varepsilon_0}}$, where n_{pe} is the plasma electron density, e and m_e are the electron charge and mass, ε_0 is the vacuum permittivity. The local charge non-neutrality sustains fields with transverse and longitudinal components, known as wakefields, that can have amplitudes appealing for high-gradient particle acceleration [11, 12].

SMI [10] develops when the bunch duration is much longer than the period of the wakefields: $\sigma_t \gg T_{pe} = 2\pi/\omega_{pe}$. Transverse wakefields act back on the bunch, modulating its radius and thus its charge density. The modulated distribution drives enhanced wakefields, causing the growth of SMI that, at saturation, leaves the long bunch fully modulated into a train of microbunches with periodicity $\sim T_{pe}$. The timing of the microbunches along the train is tied to that of the wakefields since microbunches develop in their focusing phase.

When a long proton (p^+) bunch enters a pre-ionized plasma, SMI develops from the wakefields driven by noise [13] or by imperfections in the incoming bunch charge distribution [14]. Thus, the initial conditions vary from event to event and so do the timing and amplitude of the wakefields. However, the outcome can be controlled by seeding the instability, i.e., by fixing the initial conditions from which the instability grows.

Seeding requires driving initial transverse wakefields with amplitude larger than those driven by the noise or imperfections in the bunch so that the self-modulation (SM) develops from a well-defined time, and with well-defined initial amplitude and growth rate. We demonstrated experimentally that a high-energy, long p^+ bunch undergoes SMI when traveling in plasma [15], and that the resulting microbunch train resonantly excites large amplitude wakefields [16, 17]. A relativistic ionization front (RIF) generating the plasma and co-propagating within the p^+ bunch can provide the seed by the rapid onset of the beam-plasma interaction [14]. In this case, the amplitude of the seed wakefields and the growth rate of SM depend on the p^+ bunch density at the RIF and cannot be varied independently. Moreover, the front of the bunch propagates as if in vacuum and thus remains unmodulated.

The initial transverse seed wakefields can also be provided by a preceding charged particle bunch [18, 19]. In this case, seeding amplitude and growth rate of SM can be varied independently. Moreover, as the seed wakefields act on the whole p^+ bunch, the entire bunch self-modulates.

The protons that are defocused out of the wakefields are probes for the amplitude of the wakefields at early distances along plasma, during SM growth, before saturation [16, 20]. Theoretical and numerical simulation results [10, 21–23] show that, in the linear regime, the amplitude of the transverse wakefields along the bunch (t) and along the plasma (z) grows as $W_\perp(t, z) = W_{\perp 0} \exp\left(\Gamma(t, z)z\right)$. In the case of seeding with an electron (e^-) bunch, the amplitude of the initial wakefields $W_{\perp 0}(z = 0)$ depends solely on the e^- bunch parameters, while the growth rate of SM $\Gamma(t, z)$ depends solely on those of the p^+ bunch. The radial extent reached by defocused protons a distance downstream of the plasma is proportional to the transverse momentum they acquire from these wakefields, and therefore increases with the growth of SM.

In this *Letter*, we demonstrate with experimental results that SM of a long, relativistic p^+ bunch in plasma can be seeded by a preceding e^- bunch. We show that the growth of SM increases when increasing the charge of the seed e^- bunch Q_e or the charge of the p^+ bunch Q_p. We attribute these changes to a change in the amplitude of the transverse seed wakefields $W_{\perp 0}(Q_e)$ or in the SM growth rate $\Gamma(Q_p)$. These observations are possible because the e^- bunch effectively seeds SM and they are in agreement with theoretical and simulation predictions [10, 21, 23, 24]. When seeding, the growth of the process is larger than in the SMI case [10]. We also observe adiabatic focusing of the front of the p^+ bunch, where the growth of SM is small. In addition, e^- bunch seeding allows for the timing of the process to be controlled at the sub-modulation-period, picosecond time scale.
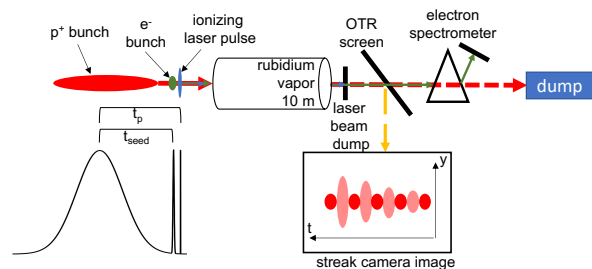

FIG. 1. Schematic of the experimental setup: the ionizing laser pulse enters the vapor source t_p ahead of the p^+ bunch center and ionizes the rubidium atoms, creating the plasma. The seed e^- bunch follows, t_{seed} ahead of the p^+ bunch. The optical transition radiation produced at a screen positioned 3.5 m downstream of the plasma exit is imaged on the entrance slit of a streak camera. A schematic example of a time-resolved image of the self-modulated p^+ bunch provided by the streak camera is shown in the inset. The magnetic spectrometer is located downstream of the screen.

Experimental Setup.— The measurements took place

in the context of the AWAKE experiment [25], whose goal is to accelerate e^- bunches to GeV energies, ultimately for high-energy physics applications [26].

Figure 1 shows a schematic of the experimental setup. A 10-m-long source provides rubidium vapor density adjustable in the $n_{vap} = (0.5-10) \cdot 10^{14}$ cm^{-3} range [25]. The density is measured to better than 0.5% [27] at the source ends. An ~ 120 fs, ~ 100 mJ laser pulse ($\lambda = 780$ nm) produces a RIF that creates the plasma by ionizing the vapor (RbI$\rightarrow$RbII). Previous experiments [15] showed that the RIF ionizes $\sim 100\%$ of the vapor along its path, producing an ~ 2-mm-diameter plasma column with density equal to that of the vapor. The RIF is placed $t_p = 620$ ps ($\sim 2.5\,\sigma_t$) ahead of the center of the 400 GeV/c, $\sigma_t \sim 240$ ps, p^+ bunch provided by the CERN SPS. Therefore, it does not seed SM [14]. The p^+ bunch is synchronized with the RIF with root mean square (rms) variation of 15 ps$\ll \sigma_t$, which is therefore negligible.

Optical transition radiation (OTR) is emitted when protons enter an aluminum-coated silicon wafer, positioned 3.5 m downstream of the plasma exit. The OTR is imaged onto the entrance slit of a streak camera that provides time-resolved images of the charge density distribution of the p^+ bunch (t,y) [28] in a ~ 180-µm-wide slice (the spatial resolution of the optical system) near the propagation axis. The streak camera temporal resolution is ~ 2 ps in the 210 ps time window, sufficient to resolve the microbunch train as the plasma period is $T_{pe} = 11.04$ and 11.38 ps, for the values of n_{pe} used in this experiment. An ultraviolet pulse derived from the same laser oscillator as that producing the RIF generates an 18.3 MeV e^- bunch in a photo-injector and booster cavity [29]. The e^- bunch and the RIF have a relative rms timing jitter < 1 ps ($\ll T_{pe}$) [30]. The delay t_{seed} between the e^- and the p^+ bunch centers can be adjusted using a translation stage. We use a magnetic spectrometer [31] to measure the energy spectrum of the e^- bunch after propagation with and without plasma [32].

We use a bleed-through of the ionizing laser pulse, thus also synchronized with the e^- bunch at the sub-ps time scale [33], to determine on the time-resolved images the bunch train timing with respect to that of the e^- bunch. This is necessary to circumvent the ~ 5 ps rms jitter ($\sim T_{pe}/2$) of the triggering system.

Experimental Results.— We first present a new and important result that is necessary for the measurements presented hereafter: the seeding of SM by the e^- bunch. The incoming p^+ bunch with $Q_p = (14.7 \pm 0.2)$ nC has a continuous charge distribution (Fig. 2(a), no plasma) with an approximately 2D-Gaussian (t,y) charge density profile. With the plasma ($n_{pe} = 1.02 \cdot 10^{14}$ cm^{-3}) and the $Q_e = (249 \pm 17)$ pC e^- bunch placed $t_{seed} = 612$ ps ahead of the center of the p^+ bunch, we observe the clear formation of a train of microbunches on the image resulting from the average of ten consecutive single-event images (Fig. 2(b)). This indicates that SM is reproducible from

event to event. The period of the modulation is 11.3 ps, close to T_{pe} as expected from SM [10, 15]. We measure the timing variation of the microbunch train with respect to the e^- bunch by performing a discrete Fourier transform (DFT, see Supplemental Material of [14]) analysis of the on-axis time profile of single-event images. The rms timing variation is $\Delta t_{rms} = 0.06\,T_{pe}$, demonstrating that the e^- bunch effectively seeds SM. The same measurement without the e^- bunch yields $\Delta t_{rms} = 0.26\,T_{pe}$, consistent with uniform variation of the timing over T_{pe} ($\Delta t_{rms} = 0.29\,T_{pe}$), confirming the occurrence of SMI, as was also observed in [14].
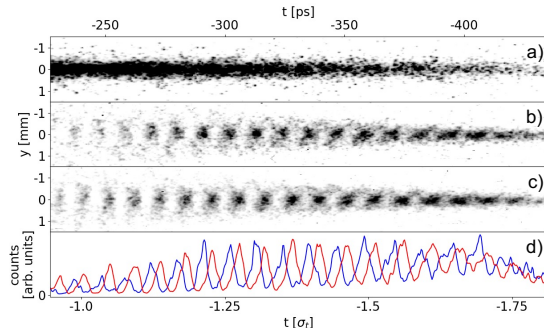

FIG. 2. Time-resolved images (t,y) of the p^+ bunch at the OTR screen obtained by averaging ten single-event images (210 ps, $Q_p = 14.7$ nC). Bunch center at $t = 0$ ps, the bunch travels from left to right. Horizontal axis: time along the bunch normalized to the incoming bunch duration σ_t. a) No plasma (incoming bunch). b) Plasma ($n_{pe} = 1.02 \cdot 10^{14}$ cm^{-3}) and e^- bunch with $Q_e = 249$ pC, $t_{seed} = 614$ ps ahead of the p^+ bunch center. c) Same as (b) but e^- bunch delayed by 6.7 ps ($t_{seed} = 607.3$ ps). All images have the same color scale. d) On-axis time profiles of (b) (blue line) and (c) (red line) obtained by summing counts over $-0.217 \leq y \leq 0.217$ mm.

We also observe seeding of SM with $Q_p = (46.9 \pm 0.5)$ nC and the same value of $Q_e = 249$ pC, i.e., with p^+ bunch and plasma parameters similar to those of [14]. This indicates that the e^- bunch drives transverse wakefields with amplitude exceeding the seeding threshold value of $(2.8-4.0)$ MV/m, determined in [14] when seeding with RIF. The amplitude thus also exceeds that for the lower $Q_p = 14.7$ nC (Fig. 2) since the seeding threshold is expected to scale with Q_p.

Figure 2(c) shows an averaged time-resolved image obtained after delaying the seed e^- bunch timing by 6.7 ps with respect to the case of Fig. 2(b). The bunch train is again clearly visible and timing analysis shows an rms variation of $0.07\,T_{pe}$, confirming the seeding of SM. Figure 2(d) shows that the temporal profiles of Fig. 2(c) (red curve) is shifted in time by (7.2 ± 1.0) ps with respect to that of Fig. 2(b) (blue curve). This demonstrates that the timing of the p^+ bunch modulation and thus also the timing of the wakefields are tied to that of the seed within a small fraction of T_{pe}.

As the amplitude of the wakefields grows along the

bunch and along the plasma [15, 16], one may expect them to produce a smaller size of the successive microbunches at the plasma exit, possibly also with larger emittance due to the nonlinear nature of the transverse wakefields. These two effects are the likely causes for the increase in transverse size of the microbunches along the train observed in Figs. 2(b) and (c), as the OTR screen is positioned 3.5 m downstream of the plasma exit. We also note that the p^+ bunch self-modulates starting from the visible front of the bunch ($t > -1.82\,\sigma_t$ on Figs. 2(b) and (c)), as the seed wakefields act on the entire bunch, and that on these figures the charge density at the bunch front is higher than in the case without plasma (Fig. 2(a)). This is due to the focusing associated with the formation of the microbunches and to global plasma adiabatic focusing (see Fig. 3).

We measure the transverse extent of the p^+ bunch distribution along the bunch on 1.1 ns, time-resolved images (Fig. 3). We define this extent w for each time-column of the image as the distance between the two points ($\pm y$) where the transverse distribution reaches 20% of its peak value, when detectable. In the case without plasma (Fig. 3(a), incoming bunch), $w_{\text{off}} = 1.7\,$mm is constant along the bunch (black dashed line) and corresponds to the $\sigma_y \sim 0.37\,$mm rms size of the bunch at the screen.
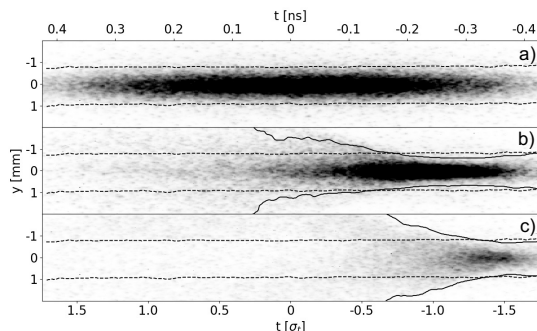

FIG. 3. Time-resolved images (t, y) of the p^+ bunch (1.1 ns, $Q_p = 14.7\,$nC) obtained by averaging ten single-event images. a) No plasma (incoming bunch). b) Plasma ($n_{pe} = 0.97 \cdot 10^{14}\,$cm^{-3}) and no e^- bunch (SMI). c) Plasma and e^- bunch with $Q_e = 249\,$pC (seeded SM). All images have the same color scale. Black dashed lines in (a) and continuous lines in (b) and (c) indicate, for each time-column of the images, the points where the transverse distribution reaches 20% of its peak value. The distance between the lines is the transverse extent w_{off} (a) and w (b, c). Dashed lines of (a) also plotted in (b) and (c) for reference.

In the case with plasma (hereafter $n_{pe} = 0.97 \cdot 10^{14}\,$cm^{-3}) and no e^- bunch (SMI [14], Fig. 3(b)), the transverse extent (black continuous lines) indicates that first the effect of plasma adiabatic focusing dominates, i.e., w decreases, due to the cancellation of the p^+ bunch space-charge field by the plasma electrons ($t < -0.8\,\sigma_t$). Then the effect of defocusing due to SM development dominates and w increases.

We note that the time resolution of these images is not sufficient to evidence the microbunch structure and the charge distribution appears continuous along the bunch.

In the case with plasma and e^- bunch ($Q_e = 249\,$pC, seeded SM, Fig. 3(c), all other parameters kept constant), the same focusing effect as in the SMI case first dominates, but the effect of defocusing starts earlier: $t \sim -1.5\,\sigma_t$ rather than $t \sim -0.8\,\sigma_t$ (Fig. 3(b)).

Figure 4(a) shows that, when increasing the charge of the seed bunch Q_e, the width w along the bunch initially decreases, following the same curve in each case, due to the effect of adiabatic focusing. It then increases with SM growth, reaching the value of the case without plasma (w_{off}) earlier along the bunch, for larger Q_e (red points). Since the global focusing effect is equal in all cases ($Q_p = const$), this shows that an increase in Q_e causes the SM defocusing effect to dominate earlier along the bunch. Afterwards, w increases monotonically and reaches larger values at all times for larger Q_e, as shown in Fig. 4(b) for two times along the bunch (blue points: $t = -1.19\,\sigma_t$, red points: $t = -0.84\,\sigma_t$; first and last t when $w > w_{\text{off}}$ for $Q_e > 0$ and all measurements provide a value).
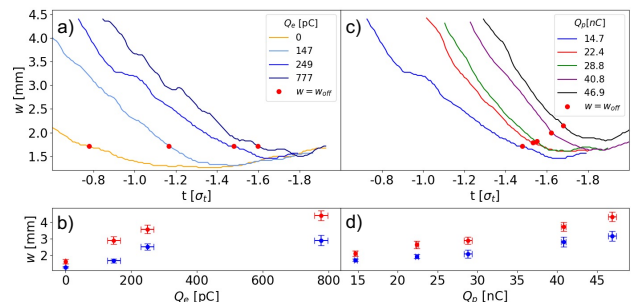

FIG. 4. Top row: transverse extent w along the p^+ bunch as a function of time along the bunch normalized to the incoming bunch duration σ_t. a) Varying the e^- bunch charge (see legend), $Q_e = 0$ (SMI), $Q_e > 0$ (seeded SM), $Q_p = 14.7\,$nC. c) Varying the p^+ bunch charge Q_p (see legend), $Q_e = 249\,$pC. Red points indicate the time along the bunch when $w = w_{\text{off}}$. Bottom row: b) w as a function of Q_e at $t = -1.19$ (blue points) and $t = -0.84\,\sigma_t$ (red points). d) w as a function of Q_p at $t = -1.48$ (blue points) and $t = -1.30\,\sigma_t$ (red points). The error bars indicate the standard deviation of w, and of Q_e and Q_p. Note: blue line: same data on (a) and (c).

Measurement of the energy spectrum of the seed e^- bunch (not shown) [32], and numerical simulation results [34] indicate that the amplitude of the wakefields driven by the e^- bunch W$_{\perp 0}$ over the first $\sim 2\,$m of plasma increases as a function of Q_e and exceeds $4\,$MV/m in all cases. The earlier occurrence of SM defocusing and the increase in w at all times when $w \geq w_{\text{off}}$ for larger Q_e are thus directly caused by the increase in amplitude of the seed wakefields $W_{\perp 0}(Q_e)$, since all other parameters were kept constant ($\Gamma(Q_p) = const$). Figure 4(a) also shows that in the SMI regime ($Q_e = 0$)

the defocusing effect of SM dominates much later along the bunch ($\sim -0.78\,\sigma_t$) and w is much smaller than in the seeded regime ($Q_e > 0$). This lower growth can be attributed to the lower amplitude of the (uncontrolled) initial wakefields, as well as to a later start of SM along the bunch [14].

When increasing the p^+ bunch charge Q_p (Fig. 4(c)), we observe again that w increases at all times along the bunch when SM defocusing effect dominates, as also shown in Fig. 4(d) for two times along the bunch (blue points: $t = -1.48\,\sigma_t$, red points: $t = -1.30\,\sigma_t$; t chosen as in the previous case). Increasing Q_p also increases the emittance, transverse size and bunch density n_p of the p^+ bunch at the plasma entrance [35], and also w_{off} at the screen (red points, Fig.(c)). Therefore, and unlike with Q_e, when increasing Q_p the effect of adiabatic focusing ($\propto n_p$) also increases. However, measurements show that the increase in w with Q_p is even larger and thus the effect of SM defocusing starts dominating earlier along the bunch.

The expected variation of Γ with n_p is $\Gamma \propto n_p^{1/3}$ [10, 21, 23]. Measurements of $\sigma_{x,y}$ and σ_t [35] show that over the $Q_p = (14.7 - 46.9)\,\text{nC}$ range, n_p changes only from 6.9 to $8.9 \cdot 10^{12}\,\text{cm}^{-3}$. However, the effect of this change is observed after exponentiation of SM.

The effect of the increase in transverse size and emittance of the p^+ bunch when increasing Q_p [35] (not explicitly included in Γ) is to reduce the growth of SM [36, 37]. Thus, the increase in Γ with Q_p is likely larger than the increase in w shown by Fig. 4(d).

We note here that the measurement of w is not direct measurement of the amplitude of the seed wakefields $W_{\perp 0}$ or growth rate Γ. However, changes in w are direct consequences of changes in $W_{\perp 0}(Q_e)$ and $\Gamma(Q_p)$. For a direct measurement of Γ all protons would have to leave the wakefields at the same position along the plasma and propagate ballistically an equal distance to the OTR screen. Numerical simulation results show that with the plasma of these experiments longer than the saturation length of SM [20], protons may leave the wakefields earlier or later depending on the amplitude of the wakefields and on the distance they are subject to them. However, simulations also show monotonic increase of w, as observed in the experiments, and that w increases with increasing amplitude of the wakefields along the bunch.

Summary. — We demonstrated in experiments that a short e^- bunch can seed SM of a long p^+ bunch in plasma. We showed that when increasing the e^- (Q_e) or the p^+ (Q_p) bunch charge, the transverse extent of the p^+ bunch distribution w along the bunch (measured after the plasma) also increases. We attribute these changes to the change in amplitude of the seed wakefields ($Q_e \rightarrow W_{\perp 0}$) and in growth rate of SM ($Q_p \rightarrow \Gamma$), in agreement with theoretical and simulation results.

These results show that SM is well understood and can be well controlled. Control is key for optimization of the SM wakefields for particle acceleration [38, 39].

* livio.verra@cern.ch

[1] B. Lehnert, Experimental evidence of plasma instabilities, Plasma Physics **9**, 301 (1967).

[2] A. M. Bykov, A. Brandenburg, M. A. Malkov, S. M. Osipov, Microphysics of cosmic ray driven plasma instabilities, Space Science Reviews **178**, 201 (2013), https://doi.org/10.1007/s11214-013-9988-3.

[3] F. Haas, Neutrino oscillations and instabilities in degenerate relativistic astrophysical plasmas, Phys. Rev. E **99**, 063209 (2019).

[4] F. F. Cap, *Handbook on Plasma Instabilities*, edited by F. F. Cap (Academic Press, 1976).

[5] D. S. Montgomery, Two decades of progress in understanding and control of laser plasma instabilities in indirect drive inertial fusion, Physics of Plasmas **23**, 055601 (2016), https://doi.org/10.1063/1.4946016.

[6] D. U. Sharma K., Comprehensive review on various instabilities in semiconductor quantum plasma, Brazilian Journal of Physics **51**, 1944 (2021).

[7] P. Arnold, J. Lenaghan, G. D. Moore, and L. G. Yaffe, Apparent thermalization due to plasma instabilities in the quark-gluon plasma, Phys. Rev. Lett. **94**, 072302 (2005).

[8] D. T. Farley, Two-stream plasma instability as a source of irregularities in the ionosphere, Phys. Rev. Lett. **10**, 279 (1963).

[9] O. Buneman, Excitation of field aligned sound waves by electron streams, Phys. Rev. Lett. **10**, 285 (1963).

[10] N. Kumar, A. Pukhov, and K. Lotov, Self-modulation instability of a long proton bunch in plasmas, Phys. Rev. Lett. **104**, 255003 (2010).

[11] T. Tajima and J. M. Dawson, Laser electron accelerator, Phys. Rev. Lett. **43**, 267 (1979).

[12] P. Chen, J. M. Dawson, R. W. Huff, and T. Katsouleas, Acceleration of electrons by the interaction of a bunched electron beam with a plasma, Phys. Rev. Lett. **54**, 693 (1985).

[13] K. V. Lotov, G. Z. Lotova, V. I. Lotov, A. Upadhyay, T. Tückmantel, A. Pukhov, and A. Caldwell, Natural noise and external wakefield seeding in a proton-driven plasma accelerator, Phys. Rev. ST Accel. Beams **16**, 041301 (2013).

[14] F. Batsch, P. Muggli et al. (AWAKE Collaboration), Transition between instability and seeded self-modulation of a relativistic particle bunch in plasma, Phys. Rev. Lett. **126**, 164802 (2021).

[15] AWAKE Collaboration, Experimental observation of proton bunch modulation in a plasma at varying plasma densities, Phys. Rev. Lett. **122**, 054802 (2019).

[16] M. Turner et al. (AWAKE Collaboration), Experimental observation of plasma wakefield growth driven by the seeded self-modulation of a proton bunch, Phys. Rev. Lett. **122**, 054801 (2019).

[17] AWAKE Collaboration, Acceleration of electrons in the plasma wakefield of a proton bunch, Nature **561**, 363 (2018).

[18] M. Hüther and P. Muggli, Seeding of the self-modulation in a long proton bunch by charge cancellation with a short electron bunch, Nuclear Instruments and Methods in Physics Research Section A: Accelerators, Spectrometers, Detectors and Associated Equipment **909**, 67 (2018), 3rd European Advanced Accelerator Concepts workshop (EAAC2017).

[19] P. Muggli, P. I. Morales Guzman, A.-M. Bachmann, M. Hüther, M. Moreira, M. Turner, J. Vieira, Seeding self-modulation of a long proton bunch with a short electron bunch, Journal of Physics: Conference Series **1596**, 012066 (2020).

[20] M. Turner, P. Muggli et al. (AWAKE Collaboration), Experimental study of wakefields driven by a self-modulating proton bunch in plasma, Phys. Rev. Accel. Beams **23**, 081302 (2020).

[21] A. Pukhov, N. Kumar, T. Tückmantel, A. Upadhyay, K. Lotov, P. Muggli, V. Khudik, C. Siemon, and G. Shvets, Phase velocity and particle injection in a self-modulated proton-driven plasma wakefield accelerator, Phys. Rev. Lett. **107**, 145003 (2011).

[22] K. V. Lotov, Physics of beam self-modulation in plasma wakefield accelerators, Physics of Plasmas **22**, 103110 (2015), https://doi.org/10.1063/1.4933129.

[23] C. B. Schroeder, C. Benedetti, E. Esarey, F. J. Grüner, and W. P. Leemans, Growth and phase velocity of self-modulated beam-driven plasma waves, Phys. Rev. Lett. **107**, 145002 (2011).

[24] K. V. Lotov and P. V. Tuev, Plasma wakefield acceleration beyond the dephasing limit with 400 GeV proton driver, Plasma Physics and Controlled Fusion **63**, 125027 (2021).

[25] P Muggli et al. (AWAKE Collaboration), AWAKE readiness for the study of the seeded self-modulation of a 400 GeV proton bunch, Plasma Physics and Controlled Fusion **60**, 014046 (2017).

[26] A. Caldwell and M. Wing, VHEeP: a very high energy electron–proton collider, The European Physical Journal C **76**, 10.1140/epjc/s10052-016-4316-1 (2016).

[27] F. Batsch, M. Martyanov, E. Oez, J. Moody, E. Gschwendtner, A. Caldwell, and P. Muggli, Interferometer-based high-accuracy white light measurement of neutral rubidium density and gradient at AWAKE, Nuclear Instruments and Methods in Physics Research Section A: Accelerators, Spectrometers, Detectors and Associated Equipment **909**, 359 (2018), 3rd European Advanced Accelerator Concepts workshop (EAAC2017).

[28] K. Rieger, A. Caldwell, O. Reimann, R. Tarkeshian and P. Muggli, GHz modulation detection using a streak camera: Suitability of streak cameras in the AWAKE experiment, Review of Scientific Instruments **88**, 025110 (2017), https://doi.org/10.1063/1.4975380.

[29] K. Pepitone, S. Doebert, G. Burt, E. Chevallay, N. Chritin, C. Delory, V. Fedosseev, C. Hessler, G. McMonagle, O. Mete, V. Verzilov, and R. Apsimon, The electron accelerator for the AWAKE experiment at CERN, Nuclear Instruments and Methods in Physics Research Section A: Accelerators, Spectrometers, Detectors and Associated Equipment **829**, 73 (2016), 2nd European Advanced Accelerator Concepts Workshop - EAAC 2015.

[30] A.-M. Bachmann, Self-Modulation Development of a Proton Bunch in Plasma, PhD thesis, Technical University Munich, CERN-THESIS-2021-094 (2021).

[31] J. Bauche, B. Biskup, M. Cascella, J. Chappell, N. Chritin, D. Cooke, L. Deacon, Q. Deliege, I. Gorgisyan, J. Hansen, S. Jolly, F. Keeble, P. La Penna, S. Mazzoni, D. Medina Godoy, A. Petrenko, M. Quattri, T. Schneider, P. Sherwood, A. Vorozhtsov, and M. Wing, A magnetic spectrometer to measure electron bunches accelerated at AWAKE, Nuclear Instruments and Methods in Physics Research Section A: Accelerators, Spectrometers, Detectors and Associated Equipment **940**, 103 (2019).

[32] L. Verra, G. Zevi Della Porta, K.-J. Moon, A.-M. Bachmann, E. Gschwendtner and P. Muggli, Seeding of proton bunch self-modulation by an electron bunch in plasma, EuroPhysics Conference Abstracts **45A** (2021).

[33] F. Batsch, Setup and characteristics of a timing reference signal with sub-ps accuracy for AWAKE, Journal of Physics: Conference Series **1596**, 012006 (2020).

[34] K.-J. Moon, In preparation.

[35] When Q_p varies in the range $(14.8 - 47.2)\,\mathrm{nC}$, the transverse size at the plasma entrance and normalized emittance of the p^+ bunch vary accordingly in the ranges $\sigma_{x,y} = (0.11, 0.10 - 0.18, 0.17)\,\mathrm{mm}$ and $\epsilon_N = (1.9 - 4.2)\,\mathrm{mm}$ mrad, respectively, and the bunch duration remains in the range $\sigma_t \sim (236 - 255)\,\mathrm{ps}$, leading to the bunch density values quoted in the text.

[36] A. Gorn, M. Turner et al. (AWAKE Collaboration), Proton beam defocusing in AWAKE: comparison of simulations and measurements, Plasma Physics and Controlled Fusion 10.1088/1361-6587/abc298 (2020).

[37] K. V. Lotov, Effect of beam emittance on self-modulation of long beams in plasma wakefield accelerators, Physics of Plasmas **22**, 123107 (2015), https://doi.org/10.1063/1.4936973.

[38] V. K. B. Olsen, E. Adli, and P. Muggli, Emittance preservation of an electron beam in a loaded quasilinear plasma wakefield, Phys. Rev. Accel. Beams **21**, 011301 (2018).

[39] P. Muggli, Physics to plan AWAKE run 2, Journal of Physics: Conference Series **1596**, 012008 (2020).

Adiabatic Focusing of a Long Proton Bunch in Plasma

L. Verra[1,2,3], E. Gschwendtner[1], and P. Muggli[2], for the AWAKE Collaboration

[1] *CERN, Geneva 1211, Switzerland*

[2] *Max Planck Institute for Physics, Munich 80805, Germany*

[3] *Technical University Munich, Garching 85748, Germany*

We show in experiments that a long, relativistic p^+ bunch is focused by the plasma adiabatic response. The free plasma electrons migrate so as to neutralize the space-charge field of the bunch [1], and the bunch is therefore focused by the azimuthal magnetic field generated by its own current, that is not balanced by the radial electric field [2, 3, 4]. Since the length of the bunch is much longer than the plasma electron wavelength, the bunch also undergoes the self-modulation instability [5, 6]. Thus, the amplitude of the wakefields grows along the bunch and along the plasma, and the defocusing effect of the self-modulation can become dominant over the adiabatic focusing effect. We show that, when seeding the self-modulation with a preceding e^- bunch [7], the transition between the effect of the adiabatic response and that of the self-modulation depends on the amplitude of the seed wakefields.

References

[1] P. Chen, J. M. Dawson, R. W. Huff, and T. Katsouleas, Acceleration of electrons by the interaction of a bunched electron beam with a plasma, Phys. Rev. Lett. 54, 693 (1985)

[2] P. Chen, K. Oide, A. M. Sessler, and S. S. Yu, Plasma-based adiabatic focuser, Phys. Rev. Lett. 64, 1231 (1990)

[3] G. Hairapetian, P. Davis, C. E. Clayton, C. Joshi, S. C. Hartman, C. Pellegrini, T. Katsouleas, Experimental Demonstration of Dynamic Focusing of a Relativistic Electron Bunch by an Overdense Plasma Lens, Phys. Rev. Lett. 72, 2403 (1994)

[4] J. S. T. Ng et al., Observation of Plasma Focusing of a 28.5 GeV Positron Beam, Phys. Rev. Lett. 87, 244801 (2001)

[5] AWAKE Collaboration, Experimental observation of proton bunch modulation in a plasma at varying plasma densities, Phys. Rev. Lett. 122, 054802 (2019)

[6] M. Turner et al. (AWAKE Collaboration), Experimental observation of plasma wakefield growth driven by the seeded self-modulation of a proton bunch, Phys. Rev. Lett. 122, 054801 (2019)

[7] L. Verra et al. (AWAKE Collaboration), to be submitted.

Seeding of proton bunch self-modulation by an electron bunch in plasma

L. Verra[1,2,3,*], G. Zevi Della Porta[1], K.-J. Moon[4],
A.-M. Bachmann[2], E. Gschwendtner[1] and P. Muggli[2]

[1] *CERN, Geneva 1211, Switzerland*
[2] *Max Planck Institute for Physics, Munich 80805, Germany*
[3] *Technical University Munich, Garching 85748, Germany*
[4] *UNIST, Ulsan 44919, South Korea*

Introduction

The AWAKE experiment at CERN [1] relies on the self-modulation in plasma of the long 400 GeV/c proton bunch from the CERN SPS, to accelerate an externally injected electron bunch to GeV energies. The control of the acceleration requires that the self-modulation process and the electron beam injection are reproducible from event to event. Making the self-modulation instability (SMI) reproducible means that the phase and the amplitude of the plasma wakefields along the driver bunch are fixed, once the process has saturated. This is achieved by seeding the instability, and the process is therefore called seeded self-modulation (SSM). Proton bunch SSM using a relativistic ionization front method [2, 3, 4], and the acceleration of electrons [5] were demonstrated during AWAKE Run 1. The physics of seeding using a short electron bunch will be studied during Run 2a (starting in July 2021) [6, 7].

Electron bunch seeding of the self-modulation

When an electron bunch travels in plasma, it drives wakefields that can impose a charge modulation on the trailing proton bunch (see Figure 1a). If this modulation is deep enough (i.e. the amplitude of the wakefields is above the seeding threshold), the self-modulation process is seeded and grows resonantly until the proton bunch is fully modulated (see Figure 1b). Thus, the final phase of the microbunch train (and of the wakefields) is uniquely related in phase to the short seed electron bunch.

AWAKE Run 2a is using the same experimental setup as Run 1 [1, 7]. The main elements are: a 10 meter-long Rb vapor source, a 120 fs, < 450 mJ laser pulse ($\lambda = 780$ nm) ionizing the Rb atoms and creating the plasma column, the electron beam source and transfer line, a magnetic spectrometer system downstream of the plasma. The initial plasma electron density n_{pe} can be varied in a range from 0.5 to $10 \cdot 10^{14}$ cm^{-3}, the energy of the electron bunch from 10 to 20 MeV

*livio.verra@cern.ch

with 0.5% relative energy spread, the charge from 100 to 600 pC (with normalized transverse emittance and bunch length σ_z scaling accordingly from 1 to 6 mm·mrad and from 2 to 5 ps). The electron bunch transverse size at the plasma entrance can be adjusted using a quadrupole triplet final focusing system to a minimum size $\sigma_r \sim 200\,\mu$m.

As shown in [4], the phase of the train of proton microbunches is reproducible (therefore SSM has occurred) when the amplitude of the seed wakefield is larger than a threshold value. Using the relativistic ionization front seeding method, the threshold was determined to be between 4 and 6 MV/m (with $n_{pe} = 0.9 \cdot 10^{-14}\,\text{cm}^{-3}$). Linear plasma wakefields theory [9] shows that with the initial parameters of the AWAKE electron bunch, it would not be possible to effectively seed the self-modulation. For $Q = 150$ pC, $\sigma_z = 2$ ps, $\sigma_r = 200\,\mu$m, $n_{pe} = 2 \cdot 10^{-14}\,\text{cm}^{-3}$, the maximum amplitude of the transverse wakefields $W_\perp$ behind the bunch at $r = \sigma_r$ is 3 MV/m. The electron beam transverse size, though, evolves according to $\gamma m \frac{d^2\sigma_r}{dt^2} = qW_\perp$ (where q and m are the electron charge and mass and γ the relativistic factor): using linear optics, one can esti-
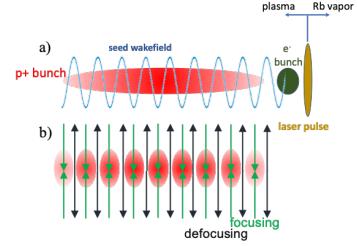

Figure 1: *Schematic of the electron bunch seeding process. a) Beams at the injection and initial wakefields; b) Fully modulated train of microbunches and transverse wakefields at saturation.*

mate the initial bunch radius σ_{r0} at the injection so that the amplitude of the wakefields within the bunch at $r = \sigma_{r0}$ balances the divergence of the bunch and therefore the size remains constant along the plasma. For the same parameters mentioned above, $\sigma_{r0} \sim 7\,\mu$m, much smaller than the minimum achievable size at the plasma entrance in the experiment. Therefore, the bunch undergoes severe non-linear pinching in the first centimeters of propagation in plasma [10], and numerical simulations are required to describe and compute its transverse size. Simulations [11, 12] show that, because of this transverse size evolution, the bunch charge density becomes high enough to drive transverse wakefields with amplitude above the seeding threshold.

The goal of Run 2a is not only to experimentally prove the seeding of the self-modulation of the long proton bunch using an electron bunch, but also to vary the initial parameters of the electron bunch (and therefore the amplitude of the initial wakefields) to observe the transition between SMI and SSM.

Preparatory experimental studies

Before performing the electron bunch seeding experiment with the SPS proton bunch, we want to study the effect of the propagation through the 10 meter-long plasma column [13] on the electron bunch. As the low-energy bunch drives wakefields and loose a significant amount of its

energy, we expect a fraction of the electrons to be dephased with respect to the wakefields, and to be defocused, and to detect the energy loss as a long low-energy tail in the energy spectrum of the bunch on the spectrometer screen. Figure 2a shows the $150\,\mathrm{pC}$ and $\sim 18.5\,\mathrm{MeV}$ electron bunch, propagated through vacuum and imaged onto the spectrometer screen. Figure 2b shows the electron bunch with the same input parameters after propagation through $10\,\mathrm{m}$ of plasma ($n_{pe} = 2 \cdot 10^{14}\,\mathrm{cm^{-3}}$). As the beam is dispersed in the horizontal plane, the horizontal axis of the screen is converted into energy. One notices the long low-energy tail, showing energy loss occurred in the plasma.
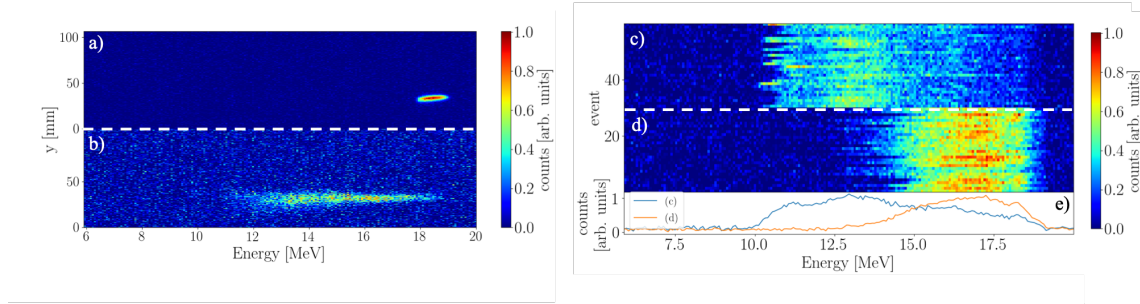

Figure 2: *a) Electron bunch imaged onto the spectrometer screen after propagation through vacuum. b) Electron bunch imaged onto the spectrometer screen after propagation through 10 meters of plasma. The horizontal axis is the dispersive plane. The counts of each image are normalized to the respective maximum. c) and d) show a waterfall plot of the energy projections of the electron beam imaged on the spectrometer screen. c) 30 events with the smallest beam size at the plasma entrance; d) 30 events with the largest beam size at the plasma entrance. e) sums of the energy distributions for the two cases: (c) in blue and (d) in orange. For all images, the electron bunch charge at the plasma entrance is 150 pC and the energy is ~ 18.5 MeV.*

During the first experimental campaign, we varied the size at the plasma entrance of the $150\,\mathrm{pC}$, $18.5\,\mathrm{MeV}$ electron bunch (and $n_{pe} = 2 \cdot 10^{14}\,\mathrm{cm^{-3}}$). Figure 2 (c and d) show a waterfall plot of the projections along the energy axis of images at the spectrometer screen. We collected 30 events with the smallest beam size at the injection (beam focused at the plasma entrance, $\sigma_r \sim 200\,\mu\mathrm{m}$ (c)) and 30 events with the largest beam size (beam focused $5\,\mathrm{m}$ downstream of the plasma entrance, $\sigma_r \sim 1\,\mathrm{mm}$ (d)). We note here that the energy distributions reach lower values for the smaller beam size (the minimum energy is detected around $10\,\mathrm{MeV}$) indicating that the smaller beam (with larger charge density) experiences more energy loss. We also show in Figure 2e the sum of the energy distributions for the two cases: the minimum energy and the mean of the distribution are clearly different in the two cases. The energy of one electron along the propagation length L evolves according to: $\Delta W = q \int_0^L E_z(z)dz$, where E_z is the longitudinal

wakefield within the bunch. What we observe on the screen is the results of a complex dynamics, as E_z varies along the bunch and along the plasma.

Simulations [12] show that the amplitude of the decelerating fields inside the bunch and of the transverse fields behind the bunch are maximum over the first 2 meters of plasma, where the transverse pinching occurs. Then, due to dephasing, some charge is expelled out of the plasma and the bunch length becomes comparable to the plasma wavelength, making the wakefields decrease and the bunch transverse size increase. To summarize, the energy spectrum, observed after the propagation in plasma, is mostly affected by the longitudinal and transverse evolution of the bunch and of the wakefields over the first meters of propagation, which in turn are directly related to the initial parameters of the electron bunch, in particular its charge density.

Conclusions

We have discussed the electron bunch seeding process of the proton bunch self-modulation, that will be studied in the context of AWAKE Run 2a. We have shown that we are able to vary the energy loss of the seed electron bunch in plasma by changing its initial parameters. We will perform the same type of measurements in the presence of the proton bunch, including the variation of other parameters (e.g. electron bunch charge, for a fixed bunch size), to study the phase reproducibility of the self-modulation of the proton bunch and the transition from SMI to SSM, using the electron bunch seeding method.

References

[1] P. Muggli et al. (AWAKE Collaboration), Plasma Phys. Control. Fusion, **60**(1) 014046 (2017).

[2] AWAKE Collaboration, Phys. Rev. Lett. **122**, 054802 (2019).

[3] M. Turner et al. (AWAKE Collaboration), Phys. Rev. Lett. **122**, 054801 (2019).

[4] F. Batsch et al. (AWAKE Collaboration), Phys. Rev. Lett. **126**, 164802 (2021).

[5] AWAKE Collaboration, Nature **561**, 363–367 (2018).

[6] P. Muggli, J. Phys.: Conf. Ser. **1596** 012008 (2020).

[7] E. Gschwendtner, for the AWAKE Coll., in 12th International Particle Accelerator Conference, ID: 1768 (2021).

[8] P. Muggli et al., J. Phys.: Conf. Ser. **1596** 012066 (2020).

[9] R. Keinigs and M. E. Jones, The Physics of Fluids **30**, 252 (1987).

[10] K. V. Lotov, Phys. Plasmas **24**, 023119 (2017).

[11] A.-M. Bachmann, Ph. D. Thesis, Technical University of Munich (2021).

[12] K.-J. Moon, these Proceedings, ID: 2301.

[13] G. Zevi Della Porta et al., in 12th International Particle Accelerator Conference, ID: 1764 (2021).

Study of external electron beam injection into proton driven plasma wakefields for AWAKE Run2

L. Verra[1,2,3], E. Gschwendtner[1] and P. Muggli[2]

[1] CERN, Geneva, Switzerland
[2] Max-Planck Institute for Physics, Munich, Germany
[3] Technical University Munich, Munich, Germany

E-mail: `livio.verra@cern.ch`

Abstract.
    We describe an external electron injection scheme for the AWAKE experiment. We use scattering in two foils, that are necessary as vacuum window and laser beam dump, to decrease the betatron function of the incoming electron beam for injection and matching into plasma wakefields driven by a self-modulated proton bunch. We show that, for a total aluminum foil thickness of $\sim 280 \, \mu$m, multiple Coulomb scattering increases the beam emittance by a factor of ~ 10 and decreases the betatron function by a factor of ~ 3. The plasma in the accelerator is created by a ionizing laser pulse, counter-propagating with respect to the electron beam. This allows for the electron bunch to enter the plasma through an "infinitely" sharp vapor-plasma boundary, away from the foils.

1. Introduction

During its first experimental run (2016-2018), AWAKE (the Advanced WAKEfield experiment) [1] reached two important milestones: the demonstration of the seeded self-modulation of the 400 GeV/c proton bunch delivered by the CERN Super Proton Synchrotron [2][3], and the acceleration of externally injected electrons from 19 MeV up to 2 GeV [4]. The goal of the second run is to accelerate a 165 MeV electron bunch while preserving its quality. For AWAKE Run2 [5] we plan to use two separated plasma sources: one dedicated to the self-modulation of the proton bunch (seeded by an electron bunch) and one to the electron acceleration (see Figure 1).
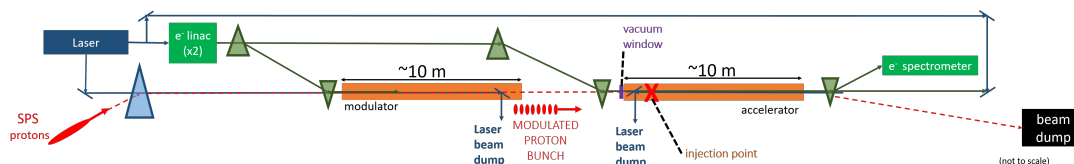

Figure 1. Schematic drawing of the AWAKE Run2 setup.

A short vacuum gap (with length of ~ 30 cm) separates the two sources, and aluminum windows confine the rubidium vapor to the sources. In the gap region, the electron beam

trajectory merges with the proton beam one, so as to inject the witness bunch on axis into the wakefields. A laser pulse ($\sigma_\tau = 120\,\text{fs}$, $E < 450\text{mJ}$, $\lambda = 780\,\text{nm}$) is split to ionize separately the rubidium vapor in the two sources. In the first source, the laser pulse co-propagates with the proton bunch and is stopped by the laser beam dump. In the second source, the laser pulse counter-propagates with respect to the particle bunches. Particles thus enter the plasma through an "infinitely" sharp in space, but extended in time (on the order of half the bunch duration), boundary between vapor and plasma. The electron bunch parameters are such that it is directly matched to the ion column focusing force. Using a plasma density ramp to assist the matching of the beam would require a room temperature expansion volume between the two vapor sources and would make the gap between the two plasmas too long for effective excitation of wakefields in the second plasma [6]. Laser beam dumps protect the vacuum windows in each source. Hence, the proton and electron beams cross these aluminum foils upstream the injection point. While the effect on the proton beam optical properties is negligible, the electron beam is strongly affected by scattering in the material. In this paper we study the incoming electron beam parameters to achieve matching to the plasma focusing force.

2. Electron beam injection

2.1. Blowout, beam loading, beam matching

The final goal of the AWAKE experiment is to provide an electron beam suitable for applications to high-energy physics (fixed target or electron-proton collision experiments). To do this, it is necessary that the electron bunch carries a high charge ($> 100\,\text{pC}$), that the normalized emittance is sufficiently low ($10 - 20\,\text{mm}\cdot\text{mrad}$), and that the final energy spread is kept at, or below, the $\%-$level.

The bunch must be injected in the accelerating and focusing phase of the wakefields. Therefore, the electron bunch length σ_z must be much shorter than a quarter of the plasma electron wavelength $\lambda_{pe} = 2\pi c/\omega_{pe}$, where c is the speed of light and $\omega_{pe} = \sqrt{n_{pe}e^2/\epsilon_0 m_e}$ is the angular plasma electron frequency (n_{pe} is the plasma electron density, e is the elementary charge, ϵ_0 is the vacuum permittivity, m_e is the electron mass). This would insure high efficiency of the capture process. At the baseline plasma electron density ($n_{pe} = 7 \cdot 10^{14}\,\text{cm}^{-3}$), $\lambda_{pe} \sim 1.2\,\text{mm}$; by design, $\sigma_z = 60\,\mu\text{m}$ [5].

According to Liouville's theorem, the incoming emittance is preserved if the transverse focusing force acting on the witness beam increases linearly with the distance from the axis. This is achieved by fully blowing out the plasma electrons from the plasma cavity [7]: the system enters in the so-called blowout, non-linear regime. In this scenario, the focusing force generated by the pure, uniform density ion column is radially linear, therefore the electron bunch slice emittance can be conserved. Simulations [8] show that, even though the AWAKE proton microbunches generate plasma wakefields only in the quasilinear regime ($\delta n_{pe} \leq n_{pe}$), an intense enough electron bunch ($n_{eb} > 35 n_{pe}$, with n_{eb} the charge density of the electron bunch, for a bunch length of $60\,\mu\text{m}$) can expel all the residual plasma electrons from the propagation axis, leaving an ion column behind.

In order to accelerate this bunch with a low energy spread, it is necessary to flatten the longitudinal wakefield amplitude along the bunch, so that most of the witness bunch particles experience the same accelerating gradient. This is possible with beam loading [9]: the witness bunch is positioned such that its own wakefields, superimposed to the wakefields driven by the proton bunch train, make the accelerating field approximately constant along the witness bunch.

To maintain blowout and beam loading, the electron bunch charge density may not oscillate while propagating along the plasma. This is satisfied by matching the electron beam to the plasma ion column focusing force. When the beam is injected into the wakefields, its transverse

size σ follows the envelope equation:

$$\sigma''(z) + (K_\beta^2 - \frac{\epsilon_g^2}{\sigma^4(z)})\sigma(z) = 0, \tag{1}$$

where $K_\beta = \frac{\omega_{pe}}{c\sqrt{2\gamma}}$ is the focusing term of the ion column (γ is the Lorentz factor), and the $\frac{\epsilon_g^2}{\sigma^4(z)}$ term describes the divergence of the beam due to its geometric emittance ϵ_g. The beam is matched to the plasma (and therefore its envelope does not oscillate along the plasma) when it is injected at the waist ($\sigma'(z_{inj}) = 0$, where z_{inj} is the longitudinal position of the injection point, i.e. the plasma entrance) and the term in parenthesis in Equation 1 vanishes, i.e. the focusing force exactly balances the divergence of the beam. Satisfying these conditions yields:

$$\beta^* = \sqrt{\frac{2\epsilon_0 m_e c^2 \gamma}{n_{pe} e^2}}, \tag{2}$$

where $\beta^* = \sigma^{*2}/\epsilon_g$ is the betatron function of the electron beam at the injection point (therefore, at the beam waist). Thus, Equation 2 defines the matching condition for β^*, and therefore for the transverse beam size and emittance, accordingly.

2.2. Electron beam injection and matching in the AWAKE experiment

For the AWAKE Run2 baseline parameters, the electron beam energy is 165 MeV and $n_{pe} = 7 \cdot 10^{14}$ cm^{-3}, hence $\beta^* = 5.1$ mm (for a normalized emittance $\epsilon_N = 20$ mm $\cdot$ mrad, $\sigma^* = 17.7 \, \mu$m). This is a rather short value that is challenging to produce in the AWAKE geometry, since it requires strong focusing close to the waist location. Increasing this value for the incoming beam is therefore desirable. As mentioned above, the electron beam has to cross two aluminum foils before the injection (a vacuum window and a laser beam dump). We choose aluminum because of the good trade-off between its radiation length ($X_0 \sim 9$ cm) and its mechanical properties. The incoming beam parameters are spoiled because of multiple scattering inside the material [10]: the emittance increases, the betatron function decreases, the position of the waist moves upstream [11]. Therefore, since the plasma parameters determine β^* after the foils, we calculate backwards the necessary incoming beam parameters (incoming betatron function β_{in}^* and position of the waist respect to the laser beam dump position) and the maximum possible foil thickness in order to match the beam with the plasma at the injection point, according to:

$$\epsilon_{in}^2 - \epsilon_g^2 = \sigma_{f2}^2 \theta_{f2}^2 + \sigma_{f1}^2 \theta_{f1}^2, \tag{3}$$

where $\epsilon_{in}, \sigma_{f2}, \theta_{f2}$ and $\epsilon_g, \sigma_{f1}, \theta_{f1}$ are the geometric emittance, transverse beam size, scattering angle at the vacuum window and at the laser beam dump, respectively, and

$$\beta_{in}^* = \frac{\epsilon_{in}}{\epsilon_g - \beta^*(\theta_{f1}^2 + \theta_{f2}^2)} \cdot \beta^*, \tag{4}$$

Figure 2 shows the required betatron function to achieve a normalized emittance $\epsilon_N = \beta\gamma\epsilon_g = 20$ mm$\cdot$mrad (β is the ratio of the beam velocity to c) and $\beta^* = 5.1$ mm at the injection, assuming an initial normalized emittance of 2 mm$\cdot$mrad (nominal value provided by the electron beamline design), as a function of the total amount of material in the beam path.

Note that, as the foils thickness increases, β_{in}^* has to increase, but it is independent of the distance between the two foils (Equation 4). The black dashed line indicates the maximum amount of material that can be positioned in the beam path. For a foil thicker than this value, the divergence contribution of the multiple scattering $< \theta^2 >$ becomes too large to be compensated by any convergence angle. Therefore, the beam defocuses at the foil exit and
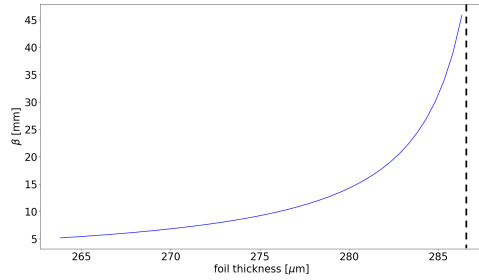
Figure 2. Incoming betatron function β_{in}^* as a function of the foil thickness required to reach the goal parameters at the injection point.

cannot be matched to the plasma wakefields. The decrease of the betatron function, as the beam crosses the material, means that the beam waist moves closer to the foil.

Hence, the beamline does not have to provide directly $\beta_{in}^* = \beta^*$, that is very challenging to produce and require to position the last focusing element very close to the injection point. Instead, we exploit the two foils, needed as vacuum window and beam dump, to relax the request on the betatron function.

We also calculate the position respect to the laser beam dump where the incoming beam waist needs to be set (without foils and scattering), as a function of the distance between the two foils (Figure 3, blue line). The upper limit is given by the requirement that the beam does not diverge upstream the laser beam dump. Figure 3 also shows the final position of the waist with foils and scattering (orange line): this is closer to the foils (i.e. upstream) than without scattering, as expected. Using the calculated betatron function and waist position, we can estimate the maximum distance from the plasma entrance where the last focusing element can be positioned. Considering the linear field area of a quadrupole magnet to have a radial dimension $r \sim 20$ mm, the upper limit of the distance for the magnet to accept the whole beam (i.e. $3\sigma < r$) is ~ 10 m. Still, in order to keep $\sigma < 10$ mm inside the magnets, the last focusing element is positioned as closed as possible to the gap region, depending on the beamline bending angle.
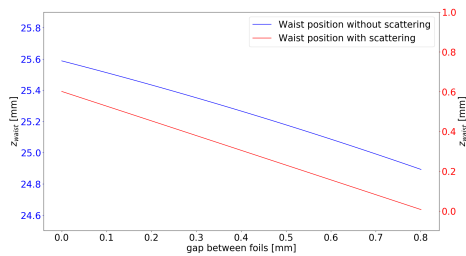

Figure 3. Position of the waist with (orange line) and without (blue line) scattering, respect to the laser beam dump, as a function of the gap between the two foils.

When the beam is correctly matched to the plasma ion column (see the green line in Figure 4), its transverse size does not oscillate along the plasma. The bunch charge density does not change and the blowout and beam loading are maintained along the entire plasma length. On the contrary, when the beam is mismatched (see blue and red lines) betatron oscillations of the beam envelope take place. The beam size along the plasma is obtained by integrating Equation 1 with particular initial condition:

$$\sigma(z) = \sqrt{\frac{\epsilon_g(\sqrt{F^2 + 1} + F cos(2\sqrt{K_\beta}z))^{1/2}}{\sqrt{K_\beta}}}, \tag{5}$$

where $F = \frac{(K_\beta \sigma^{*4}/\epsilon_g^2) - 1}{2\sqrt{K_\beta \sigma^{*2}/\epsilon_g}}$. Moreover, even though the betatron function at the waist is equal to β^* (calculated with Equation 2), the envelope starts oscillating when the beam is not injected at the waist ($\sigma'(z_{inj}) \neq 0$), as shown in Figure 5. Since the plasma entrance is determined by the location of the counter-propagating ionization laser pulse and electron bunch meeting point, mismatch caused by $\sigma'(z_{inj}) \neq 0$ can be corrected by adjusting the relative timing between the pulse and the bunch. The value of the betatron function also determines the required timing precision needed for the meeting point. This time has to be much shorter than the transition time of the bunch over one β^*. In this case, $\beta^*/c = 17$ ps. We also note that, as the crossing distance is on the order of $\sigma_z << \beta^*$, the entire bunch can be considered as injected and matched at once. Instead, mismatching caused by the wrong transverse waist size can only be corrected by adjusting the incoming beam optical properties.

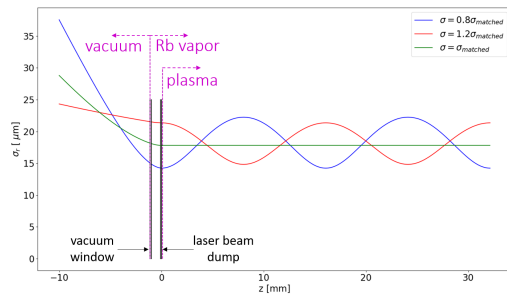**Figure 4.** Transverse electron beam envelope (from Equation 5) in vacuum ($z < -1$ mm), in Rb vapor between foils ($-1 < z < 0$ mm) and along the plasma ($z > 0.1$ mm) for the case of a matched (green line), under-matched (red) and over-matched (blue) beam. In this case, $\sigma_{matched} = 17.7 \, \mu$m
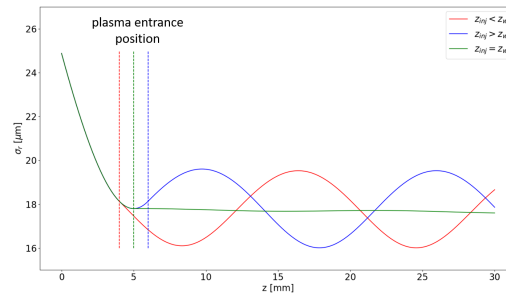

Figure 5. Transverse electron beam envelope (from Equation 5) in the plasma for the case of a beam injected at the waist ($z_{inj} = z_w$, green line), of an early injected beam ($z_{inj} = z_w - 1$ mm, red line) and of a late injected beam ($z_{inj} = z_w + 1$ mm, blue line). $\beta = \beta^*$ for all the examples.

2.3. Effect of acceleration on electron beam matching

So far, we determined the matching condition at the plasma entrance for the incoming beam energy. But energy gain occurs along the plasma ($\gamma(z) = \gamma_0(1 + \frac{d\gamma}{dz}dz)$), potentially leading to loss of the matching condition. However, when the energy gain per unit length is small enough so that $\frac{d\gamma}{dz} << \frac{\gamma}{\lambda_\beta}$, the matching is mostly maintained. The transverse bunch size therefore adiabatically adjusts to satisfy the matching condition as the energy changes, according to $\sigma \propto \gamma^{1/4}$ (from Equation 2). In this case, $\gamma = \gamma(z)$ in Equation 1, that is solved numerically. We consider a constant energy gain $\frac{d\gamma}{dz} = 200$ MeV/m (from Run1 experimental results [4]), that satisfies the adiabaticity condition, and we assume that the normalized emittance is preserved during the acceleration. Figure 6 shows that the bunch size decreases overall, but the approximate matching leads to small envelope oscillations. With the adiabatic matching, the transverse beam size and the betatron function are, after the acceleration over 10 m of plasma, $\sim 10 \, \mu$m and ~ 2 cm, respectively. This is important for the magnetic energy spectrometer design. We also note here that the effect of the density ramp at the plasma exit must be included. Still, the matching condition (Equation 2) is defined for only one energy value. Therefore, in order to have the whole beam nearly matched, a small energy spread of the incoming beam, and the beam loading, are necessary conditions. And, to satisfy the request of a constant normalized emittance,

the beam must be accelerated in the blowout regime. It is then clear that matching, blowout and beam loading are reciprocal conditions. Blowout and beam loading are achieved through proper charge and length adjustment of the electron bunch (for a given radius, determined from matching to the pure ion column), that is not discussed here. We also note that the blowout is produced by the head of the electron bunch; therefore, a thin part of the beam will not experience the linear focusing force and its emittance might not be preserved. Still, as shown in numerical simulation [8], the short witness bunch is injected in an overall focusing phase of the proton driven wakefields. Thus, the superimposition of the fields keeps the whole electron bunch confined (head included), minimizing the emittance growth.
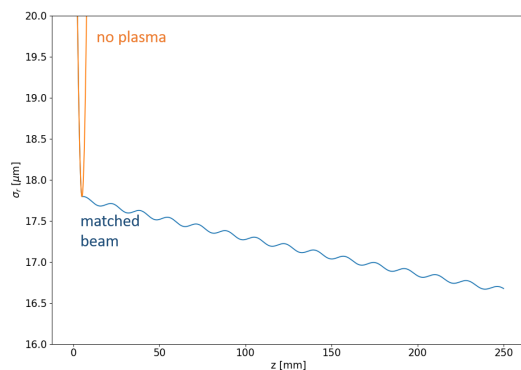

Figure 6. Electron beam envelope for a matched beam accelerated in plasma (blue line), and without plasma (orange line). The result is obtained integrating numerically Equation 1.

3. Conclusions

AWAKE Run2 focuses on producing a high-energy and high-quality beam suitable for high-energy physics applications. To do so, the Run1 experimental setup is modified in order to precisely control the electron beam injection in the proton-driven plasma wakefields. The emittance preservation and the low final energy spread are achieved exploiting full blowout of the plasma electrons, beam loading of the wakefields, and matching of the electron beam to the plasma ion column focusing force. For a given plasma electron density, we therefore define the necessary incoming electron beam parameters, considering the amount of material that the bunch has to cross before entering the plasma, and we find that the use of foils relax the condition on the incoming electron beam betatron function. The electron bunch parameters for matching are determined for the case of a low electron bunch normalized emittance ($20 \, \mathrm{mm \cdot mrad}$). Full parameters were determined for the case of a single driver proton microbunch [8] and a witness bunch normalized emittance of $2 \, \mathrm{mm \cdot mrad}$. Parameters for the higher emittance case need to be determined for the fields driven by the self-modulated proton bunch and also for lower densities (e.g. from 2 to $4 \cdot 10^{14} \, \mathrm{cm}^{-3}$). To unequivocally prove the matching of the electron beam with the plasma wakefields, we will experimentally study the accelerated beam properties as a function of the incoming beam parameters. Therefore, it will be necessary to measure the transverse beam size and position at the entrance of the accelerating plasma section with μm-resolution. As the electron beam has to be injected in the proton driven wakefields, its trajectory must be aligned onto the proton beam for the whole accelerator length within the proton transverse beam size ($200 \, \mu$m, by design) in position and within $0.02 \, \mathrm{mrad}$ in pointing. This will require a challenging design and integration of the diagnostics, due to the compact geometry of the system. Once the acceleration of a high-quality electron bunch is successfully proven, the final energy could be increased by simply scaling up the length of the accelerating plasma section.

References

[1] P. Muggli et al. (The AWAKE Collaboration), AWAKE readiness for the study of the seeded self-modulation of a 400GeV proton bunch, Plasma Physics and Controlled Fusion, **60** (2018), 014046.

[2] M. Turner et al. (The AWAKE Collaboration), Experimental observation of plasma wakefield growth driven by the seeded self-modulation of a proton bunch, Physical Review Letters **122**, 054801 (2019).

[3] E. Adli et al. (The AWAKE Collaboration), Experimental observation of proton bunch modulation in a plasma, at varying plasma densities, Physical Review Letters **122**, 054802 (2019).

[4] E. Adli et al. (The AWAKE Collaboration), Acceleration of electrons in the plasma wakefield of a proton bunch, Nature **561**, 363 (2018).

[5] P. Muggli, Physics to plan AWAKE Run2, these proceedings.

[6] A. Petrenko, Private communication.

[7] J. B. Rosenzweig et al. , Acceleration and focusing of electrons in two-dimensional nonlinear plasma wake fields, Physical Review A **44**, R6189 (1991).

[8] V. K. Berglyd Olsen et al., Emittance preservation of an electron beam in a loaded quasilinear plasma wakefield, Physical Review Accelerators and Beams **21**, 011301 (2018).

[9] T. Katsouleas et al., Beam loading in plasma accelerators, Particle Accelerators **22**, pp. 81-99 (1987).

[10] V. L. Highland, Some practical remarks on multiple scattering, Nuclear Instruments and Methods **129**, 2 (1975).

[11] M. B. Reid , Electron beam emittance growth in thin foils: A betatron function analysis, Journal of Applied Physics **70**, 7185 (1991).

Electron beam characterization with beam loss monitors

L. Verra [ORCID],[1,2,3,*] M. Turner,[1] S. Gessner,[1] E. Gschwendtner,[1] F. M. Velotti,[1] and P. Muggli[2]

[1]*CERN, Geneva 1211, Switzerland*
[2]*Max-Planck Institute for Physics, Munich 80805, Germany*
[3]*Technical University Munich, Munich 85748, Germany*

We present a method to measure the transverse size and position of an electron or proton beam, close to the injection point in plasma wakefields, where other diagnostics are not available. We show that transverse size measurements are in agreement with values expected from the beam optics with a $< 10\%$ uncertainty. We confirm the deflection of the low-energy ($\sim$18 MeV) electron beam trajectory by Earth's magnetic field. This measurement can be used to correct for this effect and set proper electron bunch injection parameters. The advanced wakefield experiment at CERN (AWAKE) relies on these measurements for optimizing electron injection.

I. INTRODUCTION

A. The AWAKE experiment

AWAKE [1], the advanced wakefield experiment at CERN, recently demonstrated acceleration of externally injected electrons in plasma wakefields resonantly excited by a self-modulated [2,3] relativistic proton bunch [4].

The core of the experiment is a 10-m-long rubidium vapor source [5]: a long, fluid-heated heat exchanger evaporates rubidium at 180 °C–230 °C to reach the required vapor density of 0.5–10×10^{14} atoms/cm³. A 120 fs, $<$450 mJ laser pulse ($\lambda = 780$ nm) ionizes the rubidium vapor, creating a plasma cylinder with a radius of approximately 1 mm [6]. The vapor source is connected to the beam line at each end by a 10-mm-diameter aperture. The 400 GeV/c proton bunch provided by the CERN Super Proton Synchrotron (SPS) and delivered by a 750-m-long transfer line [7] with 3×10^{11} particles drives the plasma wakefields.

A photoinjector with an output energy of 5 MeV produces the witness electron bunch, which is then accelerated to 10–20 MeV in a 1-m-long booster structure [8]. A 15-m-long transfer line [9] finally transports the bunch from the booster to the rubidium vapor source. The electron source can provide an electron bunch charge between 0.1 and 1 nC. The nominal normalized emittance of the electron beam is 2 mm · mrad.

We use beam-position monitors (BPMs) to measure the position of the proton and electron beams along the beam line and scintillating screens (BTVs) to measure their transverse bunch profiles [10]. Losses and radiation produced by the proton beam are monitored by proton beam loss monitors (PBLMs) positioned along the transfer line and the vapor source. Figure 1 shows a schematic of the
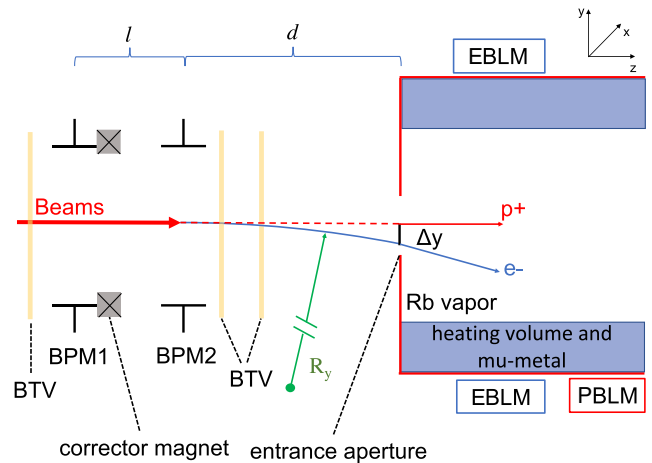

FIG. 1. Schematic of the proton and electron beam transfer line and vapor source close to the vapor source entrance. Main beam diagnostics devices are highlighted: beam-position monitors (BPMs), scintillating screens (BTVs), and electron and proton beam loss monitors (EBLMs and PBLMs, respectively). l and d are the distances between the two BPMs and between the last BPM and the vapor source entrance aperture, respectively. Beams are overlapped at the last two BPMs: The proton beam propagates essentially straight (red arrow); the electron beam trajectory (blue) is bent by Earth's magnetic field with radius of curvature R_y. Δy is the deviation from the straight trajectory in the vertical plane. The drawing is not to scale.

*livio.verra@cern.ch

beam transfer line and of the vapor source close to the vapor source entrance and the relevant diagnostics devices.

B. Experimental challenges

To inject and accelerate the electrons, we spatially and temporally overlap them with the plasma wakefields [11]. This means that the electron and proton beam trajectories have to cross within the plasma cylinder. To investigate the acceleration process and to characterize the wakefields, we want to inject the electron bunch at various locations downstream from the plasma entrance and at various angles with respect to the proton beam trajectory. We observe that the highest capture and acceleration efficiency occurs when the electron beam is injected ∼1 m downstream from the entrance. This is therefore the baseline setup for the acceleration experiment.

Because of the complexity of the vapor source, it was not possible to install any beam position or beam size diagnostics close to or along the plasma. Therefore, the last direct measurement of the electron beam is given by a scintillating screen positioned 0.8 m upstream from the entrance of the vapor source. Furthermore, during the acceleration experiment, no screen can be inserted in the beam line, because this would completely absorb the electron beam. This makes the alignment process for the injection extremely challenging due to the uncertainty on the electron transverse beam size at the injection point and due to the different effects of external magnetic fields on the two beam trajectories, given by the very different rigidity.

The rms transverse size σ at the crossing point is one of the factors that contributes to the charge capture efficiency. Measuring the size near the crossing point is therefore important. Moreover, including the effect of Earth's magnetic field on the low-energy beam is crucial to precisely predict the electron beam trajectory only using information provided by BPMs.

In this article, we illustrate how we use the electron beam loss monitors (EBLMs) to measure the transverse beam size at the plasma entrance and infer it at the injection point. We also use this setup to align the proton-electron beam trajectories, by measuring the effect of Earth's magnetic field on the electron beam trajectory.

II. MEASUREMENT SETUP

When electron and proton beams interact with the material surrounding the vapor source, they generate beam losses in the form of scattered and secondary particles. To detect these losses, we installed two EBLMs 1.5 m downstream of the source entrance aperture as shown in Fig. 1.

Each detector consists of two main parts, optically connected by a light guide: a scintillating material (EJ-200, a polyvinyltoluene-based plastic organic scintillator) and a photomultiplier tube (PMT) biased with a negative high voltage (∼kV). When particles cross the detector

material, they deposit energy; part of this energy is converted to scintillating light that is transmitted to the PMT via the light guide. The PMT produces an amplified electric signal, read out by an oscilloscope. We control the amplification power of each detector independently, with the high voltages applied to the PMTs. These are chosen such that the detectors respond linearly to our range of deposited energies. The linearity of the system has been checked varying the charge of the incoming beam, with fixed trajectory, while measuring the loss signals [12]. The integral of the output signal is proportional to the charge produced by the PMT, i.e., to the deposited energy, and it is indicated as *counts*. In the following text, losses will be expressed in percentage with respect to the maximum counts value of each given dataset.

III. MEASUREMENTS CONCEPT

As mentioned in Sec. I A, the vapor source has a 10-mm-diameter aperture in a 600-μm-thick aluminum foil for the rubidium vapor to exit the source. The thickness of the foil and the size of the aperture have been chosen according to the mechanical and thermal constraints of the vapor source, to minimize the radiation produced by the proton beam during the acceleration experiment and to allow for oblique external injection of the electron beam [11]. When beam particles hit the aluminum entrance foil, they produce secondary particles (scattered electrons and x rays) that deposit energy in the beam loss monitors. The thickness of the foil is sufficient to produce a high signal-to-noise ratio in the detectors when a fraction of the 18 MeV electron beam interacts with the material. The foil thickness and the distance between the foil and detector can, in principle, be adjusted to obtain a suitable signal. The loss signals are proportional to the amount of beam interacting with the material. Measuring these losses, we calculate the electron transverse beam size at the entrance aperture location and the deflection from the straight trajectory caused by Earth's magnetic field on the electron beam.

A. Transverse beam size measurements

The goal of the measurement is to predict the rms transverse electron beam size σ at the injection point, in order to improve the trajectory pointing precision and to estimate the charge capture efficiency. To effectively inject the witness bunch into the wakefields, its transverse size has to be comparable to the transverse extent of the plasma wakefields. This is given by the plasma skin depth c/ω_{pe}, where c is the speed of light and $\omega_{pe} = \sqrt{n_e e^2/\epsilon_0 m_e}$ is the plasma electron frequency (n_e is the plasma electron density, e is the elementary charge, ϵ_0 is the vacuum permittivity, and m_e is the electron mass) [13]. For a plasma electron density of 2×10^{14} cm^{-3}, $c/\omega_{pe} \approx 0.4$ mm. We cannot directly measure the electron beam σ at the injection point, as it is located ∼1 m downstream from the vapor

source entrance. Therefore, we measure the beam size at the plasma entrance and estimate the size at the injection location, from beam optics.

We use the last corrector magnet in the beam line (see Fig. 1) to scan the electron beam position horizontally and vertically across the entrance aperture (examples of electron beam transverse positions at the entrance aperture are shown in Fig. 2) while recording the signals of the electron beam loss monitors. This beam scraper technique is a well-known and routinely used procedure in machine operation for beam collimation and aperture size measurements [14,15] and for transverse beam profile measurements [16]. Using the horizontal and vertical beam positions measured on BPM1 and BPM2, we reconstruct the horizontal and vertical (x, y) position of the electron beam at the entrance location using a linear trajectory prediction:

$$(x, y) = \frac{(x_2 - x_1, y_2 - y_1)}{l} \cdot d + (x_2, y_2), \qquad (1)$$

where $x_{1,2}$ and $y_{1,2}$ are the horizontal and vertical beam position measurements (offset from the center of the beam line) given by BPM1 and BPM2, respectively, l is the distance between the two BPMs, and d is the distance between BPM2 and the plasma entrance. Even though BPM1 is positioned upstream of the corrector magnet, we use its measurement as the beam position at the exit of the corrector, since the two instruments are only ∼9 cm apart and the position deviations at the exit of the magnet are small (< 0.05 mm). We also neglect the effect of Earth's magnetic field on the electron beam trajectory, as it gives a constant deflection (see Sec. III B) and is, thus, not relevant for beam size measurements. For each electron beam position at the aperture, we collect and average 30 measurements. The electron beam normalized emittance

was measured to be ∼9 mm mrad with a quadrupolar scan at the exit of the electron source.

Figure 3 shows one side of the vertical and horizontal scans of the 200 pC electron bunch focused at the entrance aperture, measured by the detector positioned above the vapor source. We note that the minimum of the measured losses is around 5% (position at the entrance < 3.5 mm in Fig. 3), when the beam is centered on the aperture. We attribute this small, but nonzero, value to the non-Gaussian halo of particles around the Gaussian bunch. As soon as a significant number of beam particles hit the aluminum entrance foil, losses increase, reaching a maximum when they all interact with the iris (> 6 mm in Fig. 3).

Assuming that the transverse electron beam charge distribution is Gaussian [9], we can fit independently both rising ramps of each loss scan with an error function

$$\mathrm{erf}(x; \mu, \sigma) = \frac{1}{\sqrt{2\pi\sigma^2}} \int_0^x e^{-[(t-\mu)^2/2\sigma^2]} dt, \qquad (2)$$
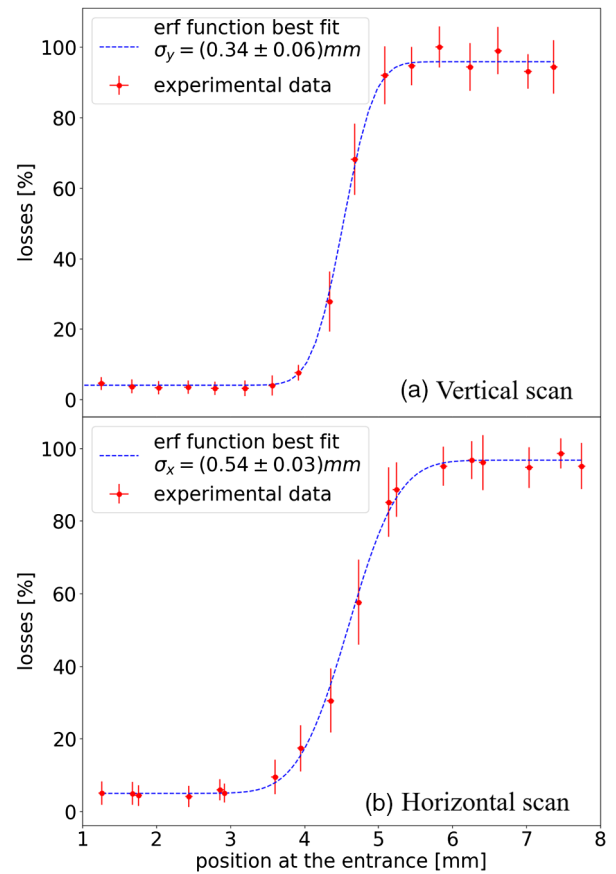
FIG. 3. Loss signals (red dots) measured as a function of the vertical (a) and horizontal (b) position at the vapor source entrance [calculated with Eq. (1)]. Every point is the mean value of 30 measurements; error bars are the standard deviation of the distribution for each point. Each plot is fitted with an error function according to Eq. (2) (blue dashed lines). For these measurements, the 200 pC electron beam is focused at the vapor source entrance (measurement location).
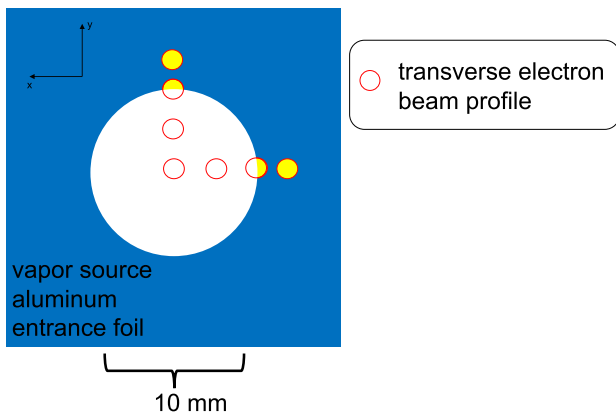

FIG. 2. Schematic drawing of the vapor source entrance. Examples of electron beam transverse positions at the entrance aperture during the horizontal and vertical scans are shown. The yellow areas mark the fraction of the beam interacting with the material, i.e., beam loss. The drawing is not to scale.

TABLE I.   Results of the electron beam scan of the entrance aperture for different focal point locations. Every scan gives two transverse beam size values σ_{fit}, one for each side of the beam loss signal. The final value of σ is obtained as the mean of the two measurements for each scan; the error is calculated propagating the statistical error.

Focal point location	Dimension	σ_{fit} [mm]		σ [mm]
Entrance aperture	Vertical	0.28 ± 0.03	0.34 ± 0.06	0.31 ± 0.03
	Horizontal	0.53 ± 0.04	0.54 ± 0.03	0.54 ± 0.03
1 m downstream from the entrance	Vertical	0.52 ± 0.05	0.4 ± 0.2	0.5 ± 0.1
	Horizontal	1.13 ± 0.06	0.98 ± 0.08	1.06 ± 0.05

where μ is the position of the center and σ the rms of the Gaussian distribution. Every loss scan produces two values of the beam transverse size σ_{fit} (one for each side).

According to the beam line optics [9], we also focus the beam 1 m downstream from the entrance aperture and repeat the measurement, that is, the optical configuration used during the injection experiment. In Table I, we give the resulting σ_{fit} values for the vertical and horizontal scans for the different optics. The error on σ_{fit} is given by the fit covariance matrix and, therefore, quantifies the goodness of the fit.

We note that the two values of σ_{fit} for each scan agree with each other. The final values are calculated as the mean of the two measurements for each scan, as given in Table I; the errors on the final values are calculated propagating the statistical error on the single measurement. When the beam is focused at the entrance, $(\sigma_x, \sigma_y) = (0.54 \pm 0.03, 0.31 \pm 0.03)$ mm; when it is focused 1 m downstream, $(\sigma_x, \sigma_y) = (1.06 \pm 0.05, 0.5 \pm 0.1)$ mm. The measured vertical transverse beam size at the waist (beam focused at the entrance) is slightly larger but still consistent, within 2 times the statistical error, with the nominal value (0.25 mm) [9]. The horizontal σ is measured to be larger than the vertical one in both optical settings; the beam is, therefore, not round as expected from the design. The difference is attributed to the dispersion D in the horizontal plane [17], that is minimized at the beam waist but never fully compensated.

The measurements performed focusing the beam 1 m downstream from the vapor source entrance provide a value of the transverse beam size 1 m upstream from the waist position. Therefore, we calculate the beam size at the waist σ_0 according to linear Gaussian beam optics: $\sigma(z) = \sqrt{(\sigma_0^2 + z^2 \epsilon_g^2/\sigma_0^2) + (D\delta p/p)^2}$ (where $z = 1$ m, σ is the transverse beam size obtained from the measurements, ϵ_g is the geometric emittance, and $\delta p/p \sim 0.5\%$ is the momentum spread [9]). Thus, this measurement allowed us to predict the beam transverse size at the injection point as $(\sigma_x, \sigma_y) = (0.60 \pm 0.06, 0.3 \pm 0.1)$ mm (the errors are calculated propagating the statistical errors obtained above). For a plasma electron density $n_e = 2 \times 10^{14}$ cm^{-3}, we are thus confident that a significant fraction of the bunch is injected into the wakefields (when the beam trajectory is properly set to cross the wakefields).

To further test this measurement concept, we also measure the transverse beam size of the well-characterized SPS "pilot" proton bunch ($\epsilon_N \sim 1$ mm mrad, bunch population $= 10^{10}$ particles). We directly see from Fig. 4 that the slope of the proton bunch (blue curve, rise ramps in the $[-6, -4]$ and $[4,6]$ mm ranges) is steeper than that of the electron beam signal (red curve, rise ramps in the $[-4, -2]$ and $[5,7]$ mm ranges). This indicates that the proton beam transverse size is smaller than the electron beam one. With the same fit procedure described above, we measure it to be $\sigma = (0.12 \pm 0.02)$ mm. It is in good agreement with the expected value (0.10 ± 0.01) mm: This is calculated measuring the proton beam σ with foils emitting optical transition radiation upstream and downstream from the vapor source and the beam emittance in the SPS.

B. Electron beam deflection from Earth's magnetic field

The externally injected electrons have a low energy (~ 18 MeV), and the transfer beam line is not shielded from external magnetic fields. Earth's magnetic field B in the experimental area was measured during the installation campaign to be [18] $B_{(x,y)} \sim (0.2, 0.4)$ G
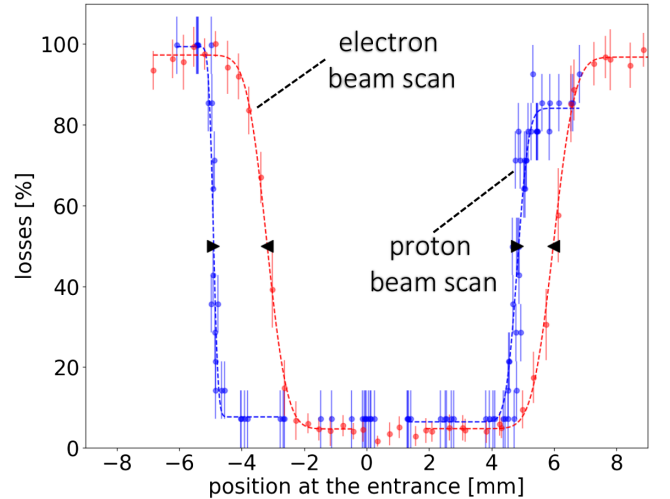

FIG. 4.   Proton (blue dots) and electron (red dots) beam losses as a function of the horizontal position at the vapor source entrance aperture. Dashed lines are the error function fits, the black triangles the centers of the rising ramps.

(with a $\pm15\%$ uncertainty), corresponding to a Larmor radius $R_{(x,y)} = \beta\gamma m_e c/eB_{(y,x)} \sim (1.5, 3)$ km. In particular, the beam trajectory between the last magnetic element and the entrance of the vapor source (more than 3 m away) cannot be approximated as straight, since Earth's magnetic field bends the beam onto a circular trajectory. The vapor source is shielded with mu metal, so that the electron beam trajectory is straight, once injected into it.

We estimate the deviation from straight trajectory as (see Fig. 1) [12]

$$\Delta x, \Delta y \sim d\sin\left(\frac{1}{2}\frac{d}{R_{x,y}}\right). \tag{3}$$

The beam position at the vapor source entrance is predicted to be different from that given by a straight line trajectory by $\Delta x \sim -1.3$ mm (to the right in the horizontal plane) and $\Delta y \sim -0.66$ mm (down in the vertical plane), with an uncertainty of $\pm15\%$.

Since the last BTV is too close to the BPMs to resolve the trajectory deviation, and no beam size or position instrument can be installed at the plasma entrance, it is not possible to directly measure this electron beam trajectory deflection. Thus, we developed an indirect measurement technique that uses both the proton and electron beam loss monitors and the vapor source entrance aperture as follows:

1. *Proton beam scan to establish position references.*— While recording the loss signals from the proton beam loss monitor (positioned on the right-hand side of the vapor source and downstream from the entrance aperture), we scan (horizontally and vertically) the proton beam position over the entrance aperture by shifting the beam parallel to its nominal trajectory (see the blue dots in the horizontal scan of Fig. 4). Note that losses on the negative side (right-hand side) are higher than on the positive side because of the position of the detector. We fit both rise ramps with the error functions [Eq. (2)] and define the position of the entrance aperture edge in the two transverse dimensions as the μ values of the rising ramps (black triangles pointing right in Fig. 4). A straight trajectory prediction of the proton beam trajectory is justified, as the effect of Earth's magnetic field on the 400 GeV/c proton bunch is smaller in amplitude than on the electron bunch by a factor $p_{p+}/p_{e-} = 2.6 \times 10^4$, where $p_{p+,e-}$ is the momentum of the proton and electron beam, respectively. Using the loss scans, we align the proton beam position on the center of the entrance aperture, and we take a trajectory reference on two scintillating screens upstream from the vapor source.

2. *Electron beam scan.*—After aligning the electron beam onto the proton reference trajectory at the scintillating screens (and, therefore, including in the measurement offset readings of the BPMs), we scan horizontally and vertically the electron beam position over the aperture while recording the EBLM loss signals. Then, we compute the beam position at the iris using Eq. (1) (red dots in Fig. 4) and fit the ramps with error functions [Eq. (2)], obtaining the μ values (black triangle pointing left in the plot) as the centers of the ramps. The error on μ is provided by the covariance matrix of the fit.

3. *Comparison of loss signals.*—As shown in Fig. 4, the proton and electron beams loss distributions do not overlap in space because of the effect of Earth's magnetic field on the electron beam trajectory. Thus, we determine the deflection $(\Delta x, \Delta y) = (\mu_{p^+} - \mu_{e^-})_{x,y}$, where μ_{p^+,e^-} are the centers of the rising ramps for the proton and electron scans, respectively. As the σ of the two beams are different, we obtain two values of the deflection for each plane (see right- and left-hand sides of the scans in Fig. 4). We use the mean of the two as a final estimate of the deflection.

The measured values are $\Delta x = (-1.44 \pm 0.03)$ mm (to the right in the horizontal plane) and $\Delta y = (-0.55 \pm 0.03)$ mm (down in the vertical plane). The measurements agree with the calculations discussed above ($\Delta x \sim -1.3$ mm, $\Delta y \sim -0.66$ mm) $\pm 15\%$. This allows us to reach true electron-proton beam crossing at the plasma entrance. Correcting the electron beam trajectory upstream, we could also make the two beam tangent at their crossing point, aligning the position and angle. This trajectory is then used as a reference for injection during the acceleration experiment.

IV. CONCLUSIONS

Using the electron beam loss monitor setup, we conduct measurements on the AWAKE electron beam. Measuring losses at the vapor source entrance aperture when the beams are made to hit the aperture, we measure the transverse beam size of the electron beam for two different magnetic optic settings. The results agree with the optical model of the beam line. This measurement has been essential for the electron beam line commissioning and for the external electron injection experiment, since no other beam transverse size diagnostics is available at that location: The EBLM system provides the closest information about the electron beam size and position to the injection point ($\sim$1 m downstream from the aperture).

Using the same technique, we measure the deflection of the low-energy ($\sim$18 MeV) electron beam trajectory, after the last corrector magnet, caused by Earth's magnetic field. We use this information to correct the electron beam trajectory in order to make it cross with the proton bunch trajectory at the desired location.

We note that this beam loss method is applicable when the beam is smaller than the entrance aperture but larger than the uncertainty on the transverse position. This method could be used in advanced accelerator experiments, when the electron beam for external injection into wakefields must be aligned onto the center of a capillary discharge or gas cell. These have, in general, rather small apertures ($\leq$1 mm) and the beam must be aligned in position and angle.

[1] E. Gschwendtner *et al.* (AWAKE Collaboration), AWAKE, The Advanced Proton Driven Plasma Wakefield Acceleration Experiment at CERN, Nucl. Instrum. Methods Phys. Res., Sect. A **829**, 76 (2016).

[2] E. Adli *et al.* (AWAKE Collaboration), Experimental Observation of Proton Bunch Modulation in a Plasma, at Varying Plasma Densities, Phys. Rev. Lett. **122**, 054802 (2019).

[3] M. Turner *et al.* (AWAKE Collaboration), Experimental Observation of Plasma Wakefield Growth Driven by the Seeded Self-Modulation of a Proton Bunch, Phys. Rev. Lett. **122**, 054801 (2019).

[4] E. Adli *et al.* (AWAKE Collaboration), Acceleration of electrons in the plasma wakefield of a proton bunch, Nature (London) **561**, 363 (2018).

[5] P. Muggli *et al.* (AWAKE Collaboration), AWAKE readiness for the study of the seeded self-modulation of a 400 GeV proton bunch, Plasma Phys. Controlled Fusion **60**, 014046 (2018).

[6] J. T. Moody *et al.*, Multi Keldysh regime resonant ionizing laser pulse propagation through a ten meter Rubidium vapor source at AWAKE, in *Proceedings of COFIL, 2018*.

[7] J. S. Schmidt *et al.*, Status of the proton and electron transfer lines for the AWAKE Experiment at CERN, Nucl. Instrum. Methods Phys. Res., Sect. A **829**, 58 (2016).

[8] K. Pepitone *et al.*, The electron accelerators for the AWAKE experiment at CERN-baseline and future developments, Nucl. Instrum. Methods Phys. Res., Sect. A **909**, 102 (2018).

[9] J. S. Schmidt *et al.*, The AWAKE electron primary beam line, in *Proceedings of IPAC, Richmond, VA, USA* (JACoW, Geneva, Switzerland, 2015), https://doi.org/10.18429/JACoW-IPAC2015-WEPWA039.

[10] S. Mazzoni *et al.*, Beam instrumentation developments for the Advanced Proton Driven Plasma Wakefield Acceleration Experiment at CERN, in *Proceedings of IPAC, 2017*.

[11] M. Turner *et al.*, External electron injection for the AWAKE experiment, in *Proceedings of IEEE Advanced Accelerator Concepts Workshop (AAC), New York, USA* (2018), https://ieeexplore.ieee.org/document/8659402.

[12] L. Verra, Electron beam measurements with beam loss monitors in AWAKE, Master Thesis, CERN-THESIS-2019-003, 2019.

[13] F. F. Chen, *Introduction to Plasma Physics and Controlled Fusion* (Plenum, New York, 1983).

[14] C. A. Pons *et al.*, LHC aperture measurements, in *Proceedings of the International Particle Accelerator Conference, Kyoto, Japan* (ICR, Kyoto, 2010).

[15] J. S. Schmidt *et al.*, AWAKE proton beam commissioning, in *Proceedings of IPAC, 2017* (JACoW, Geneva, Switzerland, 2017), http://accelconf.web.cern.ch/AccelConf/ipac2017/papers/tupik032.pdf.

[16] S. J. Werkema, Transverse beam profile measurement using scrape scans, Report No. FERMILAB-PBAR-NOTE-665, 2001.

[17] C. Bracco *et al.*, Systematic optics studies for the commissioning of the AWAKE electron beamline, in *Proceedings of IPAC, 2019* (JACoW, Geneva, Switzerland, 2019), https://doi.org/10.18429/JACoW-IPAC2019-WEPMP029.

[18] A. Petrenko, CERN (private communication).